Search for the inclusive $b \to d\gamma$ decay at *BABAR*

Deborah Bard

Thesis submitted for the degree of Doctor of Philosophy
University of Edinburgh
2006

Abstract

Radiative penguin decays of B mesons are flavour-changing neutral current (FCNC) processes, studies of which provide fertile ground for precision tests of the Standard Model. Because such decays must proceed through 1-loop or higher order processes, they are rare and their amplitudes are particularly sensitive to interference from other FCNC interactions beyond the SM. This thesis presents the search for the rare radiative penguin process $b \to d\gamma$, carried out at the *BABAR* experiment. This inclusive decay has yet to be observed, with this analysis measuring the branching fraction to 3.1σ significance as $(2.47 \pm 0.72^{+0.42}_{-0.44}) \times 10^{-5}$, where the first error is statistical and the second systematic. 90% confidence limits are set on its branching fraction: $1.4 \times 10^{-5} < BF(b \to d\gamma) < 3.6 \times 10^{-5}$. As a cross-check of the experimental procedure, measurements of the branching fraction and the direct *CP* violation of the exclusive $b \to s\gamma$ decay $B \to K^*\gamma$ are made, with $BF(B \to K^*\gamma) = (3.74 \pm 0.16 \pm 0.41) \times 10^{-5}$ and $A_{CP}(B \to K^*\gamma) = -0.079 \pm 0.036 \pm 0.001$. This analysis also measures the branching fraction and direct *CP* asymmetry of the $b \to s\gamma$ decay: $BF(b \to s\gamma) = (3.54 \pm 0.19 \pm 0.39) \times 10^{-4}$ and $A_{CP}(b \to s\gamma) = 0.040 \pm 0.035 \pm 0.004$. The branching fraction of the exclusive $b \to d\gamma$ decays $B \to (\rho, \omega)\gamma$ is also measured as a cross-check, and found to be $BF(B \to (\rho, \omega)\gamma) = (1.46 \pm 0.59^{+0.18}_{-0.19}) \times 10^{-6}$. All measurements made with control samples are found to be consistent with recent published experimental results and theoretical predictions. Finally, the ratio of the branching fractions $b \to d\gamma$ and $b \to s\gamma$ is used to set a bound on the CKM matrix element ratio $0.17 < |\frac{V_{td}}{V_{ts}}| < 0.43$ at 90% confidence level. Combining this with the ratio obtained from the cross-check $B \to K^*\gamma$ and $B \to (\rho, \omega)\gamma$ control samples gives $0.15 < |\frac{V_{td}}{V_{ts}}| < 0.37$.

Declaration

This work represents the effort of many members of the *BABAR* collaboration at SLAC, California. I have been an integral part of a small team of people working on the $b \to d\gamma$ analysis. The results of detector studies presented in Chapter 3 are the work of other members of the *BABAR* collaboration, and all results from Chapter 4 onwards are my own work. The writing of this thesis is entirely my own work.

Acknowledgements

First, I'd like to thank my supervisor Steve Playfer for all the support and guidance he provided during my research and the writing of this thesis. His patience in explaining the subtleties of radiative penguin decays and helping me through the analysis procedure has been much appreciated. Thanks also to my second supervisor Franz Muheim, and to all the Edinburgh PPE group for their help and the fun we had during my time at Edinburgh.

During this analysis I worked with many excellent physicists, and in particular I'd like to thank Tim Beck, Bruce Schumm and all the members of the HEP group at UCSC who I worked alongside in the search for $b \to d\gamma$. Francesca di Lodovico and Andrew Eichenbaum were endlessly patient while I first got to grips with the *BABAR* analysis environment, and Roger Barlow of Manchester University was invaluable in guiding me through the intricacies of EMC software during my service task.

I owe enormous thanks to my family - my parents Nic and Di and my sister Rachel - without whose love and encouragement I'd never have finished this thesis.

Finally, I am grateful to the Particle Physics and Astronomy Research Council of the United Kingdom for the support provided throughout my graduate studies.

Contents

List of Figures

List of Tables

Chapter 1

Introduction

This thesis details measurements of the $b \to s\gamma$ decay and the search for the $b \to d\gamma$ decay, carried out at the *BABAR* experiment. The physics of these decays are closely related. In the Standard Model (SM), the leading order contributions to their amplitudes are flavour changing neutral quark currents which cannot proceed through tree-level SM weak processes. They must involve one loop or higher order diagrams, the leading of which is depicted in Figure 1.1. Decays dominated by such processes are called radiative penguin decays.

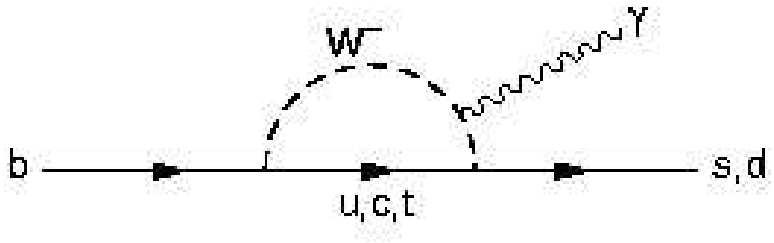

Figure 1.1: Feynman diagram for the $b \to s\gamma$ and $b \to d\gamma$ radiative penguin transitions.

Radiative penguin decays of B mesons have attracted increasing theoretical attention as experimental measurements have grown more precise. Most interesting is the potential for the discovery of new physics effects in the $b \to s\gamma$ or $b \to d\gamma$ transition amplitudes that cannot be accounted for in the SM. Many theoretical extensions to the SM, including super-symmetric theories, involve new particles

and couplings that lead to one-loop contributions similar to that in Figure 1.1 but with non-SM particles in the loop. The absence of a dominant tree-level contribution and the large mass of the loop propagators make the amplitudes of penguin transitions highly susceptible to interference from such new physics interactions.

A less exotic, but nonetheless valuable, use of radiative penguin measurements is the independent determination of SM parameters. Most important among the SM parameters currently measurable in radiative penguin physics is the ratio of CKM matrix elements $|\frac{V_{td}}{V_{ts}}|$, which is currently only known from B_d/B_s mixing [27].

The $b \to s\gamma$ transition is well documented in scientific literature [2, 3]. The branching fraction and *CP* violating properties have been measured with precision; the world average currently stands at $3.55 \pm 0.24 \times 10^{-4}$ for the branching fraction and 0.004 ± 0.037 for the direct *CP* asymmetry. So far no discrepancies between experimental results and theoretical predictions have appeared. The $b \to d\gamma$ transition is much rarer than $b \to s\gamma$, and has only recently been observed in the exclusive modes $B \to (\rho, \omega)\gamma$ [24]. This thesis presents the search for the inclusive $b \to d\gamma$ decay in the dataset currently available at *BABAR*. Observation of the inclusive branching fraction is not expected, but analysis indicates that this challenging measurement is feasible in the future.

Several methods exist in scientific literature to isolate the signal decay from background. The analysis presented here is based on the 'semi-inclusive' or 'sum-of-modes' technique, where many exclusive hadronic decay modes are combined to approximate the inclusive decay.

The main challenge facing this analysis is the separation of the signal decays from a huge background. Selection criteria are optimised on *BABAR* Monte Carlo simulated events, and applied to minimise backgrounds. To reject the largest contribution to the large background, from $q\bar{q}$ or 'continuum' events, a multivariate technique (Neural Network) is used combining information about the event

topology. The $b \to s\gamma$ and $b \to d\gamma$ signal shapes are finally extracted from data using a likelihood fit to the distribution of kinematic variables from events that fulfil the selection criteria.

Chapter 2

Theoretical motivation

2.1 Introduction to the Standard Model

The goal of particle physics is to identify and understand the elementary constituents and forces of matter. The Standard Model of particle physics classifies matter and describes its interactions with quantum field theories. It has proven a remarkably successful model in predicting and explaining particle properties and interactions and has yet to be significantly challenged by experimental data.

The elementary building blocks of matter are spin-1/2 fermions - the quarks, leptons and their anti-particles. They interact through the exchange of spin-1 gauge bosons. All are point-like at the energy resolutions available to current accelerators. Leptons are observed individually, but single or 'bare' quarks are never seen - they are always bound together in mesons (quark - anti-quark pairs) or baryons, a condition know as 'quark confinement'. Everyday matter is made of the lowest generation of particles - the u, d and e^-. Others can only be produced

quarks	u, c, t d, s, b
leptons	e^-, μ^-, τ^- ν_e, ν_μ, ν_τ

Table 2.1: The three generations of quarks and leptons. Their antiparticles are denoted $\bar{u}$, $\bar{d}$, e^+, $\bar{\nu_\mu}$ etc.

in particle accelerators.

Whether the four fundamental forces affect particles depends on their properties. All particles (except gluons) carry weak isospin, and so can interact weakly though the exchange of the Z^0, W^+ or W^-. Quarks and all charged particles feel the electromagnetic force through photon exchange, but only quarks carry colour and therefore interact via the strong force, mediated by the exchange of gluons. The theory of Quantum Chromodynamics (QCD) describes strong interactions. The SM unifies the weak and electromagnetic forces in a single 'electroweak' force with four gauge fields. The γ remains massless while the weak gauge fields acquire mass by the spontaneous breaking of electroweak gauge symmetry induced by the Higgs mechanism [4]. It is as yet uncertain whether the strong force will be unified with the electroweak theory or at what energy scale this would take place. Gravity is the fourth force, felt by all massive particles, but its effect is negligible for particle physics processes and is not described by the SM.

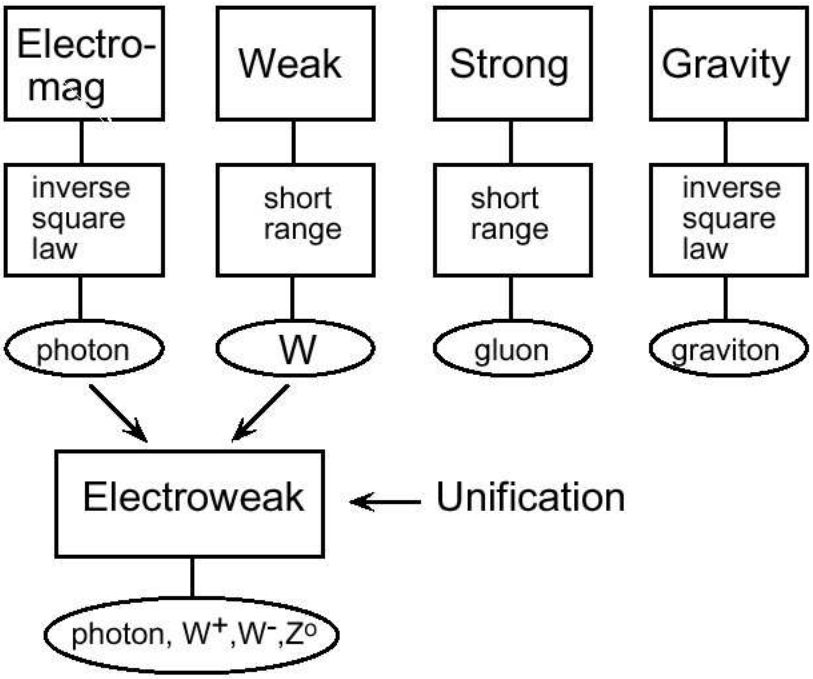

Figure 2.1: The four fundamental forces.

2.2 Symmetries

A symmetry transformation of a physical system is one for which the associated operation does not alter the experimental results. Noether's theorem [5] states that for any symmetry of a system, there must exist a corresponding conservation law, and vice versa. Symmetries are therefore a useful probe of the underlying physics of a system, and group theory is used to study and characterise symmetrical transformations.

Symmetries can, however, be broken. Parity (P) is the space-inversion transformation, turning the coordinate of a particle from $\vec{r}$ to $-\vec{r}$.

$$P|f(\vec{r})\rangle = |f(-\vec{r})\rangle \tag{2.1}$$

where f is some function of $\vec{r}$. It is broken when the weak interaction is introduced.

The charge conjugation (C) transformation changes a particle's charge (and all other additive quantum numbers) from Q to $-Q$, turning a particle into an anti-particle.

$$C|f(Q)\rangle = |f(-Q)\rangle \tag{2.2}$$

Combined, CP transforms a particle into its anti-particle with inverse momentum, and is broken in quark interactions.

2.3 The Standard Model and the CKM matrix

When the quark model was first introduced, only the light quark flavours u, d and s were required to describe observed particles. However, from the measured rates of weak decays, the coupling constant for the vertex $W^- \to \bar{u}s$ was found to be twenty times less than the coupling constant for $W^- \to \bar{u}d$. Furthermore both were smaller than the weak coupling constant, G_F, measured in the weak leptonic decays $W^- \to \bar{\nu}_e e^-$ and $W^- \to \bar{\nu}_\mu \mu^-$. In 1963, Cabibbo [6] proposed that G_F should not be applied to the vertices alone, but to W^- and u coupled

to a superposition of s and d states given by:

$$d' = d\cos\theta_C + s\sin\theta_C \tag{2.3}$$

where θ_C is the Cabibbo mixing angle, experimentally determined to be 12.8^o. G_F is therefore reduced by the factors $\cos\theta_C$ and $\sin\theta_C$ for the vertices $W^- \to \bar{u}d$ and $W^- \to \bar{u}s$ respectively. Essentially, the electroweak eigenstates of the quarks are not the quark mass eigenstates, but a mixture of them.

In 1970, Glashow, Iliopolous and Maiani (GIM) [7] predicted the existence of the as-yet unobserved c quark, based on the absence of observations of the $K^0 \to \mu^+\mu^-$ decay, a transition which is allowed in the Cabibbo theory. In 1974, the simultaneous discovery of the $c\bar{c}$ (charmonium) particle J/ψ at SLAC and Brookhaven [9, 10] won the 1976 Nobel Prize for Burton Richter and Samuel Ting. It was assumed that c couples to $s^{'}$ (which is orthogonal to $d^{'}$) and is defined as:

$$s' = -d\sin\theta_C + s\cos\theta_C. \tag{2.4}$$

The eigenstates of the d and s quarks, which couple to the W^- boson, can therefore be expressed by:

$$\begin{pmatrix} d' \\ s' \end{pmatrix} = \begin{pmatrix} \cos\theta_C & \sin\theta_C \\ -\sin\theta_C & \cos\theta_C \end{pmatrix} \cdot \begin{pmatrix} d \\ s \end{pmatrix}. \tag{2.5}$$

When the bottom quark b was discovered in 1977 [11], it followed from symmetry considerations that it should have a partner, the top quark t. Experimentally, t was to remain elusive for many years, but certain calculations of the $W^\pm$ and Z^0 masses and couplings proved to be very sensitive to the top quark mass, and precision measurement of these allowed it to be indirectly calculated. 't Hooft and Veltman won the Nobel Prize for the work that produced this calculation, and t was finally observed at the Tevatron experiment at Fermilab in 1995 [12].

Weak interactions therefore operate on three quark doublets, or generations:

$$\begin{pmatrix} u \\ d' \end{pmatrix} \begin{pmatrix} c \\ s' \end{pmatrix} \begin{pmatrix} t \\ b' \end{pmatrix}. \tag{2.6}$$

In 1973 (before the discovery of the c, b and t quarks), Kobayashi and Maskawa extended the Cabibbo-GIM model to include a third generation of quarks, and introduced the CKM matrix [8]. This was necessary to explain the phenomenon of *CP*-violation, described in Section 2.4.

$$\begin{pmatrix} d' \\ s' \\ b' \end{pmatrix} = \begin{pmatrix} V_{ud} & V_{us} & V_{ub} \\ V_{cd} & V_{cs} & V_{cb} \\ V_{td} & V_{ts} & V_{tb} \end{pmatrix} . \begin{pmatrix} d \\ s \\ b \end{pmatrix} . \tag{2.7}$$

The CKM matrix is unitary ($V_{CKM}V_{CKM}^{\dagger} = 1$) and the individual matrix elements can be measured. With unitarity imposed, the 90% confidence limits for the magnitude of the elements are [29]:

$$|V_{CKM}| = \begin{pmatrix} 0.9739 - 0.9751 & 0.221 - 0.227 & 0.0029 - 0.0045 \\ 0.221 - 0.227 & 0.9732 - 0.9744 & 0.037 - 0.044 \\ 0.0048 - 0.014 & 0.037 - 0.043 & 0.9990 - 0.9992 \end{pmatrix} . \tag{2.8}$$

The leading diagonal elements are close to one, and therefore the coupling constants are strongest for vertices with quarks belonging to the same generation. Transitions can occur across generations, but the unitarity condition requires that the charges of the quarks must differ.

2.4 *CP* violation in the Standard Model

By requiring its unitarity, the free parameters of the CKM matrix can be reduced to four, including a complex phase term which is the only source of *CP*-violation in the SM. In fact, the mixing of only two generations of quarks would not allow *CP*-violation, as it introduces only one angle. This led to the prediction of three quark generations by Kobayashi and Maskawa before experimental evidence for the third existed.

Defining $\lambda = |V_{us}|$, the Wolfenstein parameterisation of the CKM matrix is realised:

$$V = \begin{pmatrix} 1 - \frac{\lambda^2}{2} & \lambda & A\lambda^3(\rho - i\eta) \\ -\lambda & 1 - \frac{\lambda^2}{2} & A\lambda^2 \\ A\lambda^3(1 - \rho - i\eta) & -A\lambda^2 & 1 \end{pmatrix} + O(\lambda^4). \tag{2.9}$$

The unitarity of the CKM matrix gives constraints on the relationships between the matrix elements, one of which is Equation 2.10.

$$V_{ud}V_{ub}^* + V_{cd}V_{cb}^* + V_{td}V_{tb}^* = 0. \tag{2.10}$$

This equation can be expressed as a triangle in the complex plane, one of six 'unitarity' triangles (UT), and has particular relevance to B physics (Figure 2.2).

The UT can be rearranged by dividing Equation 2.10 by $V_{cd}V_{cb}^*$ and placing two of the rescaled vertices at (0,0) and (1,0). The third vertex is conventionally denoted as $(\bar{\rho}, \bar{\eta})$, where $\bar{\rho} = \rho(1 - \lambda^2/2)$ and $\bar{\eta} = \eta(1 - \lambda^2/2)$. The three inner angles become α, β and γ - see Figure 2.2.

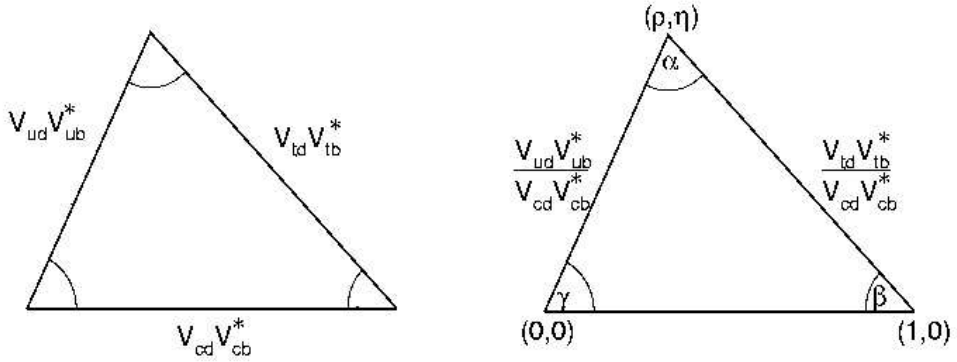

Figure 2.2: The Unitarity Triangle (left) and the rescaled UT in the Wolfenstein parameterisation (right).

2.4.1 *CP* violation in the kaon system

In 1947, G.D.Rochester and C.C.Butler observed a strange occurrence in the tracks of cosmic rays in their cloud chamber experiment [13]. Two unknown particles entered the chamber. One decayed into two pions, the other to a pion and a neutral particle. It was not until 1950 that confirmation of this discovery was made with a cloud chamber experiment at Caltech. Kaons, mesons containing an s-quark, were named in 1953, and from the beginning their behaviour was

difficult to explain. The production rates implied the strong interaction, while their long lifetimes indicated they decayed via the weak interaction.

In 1952, Pais postulated a new quantum number, conserved in strong decays and violated in weak decays, which would explain such behaviour. Gell-Mann refined this idea and called it 'strangeness'. Working together, in 1955 they classified the strangeness of all particles and found that $K^0 \neq \bar{K}^0$, a curious phenomenon as there is only one π^0.

Applying CP to a K^0 state:

$$CP|K^0\rangle \rightarrow |\bar{K}^0\rangle \tag{2.11}$$

$$CP|\bar{K}^0\rangle \rightarrow |K^0\rangle \tag{2.12}$$

Thus K^0 and $\bar{K}^0$ are not CP eigenstates, although such states can be constructed by a linear sum of K^0 and $\bar{K}^0$:

$$|K_1^0\rangle = \frac{1}{\sqrt{2}}(|K^0\rangle + |\bar{K}^0\rangle) \qquad CP = +1 \tag{2.13}$$

$$|K_2^0\rangle = \frac{1}{\sqrt{2}}(|K^0\rangle - |\bar{K}^0\rangle) \qquad CP = -1 \tag{2.14}$$

We can rewrite 2.11 and 2.12:

$$CP|K_1^0\rangle \rightarrow |K_1^0\rangle \tag{2.15}$$

$$CP|K_2^0\rangle \rightarrow -|K_2^0\rangle. \tag{2.16}$$

The physical states of the neutral kaons are in fact not pure K^0 and $\bar{K}^0$ but weak eigenstates with very different lifetimes. These physical eigenstates were originally assumed to coincide with the CP eigenstates, K_1^0 and K_2^0.

Assuming CP conservation, the short-lived K_1^0 decays primarily into two pions, since this final state also has CP=+1, and has a mean lifetime 8.96×10^{-11} seconds. The long-lived K_2^0 decays primarily into three pions, and has a mean lifetime of 5.18×10^{-8} seconds. The mass of the K_2^0 is only slightly larger than the sum of the masses of three pions, so this decay proceeds about 600 times

slower than the two-pion mode. The two different modes of decay were observed by Leon Lederman and his coworkers in 1956, thus establishing the existence of the two weak eigenstates (i.e. states with definite lifetimes under decays via the weak force) of the neutral K mesons.

In 1964, James Cronin and Val Fitch of BNL observed the decay $K_2^0 \rightarrow \pi^+\pi^-$, where a CP=-1 state goes to a CP=+1 state. In fact, the true physical states of the neutral kaons, K_L^0 and K_S^0, are indeed weak eigenstates but not the CP eigenstates K_1^0 and K_2^0 as previously assumed. They can be described in terms of K_1^0 and K_2^0 through the relations:

$$K_S^0 = \frac{K_1^0 + \epsilon K_2^0}{\sqrt{1-|\epsilon^2|}} \tag{2.17}$$

$$K_L^0 = \frac{K_2^0 + \epsilon K_1^0}{\sqrt{1-|\epsilon^2|}} \tag{2.18}$$

where ϵ is complex, with $|\epsilon| \approx 2\times10^{-3}$ and phase of 43.5^o. Thus occasionally the K_L^0 decays with CP= +1. Likewise the K_S^0 can decay with CP= -1. CP violation had been observed for the first time, a discovery that won the Nobel Prize in 1980.

2.4.2 *CP* violation in the *B* meson system

The Υ meson (the $b\bar{b}$ bound state) was first observed in 1977 by S.R.Herb *et al.* at the E288 experiment at Fermilab. The measurement of the long Υ lifetime at the Stanford Linear Accelerator Centre in 1983 marked it out as the ideal working environment for a detailed CP study. The b lifetime means that B mesons produced at today's B-factories travel a measurable distance before decaying, providing the ideal tool for searching for evidence of CP asymmetry in the b-quark system.

2.4.3 The three types of *CP* violation in the *B* meson system

There are three ways that CP violation can occur in B (and K) meson decays:

- *CP* violation in neutral B mixing, where the mass eigenstates are not *CP* eigenstates.
- *CP* violation in decay, occurring in both charged and neutral B decays, where the amplitude of a decay mode and its *CP*-conjugate process have different magnitudes.
- *CP* violation in the interference of decays with and without mixing, which occurs when a decay has a final state common to both the B^0 and the $\bar{B}^0$.

2.4.4 *CP* violation in mixing

In the absence of B^0-$\bar{B}^0$ mixing, the time evolution of a neutral B state would follow the simple form:

$$|B^0(t)\rangle = |B^0(0)\rangle e^{-iHt} \tag{2.19}$$
$$|\bar{B}^0(t)\rangle = |\bar{B}^0(0)\rangle e^{-iHt}$$

with the Hamiltonian:

$$H = M - \frac{i}{2}\Gamma \tag{2.20}$$

where M is mass and Γ width. If mixing occurs, a B^0 and $\bar{B}^0$ can mix via an intermediate state, as shown in Figure 2.3.

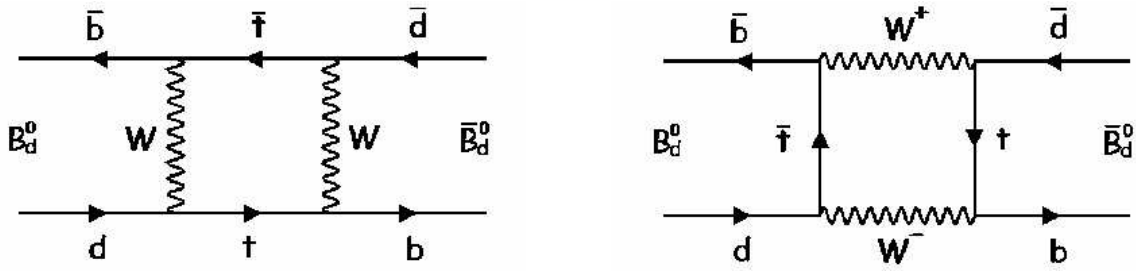

Figure 2.3: Mixing in the B meson system.

The initial state is a superposition of B^0 and $\bar{B}^0$ which evolves as a function of time in the following manner:

$$i\frac{d\Psi(t)}{dt} = \widehat{H}\Psi(t) \tag{2.21}$$

where:

$$\Psi(t) = \begin{pmatrix} |B^0(t)\rangle \\ |\bar{B}^0(t)\rangle \end{pmatrix}$$

and

$$\widehat{H} = \widehat{M} - \frac{i}{2}\widehat{\Gamma} = \begin{pmatrix} M_{11} - \frac{i}{2}\Gamma_{11} & M_{12} - \frac{i}{2}\Gamma_{12} \\ M_{21} - \frac{i}{2}\Gamma_{21} & M_{22} - \frac{i}{2}\Gamma_{22} \end{pmatrix} \tag{2.23}$$

$\widehat{M}$ and $\widehat{\Gamma}$ are Hermitian matrices with positive (real) eigenvalues. M_{ij} is the contribution from transitions with virtual intermediate states (the dispersive part) and Γ_{ij} is the contribution from transitions with physical intermediate states (the absorptive part). The diagonal elements of these 2x2 matrices are associated with flavour-conserving transitions, while the off-diagonal elements are associated with mixing transitions.

Equation 2.23 can be diagonalised using linear combinations of $|B^0\rangle$ and $|\bar{B}^0\rangle$:

$$p|B^0\rangle \pm q|\bar{B}^0\rangle \tag{2.24}$$

which has eigenvalues $\lambda_\pm = H_{11} \pm (H_{12}H_{21})^{\frac{1}{2}}$. The corresponding eigenvalue equations give:

$$\frac{q}{p} = \left(\frac{M_{12}^* - \frac{i}{2}\Gamma_{12}^*}{M_{12} - \frac{i}{2}\Gamma_{12}}\right)^{\frac{1}{2}} \tag{2.25}$$

The CP transformation changes $B^0 \rightarrow \bar{B}^0$ and $\bar{B}^0 \rightarrow B^0$:

$$CP|B^0\rangle = e^{i\zeta}|\bar{B}^0\rangle \tag{2.26}$$

$$CP|\bar{B}^0\rangle = e^{-i\zeta}|B^0\rangle \tag{2.27}$$

The probability amplitudes for the electroweak transitions $B^0 \rightarrow \bar{B}^0$ and $\bar{B}^0 \rightarrow B^0$ are:

$$\langle B^0|\widehat{T}_{weak}|\bar{B}^0\rangle = M_{12} - \frac{i}{2}\Gamma_{12} \tag{2.28}$$

$$\langle \bar{B}^0|\widehat{T}_{weak}|B^0\rangle = M_{12}^* - \frac{i}{2}\Gamma_{12}^* \tag{2.29}$$

If CP is conserved, then $|e^{-i\zeta}|$=1, so that $M_{12} = e^{-2i\zeta}M_{12}^*$ and $\Gamma_{12} = e^{-2i\zeta}\Gamma_{12}^*$. When the mass eigenstates (i.e. the physically observable B mesons) are not

CP eigenstates, there is a relative phase between M_{12} and Γ_{12}. Combining these conditions, we have:

$$\Im(M_{12}^{*}\Gamma_{12}) = 0 \Rightarrow CP\ conserved \tag{2.30}$$

$$\Im(M_{12}^{*}\Gamma_{12}) \neq 0 \Rightarrow CP\ violated \tag{2.31}$$

This is equivalent to (using Equation 2.25):

$$|\frac{q}{p}| = |e^{i\zeta}| = 1 \Rightarrow CP\ conserved \tag{2.32}$$

$$|\frac{q}{p}| \neq 1 \Rightarrow CP\ violated \tag{2.33}$$

This can be experimentally measured by looking for an asymmetry in the semi-leptonic decays of mesons initially tagged as B^0 or $\bar{B}^0$.

$$a_{SL} = \frac{\Gamma(\bar{B}^0(t) \to l^+\nu X) - \Gamma(B^0(t) \to l^-\nu X)}{\Gamma(\bar{B}^0(t) \to l^+\nu X) + \Gamma(B^0(t) \to l^-\nu X)} \tag{2.34}$$

$$a_{SL} = \frac{1 - |q/p|^4}{1 + |q/p|^4} = Im\frac{\Gamma_{12}}{M_{12}} \tag{2.35}$$

a_{SL} is expected to be small, and the world average of experimental measurements of this asymmetry is [1]:

$$a_{SL} = -0.0030 \pm 0.0078 \quad \to \quad |\frac{q}{p}| = 1.0015 \pm 0.0039. \tag{2.36}$$

2.4.5 *CP* violation in decay

A_f and $A_{\bar{f}}$ are the decay amplitudes for the transitions $B \to f$ and $\bar{B} \to \bar{f}$ respectively, given by:

$$A_f = \langle f|\widehat{H}^{weak}|B\rangle \tag{2.37}$$

$$A_{\bar{f}} = \langle \bar{f}|\widehat{H}^{weak}|\bar{B}\rangle$$

Experimental evidence for direct *CP* violation comes from the measurement of:

$$|\frac{A_{\bar{f}}}{A_f}| \neq 1 \Rightarrow CP\ violation \tag{2.38}$$

In this case, *CP* violation results from interference between at least two different terms in the decay amplitude which have different weak and strong phases. In both types, only the relative phase difference between two phase shifts has physical meaning.

$$A_f = \sum_i A_i e^{i(\delta_i+\phi_i)} \qquad (2.39)$$
$$A_{\bar{f}} = \sum_i A_i e^{i(\delta_i-\phi_i)}$$

where $i = 1$, 2 etc. δ_i is the strong phase, and ϕ_i the weak phase.

In 2004, *BABAR* announced the first experimental evidence for direct *CP* violation in the process $B^0 \to K^+\pi^-$, depicted in Figure 2.4 [16]. The ΔE^* distribution (see Section 5.2.1 for description) is shown for $B^0 \to K^+\pi^-$ in blue and $\bar{B}^0 \to K^-\pi^+$ in red, clearly showing the difference in the number of events found in each decay mode.

$$\frac{(n_{K^-\pi^+} - n_{K^+\pi^-})}{(n_{K^-\pi^+} + n_{K^+\pi^-})} = -0.133 \pm 0.030(stat) \pm 0.009(syst) \qquad (2.40)$$

where $n_{K^\pm\pi^\mp}$ is the number of events found of $K^\pm\pi^\mp$ decay mode.

2.4.6 *CP* violation in the interference of mixing and decay

The second of *CP* violation manifests itself as the difference between the phases of B^0-$\bar{B}^0$ mixing and of the decay amplitude. A B^0 may decay directly, or oscillate into its anti-particle before decaying to a final state common to both B^0 and $\bar{B}^0$ (see Figure 2.5). These two paths have a slightly different phase, and the interference between them produces the asymmetry.

An experimentally measurable quantity independent of phase convention is:

$$\lambda \equiv \pm\frac{q}{p}\frac{A_{\bar{f}_{CP}}}{A_{f_{CP}}} \qquad (2.41)$$

λ is complex, and *CP* is conserved if $|q/p| = 1$, $|A_{\bar{f}_{CP}}/A_{f_{CP}}| = 1$, and if there is no relative phase between p/q and $A_{\bar{f}_{CP}}/A_{f_{CP}}$. We can describe these requirements

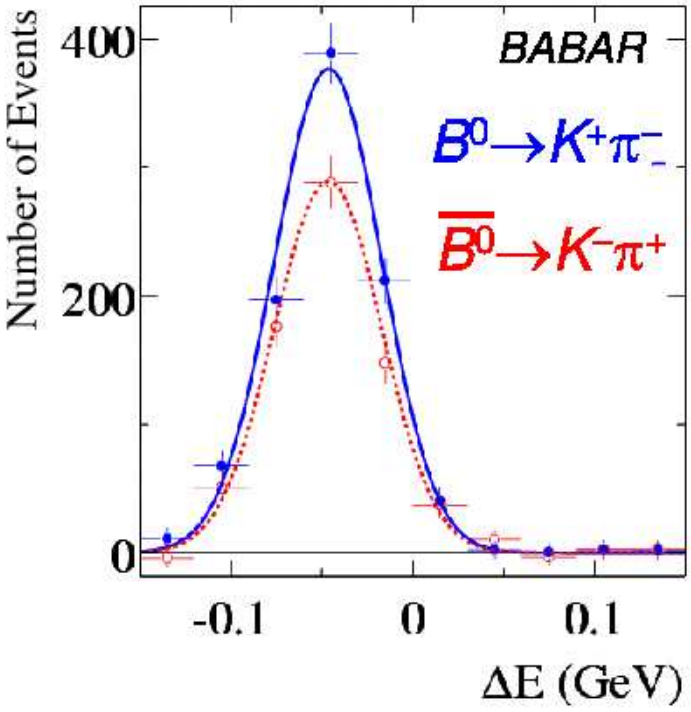

Figure 2.4: Direct CP violation in $B^+ \to K^+\pi^+$.

with the relations:

$$|\lambda| \neq 1 \Rightarrow CP\ violation \tag{2.42}$$

$$\text{or} \quad Im(\lambda) \neq 0 \Rightarrow CP\ violation. \tag{2.43}$$

The so-called 'golden mode' for searching for this type of *CP* asymmetry in experiments is $B^0 \to J/\psi K^0_S$. This decay has well-defined *CP* properties, and there are few theoretical uncertainties in the relationship between the decay asymmetry and CKM parameters. Experimentally, it is easy to identify as the branching ratio is relatively large, and the J/ψ decay into two leptons together with the displaced vertex from the $K^0_S \to \pi^+\pi^-$ decay gives a clear experimental signal.

With little theoretical uncertainty, the phase difference between the two am-

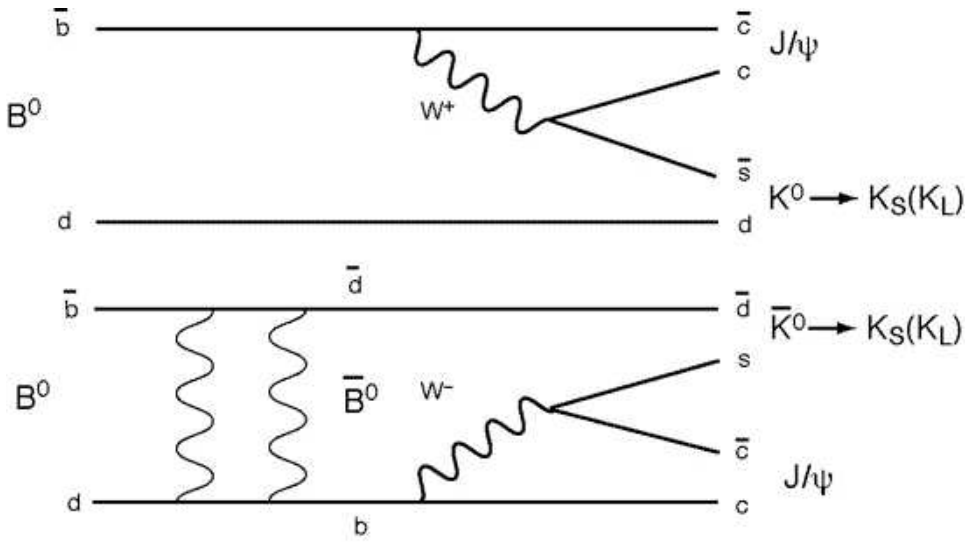

Figure 2.5: A B^0 may decay directly or may oscillate into a $\bar{B}^0$ before decay. Interference between the two paths produces an asymmetry.

plitudes is equal to twice the angle β in the Unitarity Triangle (see Section 2.4).

$$\beta = arg\left[\frac{-V_{cd}V_{cb}^*}{V_{td}V_{tb}^*}\right] \tag{2.44}$$

The first observation of time-dependent *CP* violating asymmetries in the *B*-meson system was announced in 2000, with the measurement of $\sin 2\beta$ in $B^0 \to J/\psi\, K_S^0$. The most recent *BABAR* result, shown in Figure 2.6 [15], illustrates how precise the measurement of this parameter has become over the years:

$$\sin 2\beta = 0.722 \pm 0.040(stat) \pm 0.023(syst) \tag{2.45}$$

It is now one of the most stringent tests of the Standard Model. Today the world average (for all charmonium modes) is 0.687 ± 0.032(0.028 stat only)[1], which gives a value of $\beta = (21.7^{+1.3}_{1.2})^\circ$. The alternative solution, $\beta = (68.3^{+1.2}_{-1.3})^\circ$, is excluded by measurements of $B \to J/\psi\, K^{*0}$.

2.5 Radiative penguin decays

The tree-level decay of a b quark to a d or s quark through direct Z emission is a weak process forbidden in the SM. Beyond the tree-level diagram, the transition

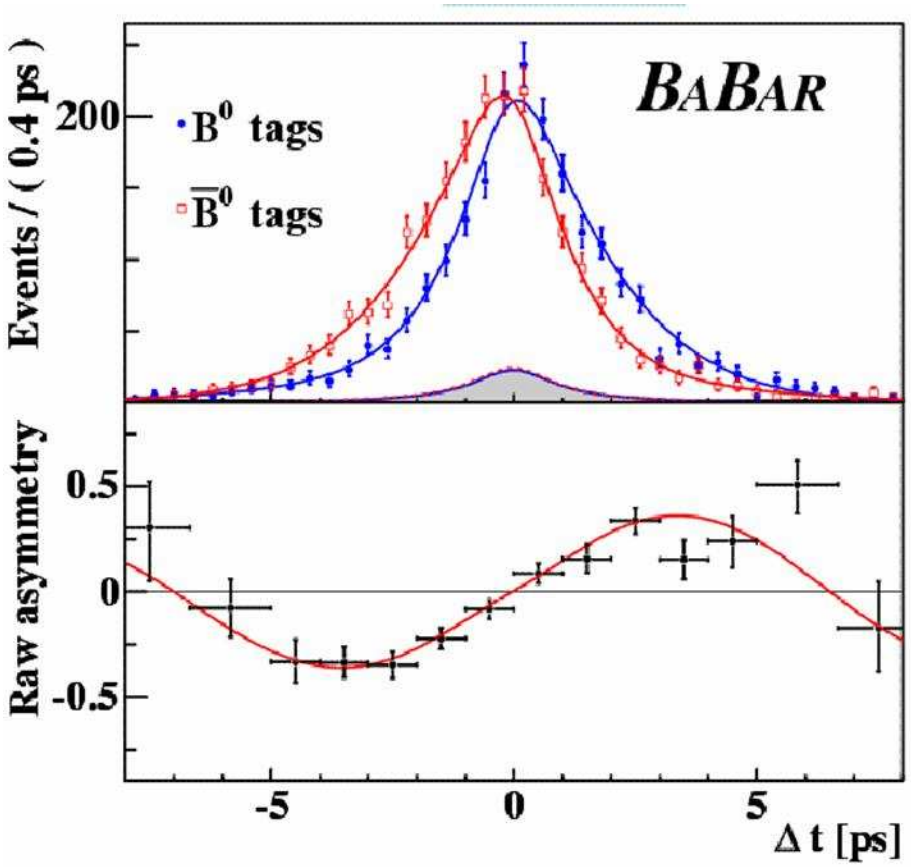

Figure 2.6: Time dependent *CP* asymmetry in the $B^0 \to J/\psi K^0_S$ decay.

can occur through the emission and re-absorption of a W boson. This is known as a one loop Flavour Changing Neutral Current (FCNC) process, commonly known as a penguin diagram. When a photon is emitted from the loop, it becomes a radiative penguin process, shown in Figure 2.7.

The intermediate quark in the loop may be either a t, c or u, with the t quark dominant, and the photon can be emitted from any of the charged particles. The overall SM amplitude is the sum of the u, $c$and t quark contributions, as shown in Figure 2.8.

The CKM factors are shown in Figure 2.8, and the amplitudes of each contri-

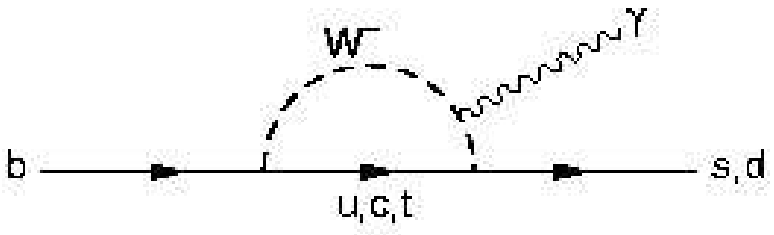

Figure 2.7: Feynman diagram for the $b \to s\gamma$ and $b \to d\gamma$ radiative penguin transitions.

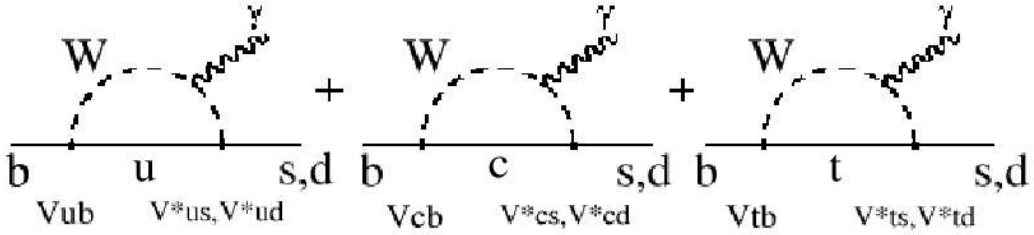

Figure 2.8: Components of SM amplitude of $b \to s\gamma$ and $b \to d\gamma$.

bution are:

$$A_s = A(m_u^2 V_{ub} V_{us}^* + m_c^2 V_{cb} V_{cs}^* + m_t^2 V_{tb} V_{ts}^*) \tag{2.46}$$

$$A_d = A(m_u^2 V_{ub} V_{ud}^* + m_c^2 V_{cb} V_{cd}^* + m_t^2 V_{tb} V_{td}^*). \tag{2.47}$$

The amplitudes A_s and A_d depend only on mass, as their flavour dependence can be removed by factoring out CKM phases. Note that from unitarity conditions (similar to Equation 2.10):

$$V_{ub} V_{us}^* + V_{cb} V_{cs}^* + V_{tb} V_{ts}^* = 0 \tag{2.48}$$

$$V_{ub} V_{ud}^* + V_{cb} V_{cd}^* + V_{tb} V_{td}^* = 0 \tag{2.49}$$

Thus if $m_u = m_c = m_t$, then $A_{s,d}$ would be zero. This is known as GIM suppression, and the greater the similarity between the three masses the greater the suppression of the decay amplitude. Since $m_t \gg m_c, m_u$, the amplitudes A_s and A_d are essentially proportional to m_t^2.

The absence of a dominant tree level contribution, small branching fractions and the large mass of the loop propagators make the amplitudes of penguin transitions highly susceptible to interference from new physics interactions. Many theoretical extensions to the Standard Model, including super-symmetric theories, involve new particles and couplings that lead to one-loop contributions similar to that in Figure 2.7 but with non-SM particles appearing in the loop (see Figure 2.9). For example, the W may be replaced by a charged Higgs boson, or both the quark and W may be replaced by their SUSY partners, a squark and chargino or neutralino. Such contributions could alter the decay amplitude.

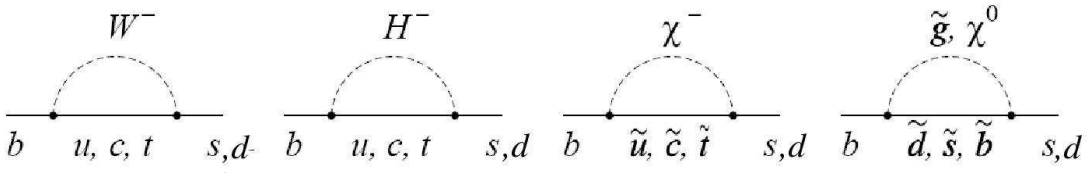

Figure 2.9: The Standard Model radiative penguin Feynman diagram (far left), and possible non-SM contributions to the loop.

While important as an indicator of new physics, radiative penguin decays also provide important independent constraints on SM parameters. One of the most important measurements is the ratio of CKM matrix elements $|\frac{V_{td}}{V_{ts}}|$ measured from the ratio of branching fractions $\frac{b\to d\gamma}{b\to s\gamma}$, which is currently constrained by measurements of B_d and B_s mixing [27].

2.5.1 Effective field theory

Quark flavour physics is governed by the interplay of strong and weak interactions. The influence of the strong interaction makes theoretical prediction of observables difficult, as no accurate estimates are available in quantum field theory for matrix elements dominated by long distance strong interactions. The resulting hadronic uncertainties greatly restrict the predictive reach of flavour physics, especially in the search for new physics.

Quark confinement makes direct experimental measurements of $b \to s\gamma$ or $b \to d\gamma$ transitions impossible, but hadronic manifestations of the quark transitions can be observed and measured. Conveniently, the decay width $\Gamma(B \to X_{s,d}\gamma)$ is well approximated by the partonic decay rate $\Gamma(b \to s, d\gamma)$ through the relation:

$$\Gamma(B \to X_{s,d}\gamma) = \Gamma(b \to s, d\gamma) + \Delta^{non-pert.} \tag{2.50}$$

$\Delta^{non-pert.}$ can be understood - since the b-quark mass is much larger than the typical scale of the strong interaction, long-distance non-perturbative strong interactions can be brought under control with Heavy Quark Theory (HQT), as will be explained later in this section.

For rare B decays, the basic experimental observable of interest (besides the existence of the decay) is the branching fraction (BF) - the fraction of B mesons that will decay to final states X. The BF is related to the commonly calculated theoretical parameter 'partial width', or partial transition rate, as follows:

$$BF(B \to X) = \frac{\Gamma(B \to X)}{\Gamma(B)} = \tau_B \Gamma(B \to X) \tag{2.51}$$

where $\Gamma(B) = 1/\tau_B$ is the B full width, and τ_B is the mean B lifetime.

The basic framework for theoretical calculations of partial width is an Operator Product Expansion (OPE) of the Standard Model. In this effective field theory for B mesons, the transition amplitude is separated into two parts - long distance and short distance contributions.

In a B meson, the heavy quark is surrounded by a complicated, strongly interacting cloud of light quarks, anti-quarks and soft gluons. The Compton wavelength of the heavy quark ($\lambda_Q \approx 1/m_Q$) is much smaller than the size of the hadron ($R_{had} \approx 1/\Lambda_{QCD}$), and the soft gluons exchanged by the heavy quark and light constituents can only be resolved over distances much larger than λ_Q. Thus the light constituents are blind to the flavour, mass and spin of the heavy quark and experience only its colour field. Hadronic bound states are therefore characterised by a large separation of mass scales. HQT aims to separate the

physics associated with these two scales using OPE so that the dependence on the heavy quark mass becomes explicit.

Long distance physics (with energy scale smaller then μ, usually taken to be $\leq 1\,\mathrm{GeV}$) are described by local operators $Q_i(x)$. The matrix elements of the operators must be determined from non-perturbative methods, such as lattice QCD.

Short distance physics (energy scale greater than μ) are described by effective coupling strengths, calculated in perturbation theory and renormalisation group techniques. These are the Wilson coefficients, $C_i(\mu)$, which can be treated as coupling constants. Their μ-dependence is governed by the renormalisation group expansion, and so these can be calculated at large scales using a perturbative method and then extrapolated down to the energy scale of μ.

The most important operators for radiative penguin decays are the current-current operators:

$$Q_1^p(\mu) = (\bar{q}_\alpha \gamma_\mu (1-\gamma_5) p_\beta)(\bar{p}_\beta \gamma^\mu (1-\gamma_5) b_\alpha) \tag{2.52}$$

$$Q_2^p(\mu) = (\bar{q}_\alpha \gamma_\mu (1-\gamma_5) p_\alpha)(\bar{p}_\beta \gamma^\mu (1-\gamma_5) b_\beta) \tag{2.53}$$

and the electromagnetic and chromomagnetic penguin operators:

$$Q_7(\mu) = \frac{e m_b}{8\pi^2}(\bar{q}_\alpha \sigma^{\mu\nu}(1+\gamma_5) b_\alpha) F_{\mu\nu} \tag{2.54}$$

$$Q_8(\mu) = \frac{g_s m_b}{8\pi^2}(\bar{q}_\alpha \sigma^{\mu\nu}(1+\gamma_5) T^a_{\alpha\beta} b_\beta) G^a_{\mu\nu}. \tag{2.55}$$

$F_{\mu\nu}$ and $G^a_{\mu\nu}$ are the electromagnetic and gluonic field strength tensors respectively; $T^a_{\mu\nu}$ are the colour $SU(3)$ group generators, α and β are colour indices, and a is the gluonic colour index. Q_7 is dominant, and other operators related to these decays make a smaller, but not negligible, contribution. The annihilation operator, shown in Figure 2.12, is a non-negligible contribution to the $b \to d\gamma$ decay.

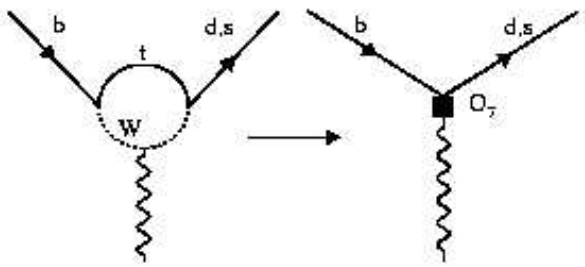

Figure 2.10: The penguin diagram contributions to Q_7

.

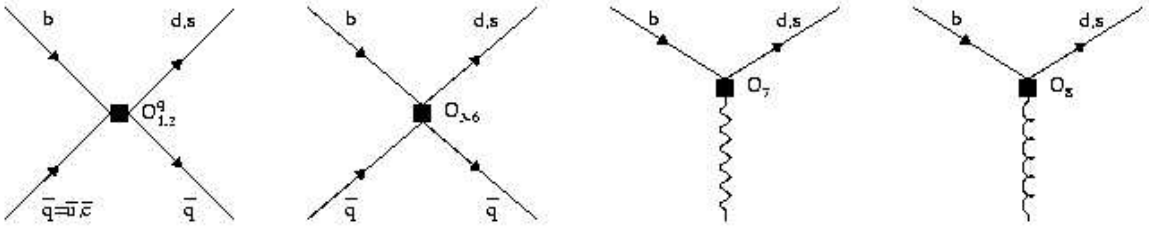

Figure 2.11: The local operators of the OPE effective theory of B meson decay.

2.5.2 $b \to s\gamma$ and $b \to d\gamma$

The branching fraction of the exclusive $b \to d\gamma$ decays $B \to (\rho, \omega)\gamma$ can be related to the SM parameter $|V_{td}|$, but the large theoretical uncertainty involved in calculating the form factor makes extraction from a direct measurement difficult. As some systematic errors cancel in the ratio of form factors $\zeta = F_{B\to(\rho,\omega)\gamma}/F_{B\to K^*\gamma}$, the ratio of exclusive branching fractions $BF(B \to (\rho, \omega)\gamma)/BF(B \to K^*\gamma)$ can be used to calculate the ratio $|\frac{V_{td}}{V_{ts}}|$ with much less theoretical uncertainty [19].

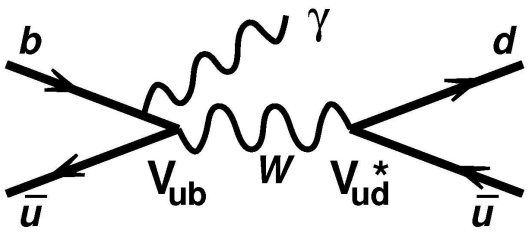

Figure 2.12: The annihilation operator diagram.

This is described by the relations:

$$\frac{BF(B \to (\rho,\omega)\gamma)}{BF(B \to K^*\gamma)} = |\frac{V_{td}}{V_{ts}}|^2 \left(\frac{1 - m^2_{\rho,\omega}/M^2_B}{1 - m^2_{K^*}/M^2_B}\right)^3 \zeta^2[1 + \Delta R] \tag{2.56}$$

where $m_{\rho,\omega}$, m_{K^*} and M_B are the masses of the ρ, ω, K^* and B mesons respectively, ζ is the ratio of transition form factors and ΔR parameterises the remaining small dynamical differences, mainly contributions from annihilation and four-quark operators. Annihilation operator effects are significant for B^+ decays but not B^0 decays, so separating B^+ and B^0 decays can help to understand this contribution.

At present, no theoretical calculations exist for the ratio of inclusive decays. In general, the inclusive channel is less sensitive to hadronic physics as no account need be taken of the resonant structure of the decay. Some corrections ought to be made for the s-quark mass, but the inclusive ζ parameter should be of less significance than that of the exclusive channels.

The annihilation/combination parameter ΔR will not be dealt with so easily. As it only contributes to the B^+ decays, it should eventually be possible to separate B^+ and B^0 decay modes to examine the contribution of this factor in more detail.

A direct measure of $|\frac{V_{td}}{V_{ts}}|$ is important for confirming the unitarity of the CKM matrix. The ratio can also be determined from $B_{d,s}$ mixing:

$$\frac{\Delta m_{B_d}}{\Delta m_{B_s}} = \frac{m_{B_d}\widehat{B}_d f_{B_d}}{m_{B_s}\widehat{B}_s f_{B_s}} . \frac{|V_{td}|^2}{|V_{ts}|^2} \tag{2.57}$$

with the mass difference $\Delta m_{B_{d,s}}$ and the form factors $f_{B_{d,s}}$.

2.5.3 SM predictions

The $b \to s\gamma$ branching fraction has been well-studied in recent years, and has been calculated at next-to-leading order (NLO) to be [2]:

$$BF(B \to X_s\gamma)_{E_\gamma > 1.6\,\mathrm{GeV}} = (3.60 \pm 0.3) \times 10^{-4}. \tag{2.58}$$

Calculations	[19]	[20]
$BF(B^0 \to \rho^0\gamma)$ $(\times 10^{-6})$	0.66 $\pm$0.20	$0.76^{+0.26}_{-0.23}$
$BF(B^+ \to \rho^+\gamma)$ $(\times 10^{-6})$	1.35 $\pm$0.42	$1.58^{+0.53}_{-0.46}$

Table 2.2: Next-to-leading order theoretical predictions of $B^0 \to \rho^0\gamma$ and $B^+ \to \rho^+\gamma$ decays. The value of $BF(B^0 \to \omega\gamma)$ is theoretically predicted by isospin symmetry to be equal to that of $B^0 \to \rho^0\gamma$.

The theory error has three main sources - parametric, perturbative and non-perturbative. The parametric uncertainties are due to uncertainties associated with the input parameters. Perturbative uncertainties have been dramatically reduced due to calculations of the NLO QCD contributions, and the uncertainties in this prediction mainly come from NNLO corrections which are currently being calculated. Non-perturbative effects become more significant in the high mass region, which is one motivation for the low photon energy cut-off in experimental measurements. Theoretical predictions for the $B \to (\rho, \omega)\gamma$ decay rates are given in Table 2.5.3.

Direct *CP* asymmetry is another measurement of interest in radiative penguin decays. The SM predicts it to be small in $b \to s\gamma$ decays ($\approx 1\%$), and large in $b \to d\gamma$ decays ($\approx 15\%$) [26][19]. The sum $A_{CP}(b \to (s+d)\gamma) \approx 0$. Direct *CP* asymmetry in the $b \to s\gamma$ system is small, and it is unlikely that the experimental precision will challenge the theoretical uncertainties in the near future. However, as $A_{CP}(b \to d\gamma)$ is expected to be large, deviations from the SM predictions would be a clear sign of new physics.

2.6 Current experimental results

The first evidence for any radiative penguin decay of a B meson was the observation of the exclusive $B \to K^*\gamma$decay, published by the CLEO collaboration in 1993 [18]. Since then, measurements continue to be refined with increasing data sets.

	BABAR[25] Semi-inclusive, 89×10^6 $B\bar{B}$ pairs	BELLE [24] Fully-inclusive, 155×10^6 $B\bar{B}$ pairs	Theory prediction [2]
$BF(b\to s\gamma)(\times10^{-4})$	$3.31\pm0.19^{+0.64}_{-0.42}$	$3.55\pm0.32^{+0.30+0.11}_{-0.31-0.07}$	3.60 ± 0.3

Table 2.3: The most recent experimental results of semi-inclusive $b\to s\gamma$ decay branching fractions.

2.6.1 $b\to s\gamma$

In 2005, *BABAR* published a measurement of the $b\to s\gamma$ branching fraction using a semi-inclusive technique [25]. A fully inclusive measurement does not reconstruct the hadronic part of the decay, but rather measures the energy spectrum of the photon. A semi-inclusive analysis uses a sum-of-exclusive modes approach to approximate the inclusive measurement - the more exclusive modes included, the closer the approximation to the inclusive decay. The semi-inclusive approach has a number of advantages. One can examine the exclusive modes individually to measure their branching fractions and *CP*-asymmetry as well as the combined branching fraction and asymmetry. There are more theoretical errors associated with a semi-inclusive BF measurement, mainly in the uncertainties related to the fraction of decays not reconstructed, but experimentally it is a cleaner result.

The *BABAR* analysis described in [25] used a sum of 38 exclusive modes. The hadronic mass range M_{Xs} covered 0.6-2.8 GeV, corresponding to a minimum photon energy of $E_\gamma > 1.9$ GeV and the analysis used a dataset of 89 million $B\bar{B}$ pairs. The photon energy spectrum is shown in Figure 2.13.

The branching fractions, together with a recent Belle measurement using a fully-inclusive technique, are given in Table 2.3. The theoretical prediction is given for comparison and shown in Figure 2.14. It is clear that there is no significant discrepancy between theory and experimental measurements of the branching fraction, and it should be noted that the experimental error on $b\to s\gamma$ is now on a par with the theory error and will become yet smaller in the next generation of analyses.

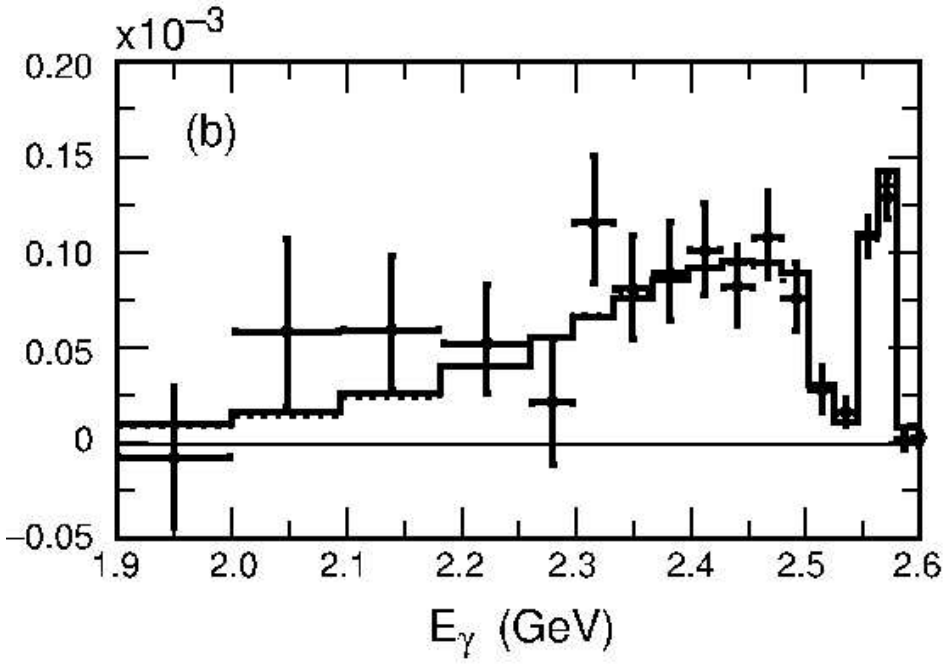

Figure 2.13: High-energy γ energy spectrum for $b \to s\gamma$, showing the K^* resonance at high E_γ and the energy cutoff at 1.9 GeV. E_γ is calculated from the hadronic mass.

2.6.2 $b \to d\gamma$

In 2004, *BABAR* published upper limits on the branching fractions of the exclusive $b \to d\gamma$ modes $B \to (\rho, \omega)\gamma$ [22]. The analysis reconstructed $B^+ \to \rho^+\gamma$ with $\rho^+ \to \pi^+\pi^0$, $B^0 \to \rho^0\gamma$ with $\rho^0 \to \pi^+\pi^-$ and $B^0 \to \omega\gamma$ with $\omega \to \pi^+\pi^-\pi^0$. The full dataset from 1999 - 2004 was used, containing 211 million $B\bar{B}$ pairs and the upper limits found were as given in Table 2.4. Belle published evidence of first observation of the $B \to (\rho, \omega)\gamma$ combined decays in 2005 [21] with 350 million $B\bar{B}$ pairs. The measured branching fraction and resulting value for $|\frac{V_{td}}{V_{ts}}|$ are shown for comparison in Table 2.4 and Figure 2.15 with the theory predictions. Results from Belle and *BABAR* for $BF(B^0 \to \rho^0\gamma)$ differ significantly. The Belle measurement of $BF(B \to (\rho, \omega)\gamma)$ agrees with the Standard Model within errors, but it is intriguing that the central values of the exclusive modes are at odds with the SM expectation that charged mode be greater than the neutral mode.

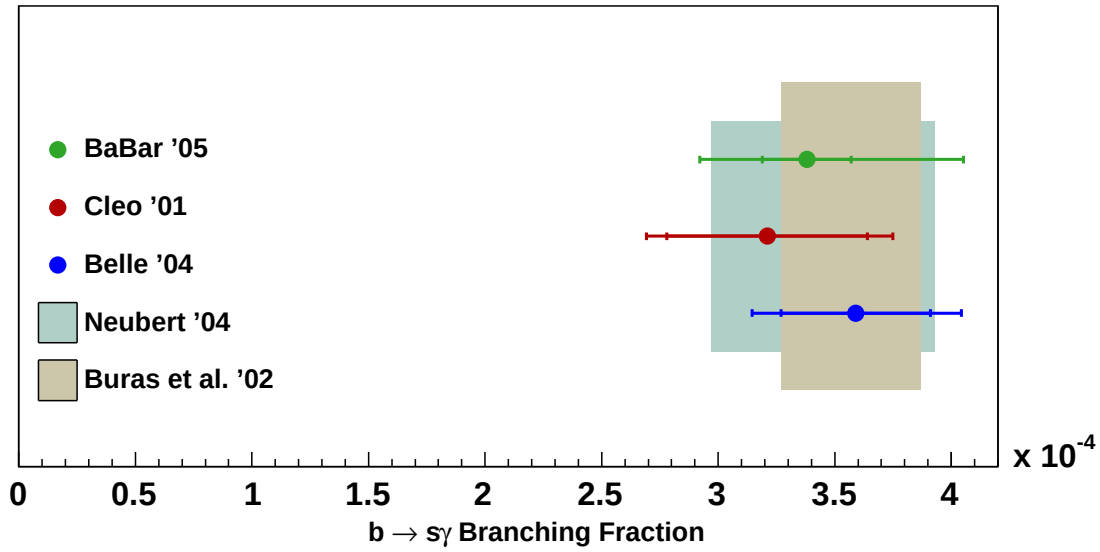

Figure 2.14: Recent experimental results of the $b \to s\gamma$ branching ratio.

	BABAR[22] 211×10^6 $B\bar{B}$ pairs	BELLE [21] 350×10^6 $B\bar{B}$ pairs	World Average	Theory predictions [19]
$BF(B^+ \to \rho^+\gamma)(\times10^{-6})$	$0.9^{+0.6}_{-0.5} \pm 0.1$	$0.55^{+0.43+0.12}_{-0.37-0.11}$	$0.68^{+0.36}_{-0.31}$	
$BF(B^0 \to \rho^0\gamma)(\times10^{-6})$	$0.0 \pm 0.2 \pm 0.1$	$1.17^{+0.35+0.09}_{-0.31-0.08}$	0.38 ± 0.18	
$BF(B^0 \to \omega\gamma)(\times10^{-6})$	$0.5 \pm 0.3 \pm 0.1$	$0.58^{+0.35+0.07}_{-0.27-0.08}$	$0.54^{+0.23}_{-0.21}$	
$BF(B \to (\rho,\omega)\gamma)(\times10^{-6})$	$0.6 \pm 0.3 \pm 0.1$	$1.34^{+0.34+0.14}_{-0.31-0.10}$	0.96 ± 0.23	1.38 ± 0.42
$\lvert\frac{V_{td}}{V_{ts}}\rvert$	<1.9	$0.200^{+0.026+0.038}_{-0.025-0.029}$		0.18-0.22

Table 2.4: Recent experimental results of exclusive $b \to d\gamma$ decay branching fractions.

This may be the first hint of physics beyond the standard model in $b \to d\gamma$, the details of which will be revealed with further studies.

2.6.3 Measurements of $|\frac{V_{td}}{V_{ts}}|$

Just before this thesis was completed, the first direct measurement of the $B_s^0 - \bar{B}_s^0$ oscillation frequency was announced by the CDF collaboration. Δm_s was measured to be $17.33^{+0.42}_{-0.21}(\text{stat.}) \pm 0.07(\text{syst.})\text{ps}^{-1}$. This gives a measurement of $|\frac{V_{td}}{V_{ts}}| = 0.208^{+0.008}_{-0.007}$ [27], which is in agreement with the BELLE result given in Table 2.4. Figure 2.16 shows the new constraints on $|\frac{V_{td}}{V_{ts}}|$ graphically [28]. The orange circle

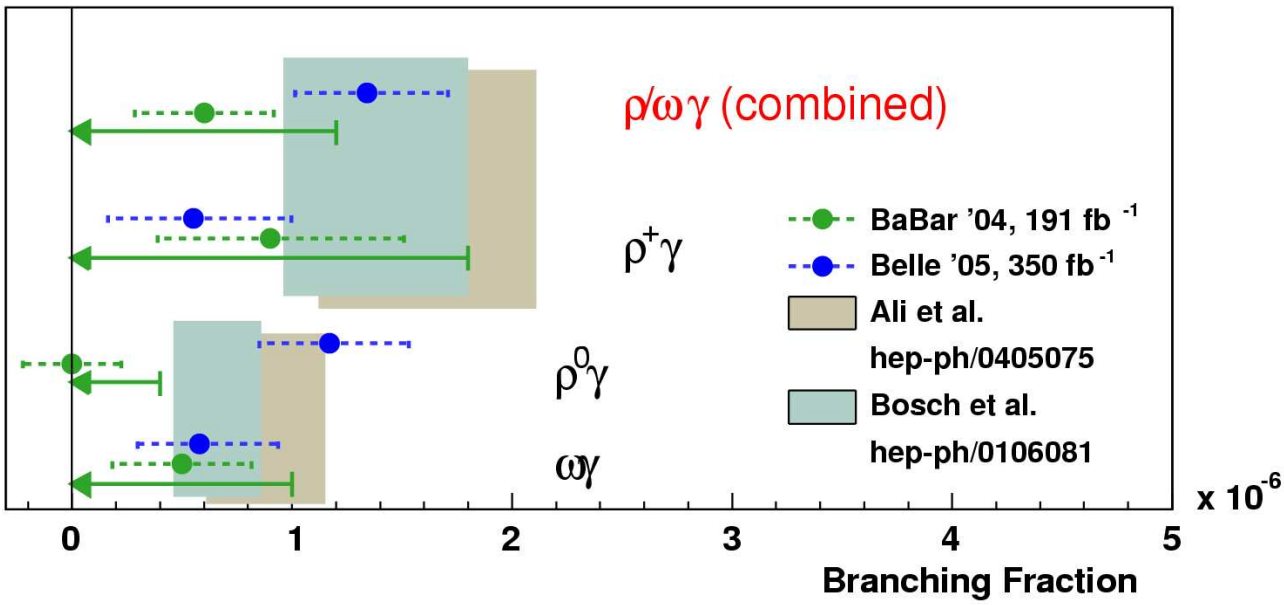

Figure 2.15: Recent experimental results of the exclusive $b \to d\gamma$ branching fractions.

shows the new constraints, compared with using Δm_d only (represented by the yellow circle).

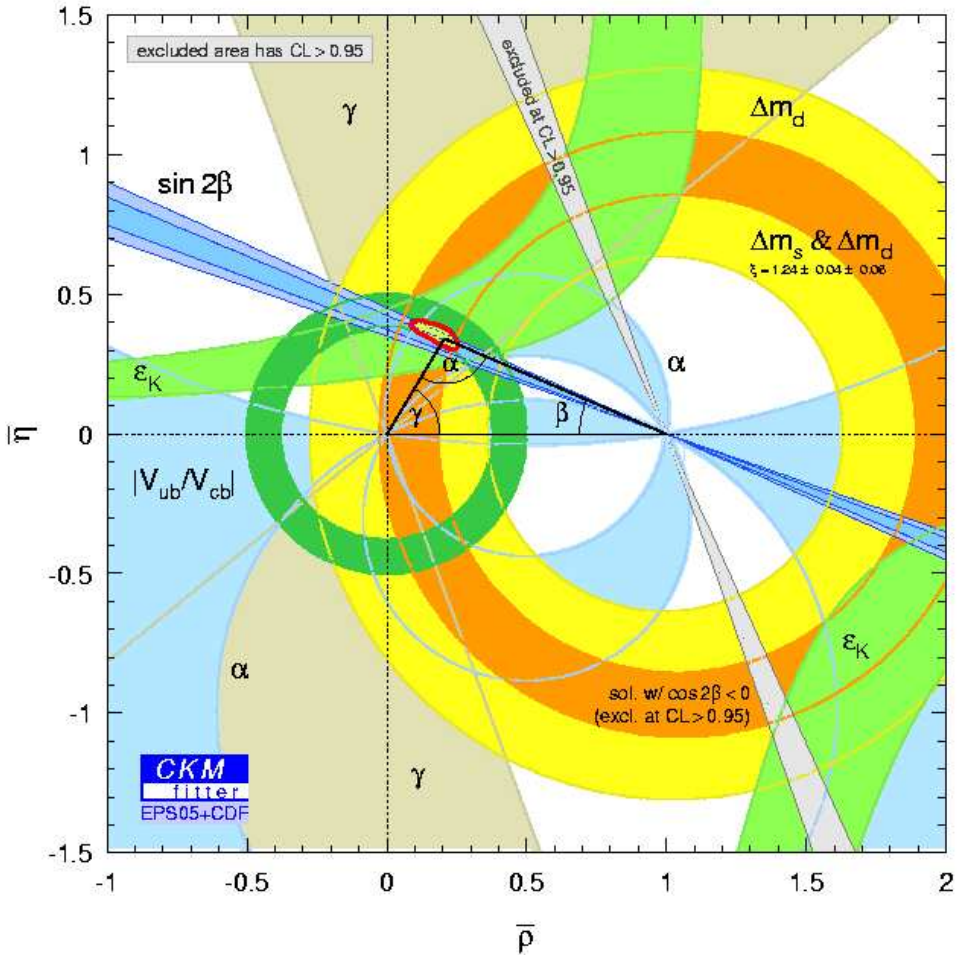

Figure 2.16: Constraints on the Unitarity Triangle including new B_s mixing results.

Chapter 3

PEP-II and the *BABAR* detector

3.1 Introduction

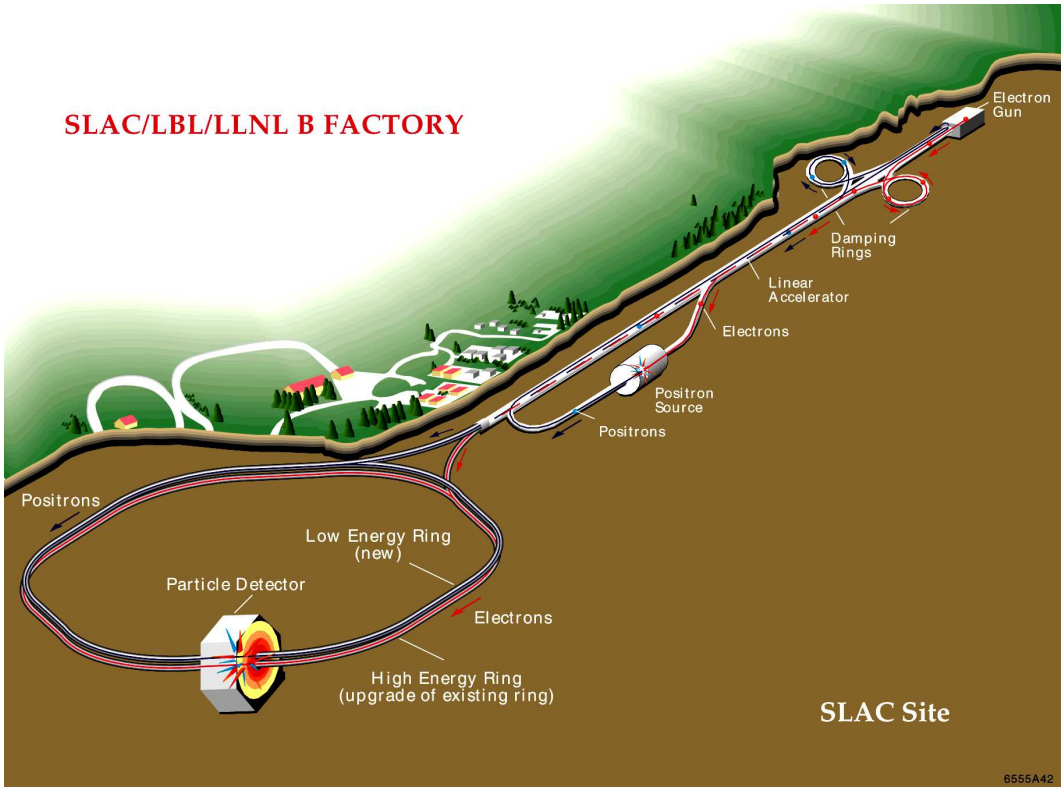

Figure 3.1: The PEP-II B-factory.

PEP-II is an asymmetric e^-e^+ collider, dubbed a "B-factory" because it is designed to produce a large number of B particles (Figure 3.1). Electrons and positrons are collided with a centre of mass energy of 10.58 GeV, corresponding

to the $\Upsilon(4S)$ resonance, which decays almost exclusively into $B\bar{B}$ pairs. As the mass of the $\Upsilon(4S)$ lies just above the $B\bar{B}$ production threshold, the daughter Bs are almost at rest in the $\Upsilon(4S)$ rest frame and do not travel far before decaying. The two B mesons have uncorrelated decay axes, so the daughters of one B are distributed isotropically with respect to the other.

Approximately 10% of collisions are produced during off-resonance running, with a centre of mass energy 40 MeV below the $\Upsilon(4S)$ peak. At this energy, B meson production is kinematically suppressed, but all other background particles are produced as usual, yielding a valuable control sample of $e^+e^- \to u\bar{u}$, $d\bar{d}$, $s\bar{s}$, $c\bar{c}$ (collectively called 'continuum') and $\tau^+\tau^-$ events. Continuum decays also tend to have larger momentum in the centre of mass frame, resulting in a jet-like distribution of daughters and allowing discrimination between B and background decays.

Accurate determination of decay vertices and B decay lifetimes are vital in CP asymmetry measurements. These are difficult to measure when the centre of mass frame is close to the lab frame, so an asymmetric machine was built. The high energy ring (HER) e^- beam has an energy of 9 GeV, and the low energy ring (LER) e^+ beam 3.1 GeV, giving the $\Upsilon(4S)$ a boost of $\beta\gamma$=0.56 in the laboratory frame. This results in measurable B decay lengths of $\approx$250 μm.

3.1.1 PEP-II

Electrons are produced with a polarised electron gun and accelerated in bunches down the 3km linear accelerator (linac) by a series of klystrons. The klystrons produce microwaves which create oscillating electric and magnetic fields in the copper cavities of the linac, synchronised with the arrival of the bunches to provide optimal acceleration. Some electrons are diverted from the linac to collide with a tungsten target to produce e^+e^- pairs. The positrons are collected and returned to the start of the linac where they are then accelerated, out of phase with

the electrons. Once the electrons and positrons have reached energies of 9 GeV and 3.1 GeV respectively, they are injected in opposite directions into the 800m diameter PEP-II storage rings, and collided head-on at the interaction point (IP).

When the two beams collide, the vast majority of the particles in each bunch pass by each other without anything happening. Particles are lost through e^+e^- collisions, residual beam-gas interactions and as they hit the beam pipe when traveling around the PEP-II ring. This results in a finite beam lifetime of 2 - 4 hours, with beam luminosity slowly decreasing as beam current is lost. The traditional solution to this problem has been to inject particles from the Linac while the detector is turned off until the rings are fully replenished, then taking data while 'coasting' for about 40 minutes with gradually decreasing luminosity. This is an inefficient process and does not take advantage of the full luminosity PEP-II can provide.

Trickle injection is the process of continuously injecting particles into the rings, whilst the detector is taking data. This requires a very clean injection and was implemented for the LER e^+ beam in November 2003. Efficiency improved by 30% within a few days. Continuous injection into the HER e^- ring began in March 2004. Currently, both rings are able to operate trickle injection with an additional 20% improvement of efficiency. The SLAC linac is capable of up to 40 e^+ and 40 e^- injection pulses per second (although fewer are actually needed). This gives true trickle injection with both electron and positron beam current stability better than 0.1%. Data-taking efficiency has been improved by just over 50%. The *BABAR* luminosity records to date are given in Table 3.1.

Time period	Integrated luminosity (*BABAR* recorded)
shift (8 hours)	239.6 pb^{-1}
day	681.08 pb^{-1}
week	4.117 fb^{-1}
month	16.05 fb^{-1}

Table 3.1: *BABAR* luminosity records.

3.2 The *BABAR* detector

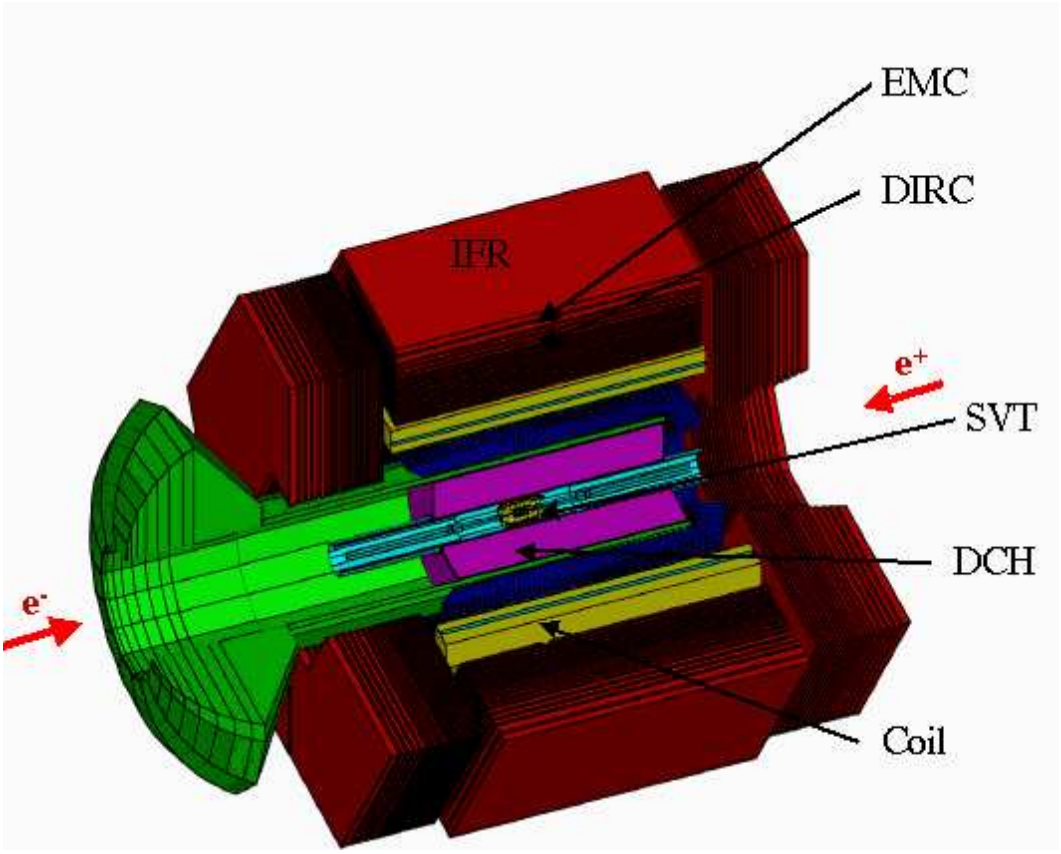

Figure 3.2: The *BABAR* detector.

The *BABAR* detector consists of 5 sub-detectors and a superconducting magnet, shown in Figure 3.2 and described in the following sections.

The detector was designed to cover the maximum possible acceptance angle in the centre of mass frame and therefore it is asymmetric about the interaction point with most detectors covering the forward end-cap as well as the barrel. It needs to have excellent vertex resolution, which is important in the measurement of particle lifetimes. It must accurately track charged particles as they pass through the detector sub-sections over a large momentum range (0.06 GeV/c - 4 GeV/c). Particle identification is very important, especially differentiating between pions and kaons at high momentum (which is particularly relevant for the $b \to d\gamma$

analysis). Finally, it must be able to detect neutral particles such as γs and π^0s and successfully identify muons and electrons.

3.2.1 The Silicon Vertex Detector (SVT)

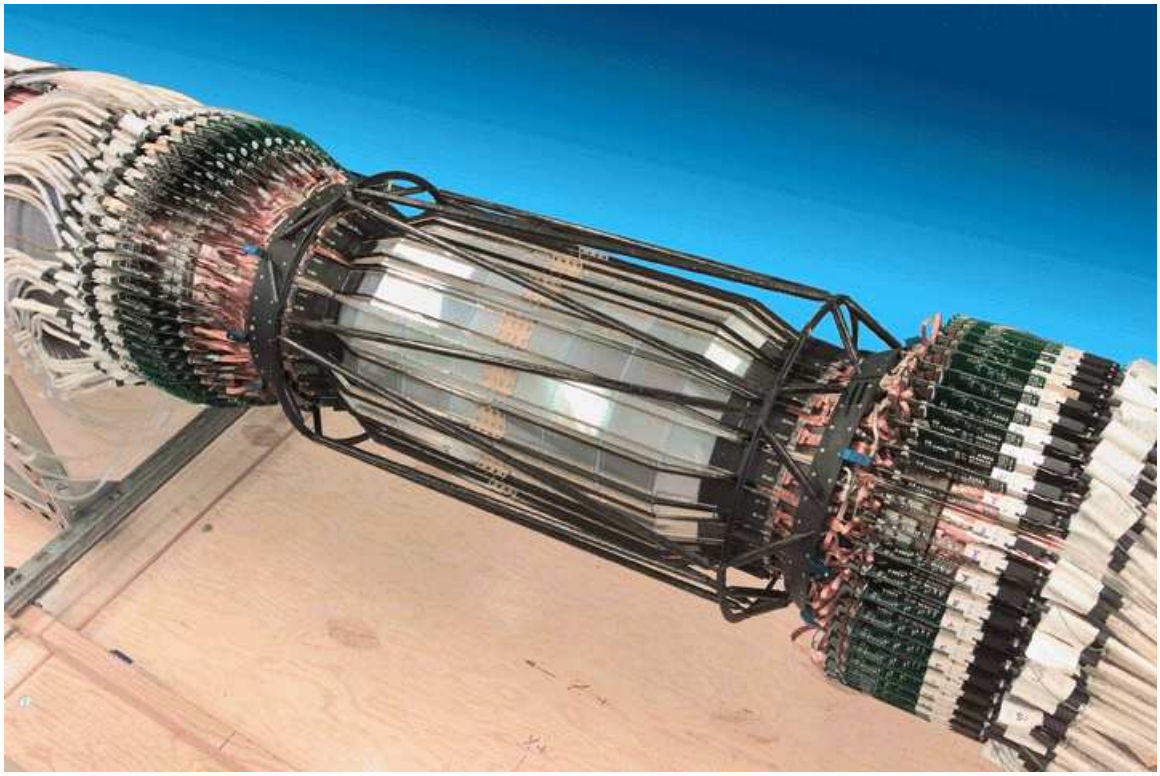

Figure 3.3: The *BABAR* silicon vertex tracker.

The innermost part of the detector is the Silicon Vertex Detector. It sits between the beam pipe and the beam support tube and measures the two B decay vertices, the impact parameter information from the resulting tracks and initial track angles. Because of the 1.5T magnetic field, particles with transverse momentum less than 100 MeV/c do not reach the Drift Chamber and for these it provides all tracking data. It needs to have excellent resolution in both longitudinal and transverse directions, especially near the interaction point, in order to measure decay vertex distances and identify decay cascades. The SVT must also be able to withstand high doses of ionising radiation, measured at 1 Rad/day in

the inner layers and 0.1 Rad/day in the outer layers.

Hardware

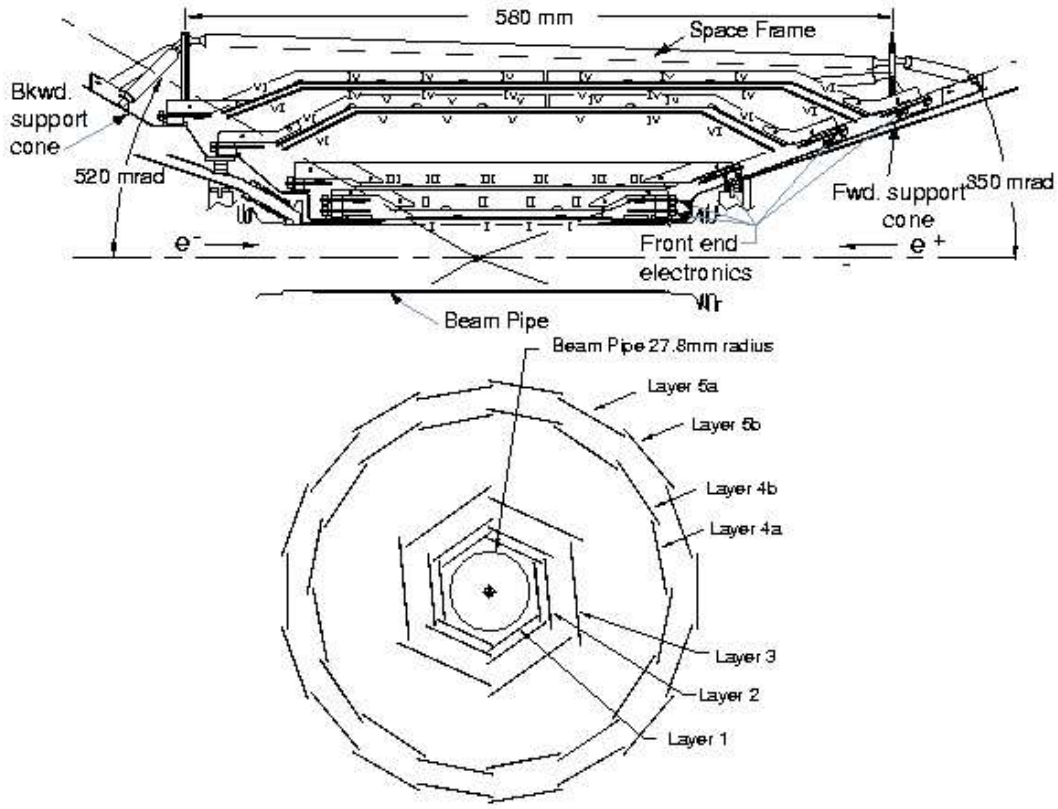

Figure 3.4: Cross-sectional view of the SVT.

The SVT consists of 5 layers of double-sided silicon micro-strip detectors with 90^o stereo. The inner 3 layers consist of 6 modules in ϕ, arranged in a barrel pinwheel formation. The 2 outer layers contain 16 and 18 modules, in an arched overlap formation (as shown in Figure 3.4) to ensure all silicon is perpendicular to tracks coming from the IP and to minimise the amount of silicon required to cover the solid angle. They are supported on Kevlar ribs and then encased in a carbon fibre support tube. The solid angle covered is limited by the beam optics, electronics and cabling in the beam pipe so much of this material has been placed in the backward direction to maximise acceptance in the forward direc-

tion. It covers the polar angle 20.1^o to 150.2^o - this corresponds to a geometrical acceptance of 90% in the centre of mass system.

There is $0.94\,\mathrm{m}^2$ of silicon in the SVT and 340 silicon detectors in total. The readout is performed by radiation hard integrated circuits, mounted on hybrid circuits which provide power and communication with the Data Acquisition (DAQ) and the cooling systems.

Performance

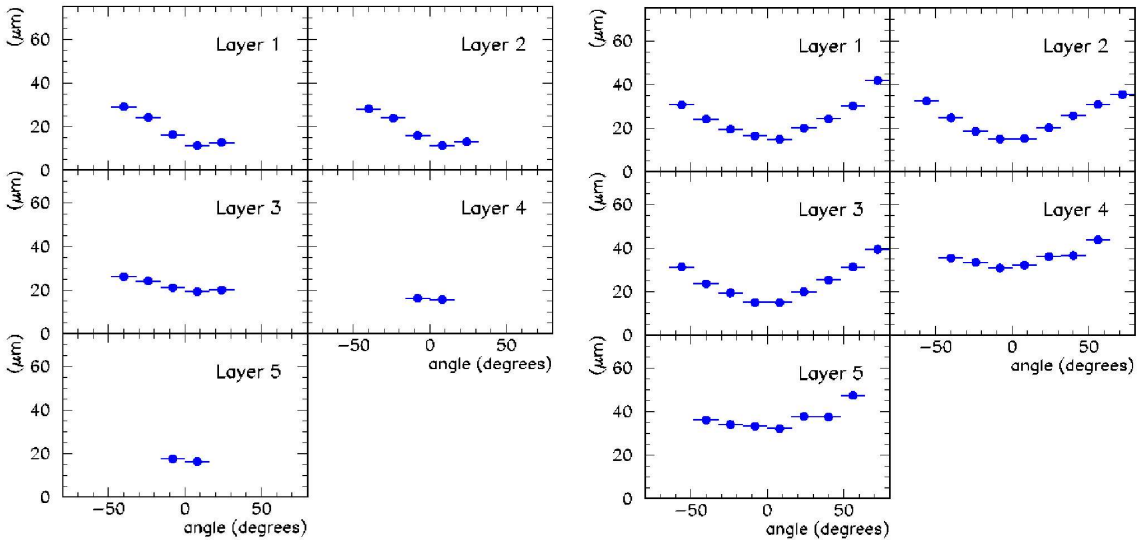

Figure 3.5: The SVT single point resolution in phi (left) and z (right). Each plot shows the measured resolution in microns (vertical axis) versus the incident angle in degrees (horizontal axis). The incident angle is defined as the angle of the track with respect to the wafer normal, projected onto the relevant view (z or phi).

The spatial resolution of the SVT is calculated by measuring the distance between the track trajectory and the hit, as projected onto the wafer plane along either the z or ϕ direction. The width of this distribution is the resolution, as shown in Figure 3.5. Over the whole SVT, for normal tracks the spatial resolution ranges from 10-15 μm in the inner layers to 30/40 μm in the outer layers.

3.2.2 The Drift Chamber (DCH)

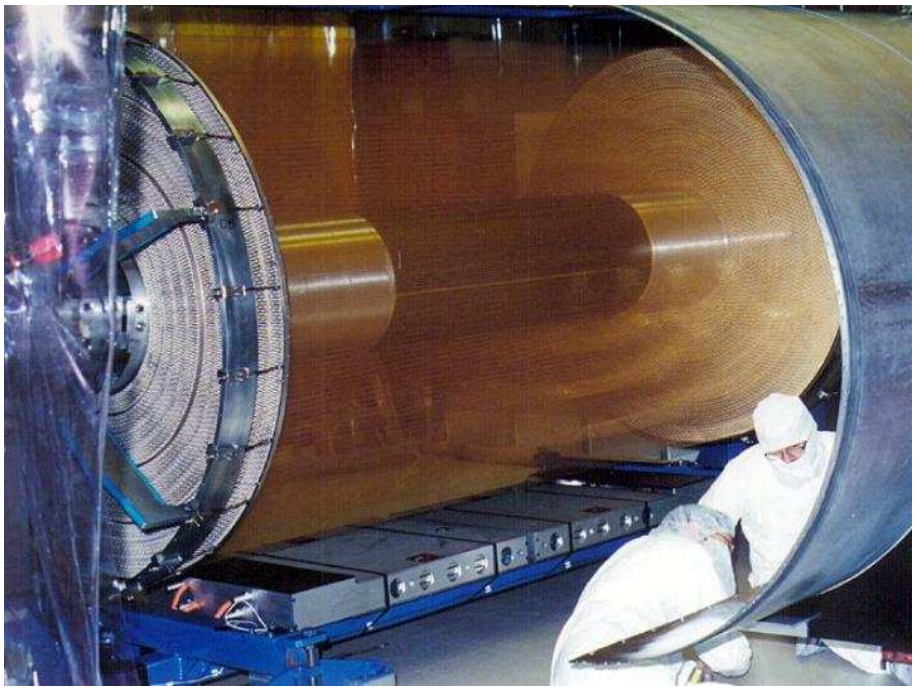

Figure 3.6: The *BABAR* drift chamber during construction.

The drift chamber is the second part of the *BABAR* tracking system, designed to complement the measurements of impact parameter and track direction taken by the SVT. For decays or interactions that occur outside the SVT, the drift chamber provides all tracking information. In addition, for particles with momentum of less than 700 MeV/c that do not reach the Detector of Internally Reflected Čerenkov Radiation or those which pass through the extreme forward and backward parts of the detector, it is the only source of particle identification (PID) which is measured from the ionisation loss dE/dx.

The DCH is therefore required to provide maximal solid angle coverage, good measurement of transverse momentum and excellent resolution of both transverse and longitudinal position. It is capable of K/π separation with a dE/dx resolution of 7% up to 700 MeV/c. The DCH also supplies information to the trigger and has to be able to function under high beam-generated background conditions

(measured up to 5 kHz/cell). The DCH position resolution is about 125 μm in the transverse plane and about 1 mm in the z direction.

Hardware

The DCH is 276 cm long, with an inner radius of 23.6 cm and an outer radius 80.9 cm. The inner wall, made of 1 mm beryllium, is kept thin to ensure good matching of SVT and DCH tracks and to minimise backgrounds. The outer wall is made of a 2 layer carbon fibre on nomex core (covered with aluminium foil for shielding). The end-plates are made of aluminium. The backward end-plate is 24 mm thick and houses most of the electronics. The forward end-plate has a thickness of 24 mm, thinning to 12mm at the edge, in order to present minimal material in front of the EMC. It is positioned asymmetrically with respect to the IP, as *BABAR* events are boosted in the forward direction. It extends 174.9 cm forward and 101.5 cm backward.

The cylinder contains 40 layers of wires strung between the two end-plates and forming 10 super-layers, as shown in Figure 3.7. They are held in a mixture of helium and isobutane gas (4:1). Sequential layers are staggered by half a cell, which enables left-right ambiguity resolution within each super-layer - effectively giving stereoscopic vision. To obtain longitudinal position information, the wires in six of the ten super-layers are positioned with slight tilts towards the z-axis, increasing with radii from $\pm$45 mrad to $\pm$76 mrad. The wires are arranged in hexagonal cells with 20 μm gold-plated tungsten-rhenium sense wires in the centre, at a potential of 1930 volts. These are surrounded by 120 μm and 80 μm field shaping wires, made of gold-plated aluminium at -340V or 0V.

Performance

The precise relation between measured drift time and drift distance is determined from sample e^+e^- and $\mu^+\mu^-$events, with the drift distance estimated from the distance of closest approach of the track to the wire. The estimated drift times

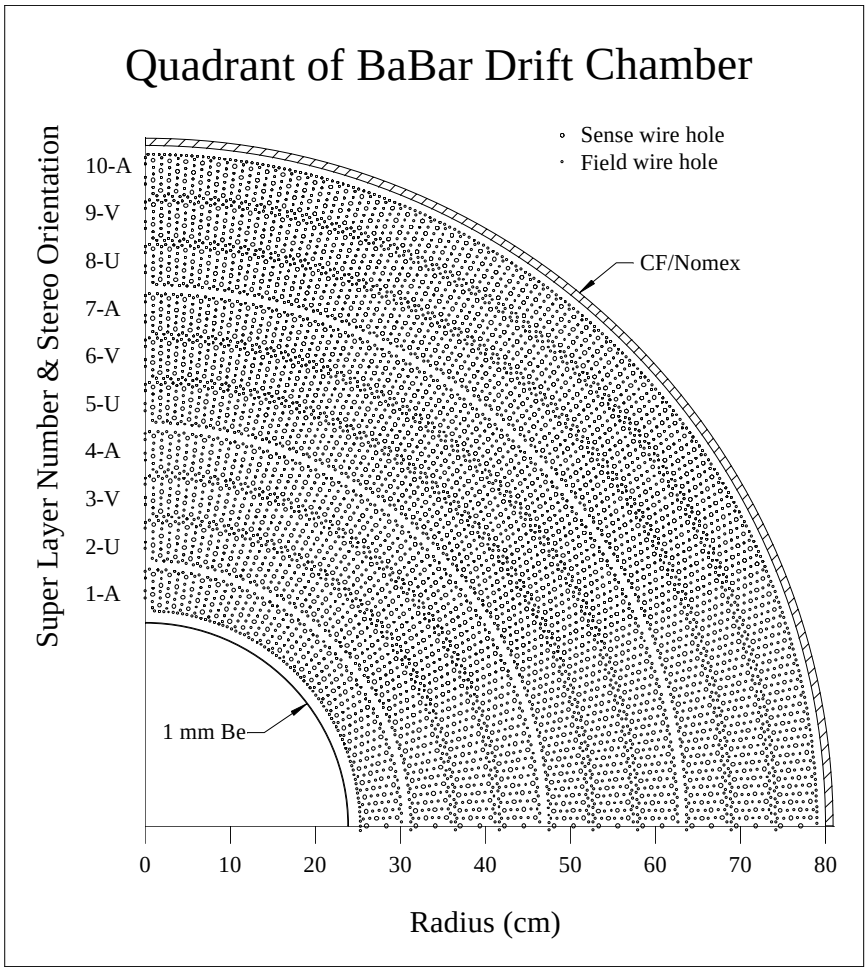

Figure 3.7: Schematic of one DCH quadrant, showing the 40 layers and 10 superlayers.

and the measured drift distances are averaged over all wires in a layer. The reconstruction momentum threshold is about 100 MeV/c, limited by the DCH inner radius. Figure 3.8 shows spatial resolution with respect to drift distance. The average resolution is 125 μm, compared to the original design value of 140 μm.

Specific energy loss (dE/dx) is calculated from the measurement of the total charge collected in each drift cell. Corrections are applied to remove sources of bias, including changes in gas pressure and temperature ($\pm 9\%$ in dE/dx), differences in cell geometry and charge collection ($\pm 11\%$) and signal saturation due to charge build up ($\pm 11\%$). The corrected dE/dx distribution as a function

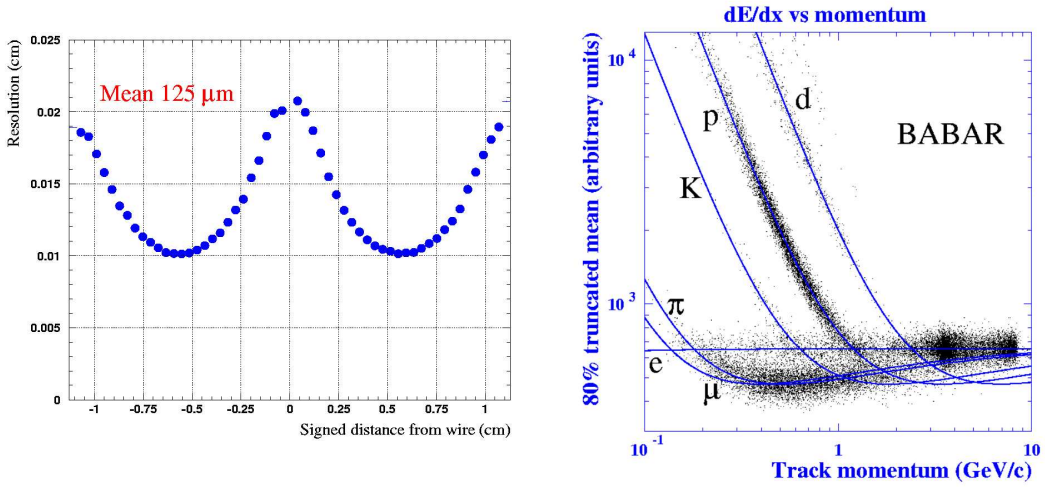

Figure 3.8: Left: the DCH drift resolution as a function of drift distance. Right: dE/dx vs momentum from tracks in the drift chamber, showing Bethe-Bloch parameterisation for various mass hypotheses.

of transverse momentum is shown in Figure 3.8. The dE/dx resolution achieved for Bhabha events is typically 7.5%.

3.2.3 The Detector of Internally Reflected Čerenkov radiation (DIRC)

The DIRC is an innovative detector designed to provide accurate particle identification, which is essential for determining the flavour of B^0 in CP violation studies and for distinguishing between pions and kaons in rare B decays.

When a particle passes through a medium with a speed such that $\beta > \frac{1}{n}$, it emits a cone of Čerenkov radiation with an angle described by the relation:

$$\cos\theta_c = \frac{1}{\beta n} \tag{3.1}$$

where θ_c is the Čerenkov cone opening angle, β is the particle velocity divided by c, the speed of light in a vacuum and n is the refractive index of the material. The DIRC imaging system is based on the total internal reflection (TIR) of Čerenkov photons produced in long quartz bars.

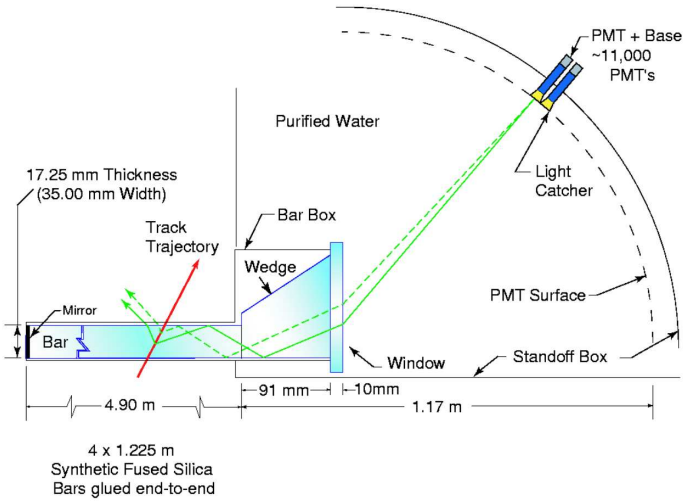

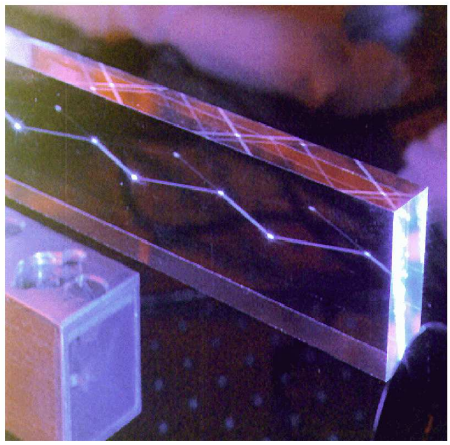

Figure 3.9: Top: The DIRC schematic. Bottom: A blue HeCd laser beam internally reflected in a DIRC bar.

Hardware

The DIRC contains 144 quartz bars, each of the dimensions 1.7 cm x 3.5 cm x 4.9 m; the length is made of 4 x 1225 mm bars glued together. Each bar has high optical quality to minimise losses during TIR. The bars have a refractive index of 1.474 and the surroundings are filled with nitrogen, with a refractive index of about 1 to maximise the total reflection.

Photons incident on the quartz bars are passed to the backward end of the DIRC which preserves θ_c. Mirrors at the front end reflect forward-moving photons

into the instrumented end, which reduces the amount of material in the end-cap before the EMC.

At the backward end of each bar, a trapezoidal quartz wedge folds the Čerenkov ring in half. This wedge is the interface to the standoff box, made of stainless steel and filled with 60000l of purified water. This expands the image which is then detected by 11000 photo-multiplier tubes, as shown in Figure 3.9.

The refractive index of water is very similar to that of quartz, so there is a minimum of reflection at the boundary of the two. Water and quartz also have similar chromacity indices, so dispersion is minimised and the measured angle is consistent with θ_c. The measured radius of the ring gives the velocity and momentum and combined with information of the track angle and momentum from the DCH, an accurate measurement of the mass of the particle is possible.

Performance

The total coverage (in the centre of mass frame) is 87% polar and 96% azimuthal. The position resolution for a track scales as the ratio of the photon Čerenkov angle resolution (σ_γ) with the root of the number of photons detected $N_{pe} \approx 28$ (for a particle of β=1 with perpendicular photon entry).

$$\sigma_{track} = \frac{\sigma_\gamma}{\sqrt{N_{pe}}} \tag{3.2}$$

The angular and time resolutions for a single photon are obtained from di-muon events. $\sigma_\gamma = 10.2\,\text{mrad}$ and the measured time resolution is 1.7 ns, which is close to the 1.5 ns intrinsic response of the PMTs. The track Čerenkov angle resolution for di-muon events is 2.4 mrad, compared to the design goal of 2.2 mrad (see Figure 3.10). The DIRC was designed to achieve a kaon-pion separation resolution of 4σ, but in practice the separation falls below 4σ at around 3 GeV/c and at 4.2 GeV/c it reaches 2.5σ. The different Čerenkov angles of various particle types is shown are Figure 3.11.

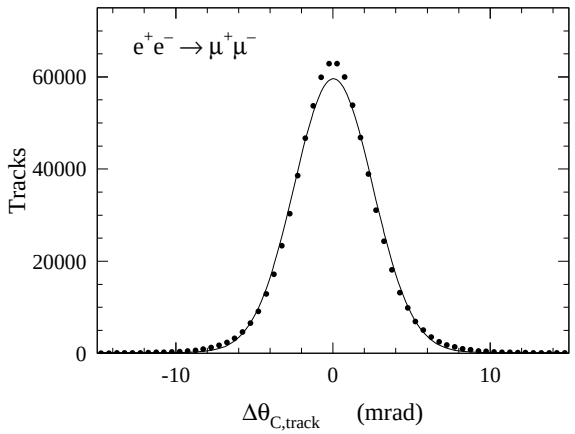

Figure 3.10: Difference between measured and expected Čerenkov angles for single muons, fitted with a Gaussian distribution with width 2.4mrad.

3.2.4 The Electromagnetic Calorimeter (EMC)

In B decays, photons are produced with a very wide range of energies. Approximately half the photons have energy below 200 MeV and very high energy photons of over 3.5 GeV occur in QED processes such as $e^+e^- \to\gamma\gamma$, used in calibration and luminosity measurements. The *BABAR* EMC is designed to detect electromagnetic showers with energies in the range 20 MeV to 9 GeV with excellent efficiency and angular resolution. The lower limit is set by backgrounds and the amount of material in front of the EMC - for this reason it is important that the inner parts of the detector present as little material as possible before the calorimeter. The measurement of rare decays containing π^0s in the final state (such as $B^+ \to \pi^+\pi^0$) sets a stringent requirement on energy resolution of 1-2% at high energies.

Below 2 GeV the energy resolution increases to 4%, which dominates the π^0 mass resolution. Above this limit the angular resolution of a few mrad becomes dominant. The EMC is also used for electron identification, and acts as a complement to the Instrumented Flux Return in detection of μs and K_L^0s.

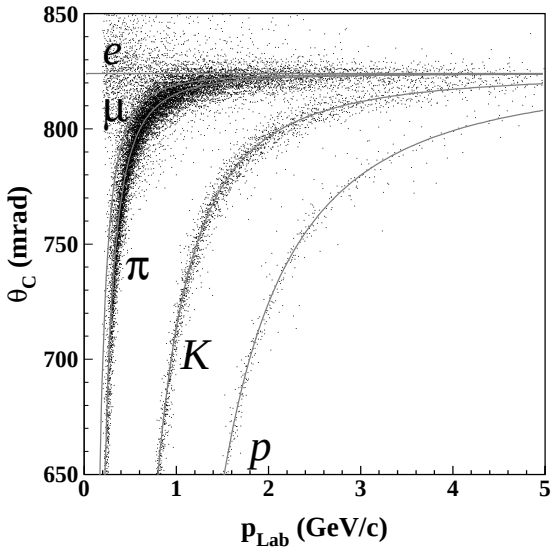

Figure 3.11: Fitted Čerenkov angle of tracks plotted against DIRC entrance momentum.

Hardware

6580 trapezoid thallium doped cesium iodide (CsI(Tl)) crystals (Figure 3.12) are used in the EMC. They are held in a carbon fibre matrix and wrapped in two layers of 150 μm Tyvech 1056D and one layer of 30 μm aluminium foil. This leaves a 1.25 mm gap between crystals, which is non-projective in polar angle θ but projective in azimuthal angle ϕ, giving a 2.5% loss of efficiency. Two large area silicon diodes are attached to the rear of each crystal, which facilitates noise reduction by averaging the contributions from both and also allows for the failure of one. The inner radius of the barrel is 91.9 cm and the outer 135.6 mm and the EMC covers a total angle of $\cos\theta = -0.775$ to 0.962 in the lab frame.

The barrel is positioned so that it extends 2.3 m forward of the interaction point and 1.56 m backward. It is made of 5760 crystals arranged in 48 rings in θ, each containing 120 crystals in ϕ. These are split into 280 modules of 7 x 3 crystals, except for the most backward modules which contains 6 x 3. In total, the barrel weighs 23.5 tons.

The end-cap contains 820 crystals and is supported from the barrel to ensure

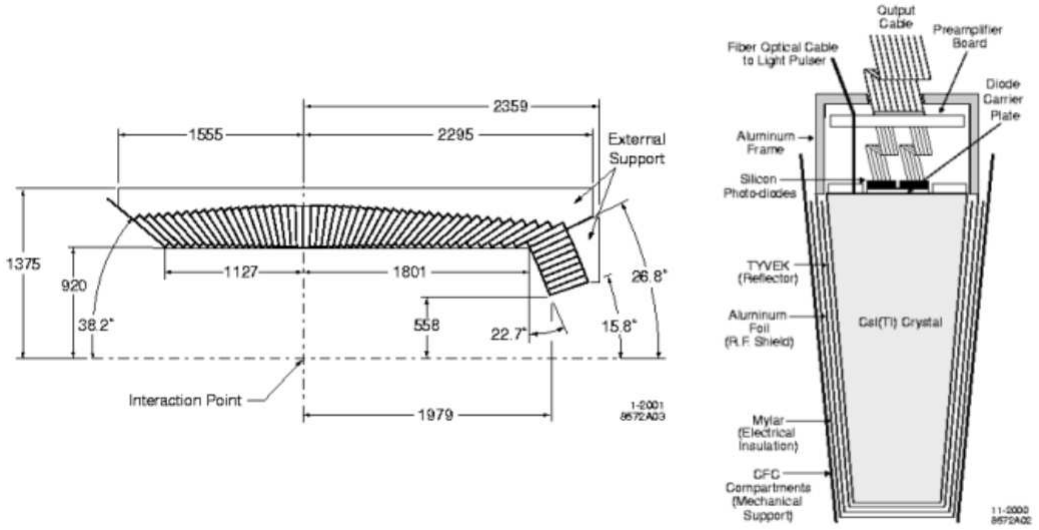

Figure 3.12: Left: The EMC in longitudinal cross-section. Right: Schematic view of one CsI(Ti) crystal with read-out mounted on rear.

good alignment between the two parts. The crystals are arranged in 8 rings in θ. The outermost three rings contain 120 crystals in ϕ, the next three 100 and the inner two rings 80. Inside the innermost ring is a region filled with lead shielding.

Performance

All parts of the detector have charge injection calibration to measure the electronic readout response, but the EMC has two additional calibration sources. A radioactive source calibration is performed via thin pipes at the front of the crystals which are filled with liquid fluorinert. The fluorinert is bombarded with neutrons outside the detector to produce excited oxygen atoms from the fluorine atoms and then circulated. The decaying atoms emit 6.1 MeV photons, giving a calibration constant for each individual crystal.

The other calibration system for the EMC is the light pulser. Two xenon flash lamps illuminate bundles of optical fibres which shine light into the back of every crystal. This gives a global crystal calibration.

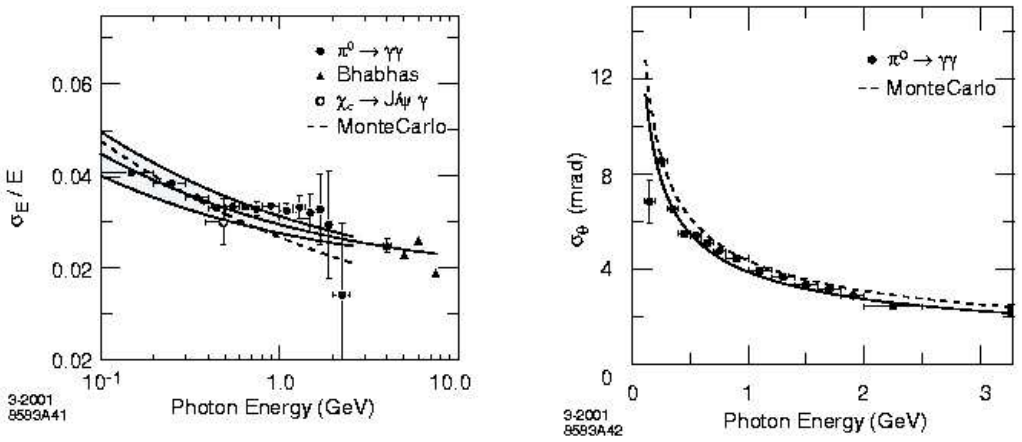

Figure 3.13: Left: EMC energy resolution versus energy for photons and electrons of various sources. Right: Angular resolution of the EMC for photons from symmetric π^0s.

The energy resolution shown in Figure 3.13 can be described by the formula:

$$\frac{\sigma_E}{E} = \frac{a}{\sqrt[4]{E}} + b. \tag{3.3}$$

The first term is energy dependent, reflecting changes in photon statistics and electronic noise. b is dominant at high (>1 GeV) energies and is due to calibration, leakage and absorption. At low energy, resolution is obtained from the radioactive fluorinert source and at 6.31 MeV is measured to be $\frac{\sigma_e}{E} = (5.0 \pm 0.8)\%$. At energy ranges of about 500 MeV the decay $\chi_{c1} \to J/\psi\,\gamma$ is used for calibration, and above 1 GeV $\mu^+\mu^-\gamma$ decays are used. Below 2 GeV, $\pi^0 \to \gamma\gamma$ calibration is also used, as shown in Figure 3.14. The highest energy resolution is measured at 7.5 GeV from Bhabha scattering, giving $\frac{\sigma_e}{E} = 1.90 \pm 0.07\%$. The total energy resolution is expressed by the formula:

$$\frac{\sigma_e}{E} = \frac{(2.32 \pm 0.30)\%}{\sqrt[4]{E}} + (1.85 \pm 0.12)\% \tag{3.4}$$

Angular resolution is determined by the crystal size and distance from the interaction point and can be described empirically in the form:

$$\sigma_\theta = \sigma_\phi = \frac{c}{\sqrt{E}} \tag{3.5}$$

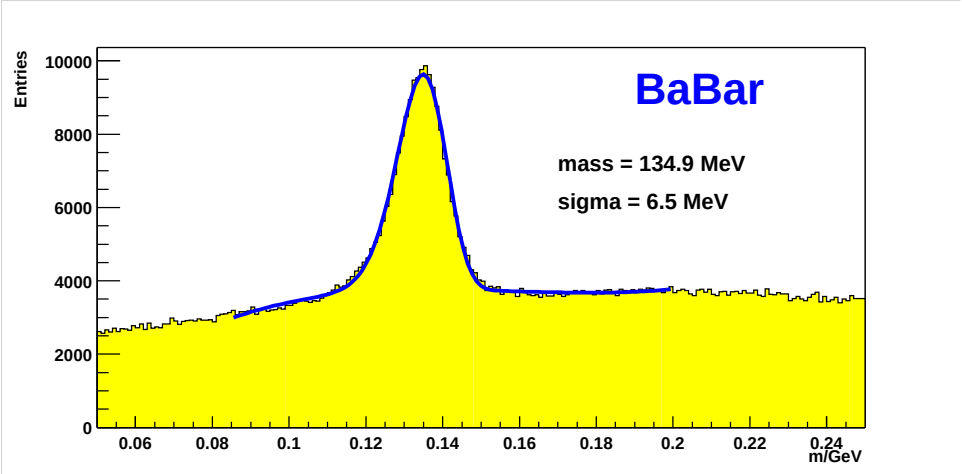

Figure 3.14: EMC π^0 mass resolution - invariant mass of two photons in hadronic events with the energy of both photons above 30 MeV and π^0 energy above 300 MeV. The solid line is a fit, giving a sigma of 6.5 MeV.

where E is measured in GeV and c is a constant.. The measurement of angular resolution is based on Bhabha and $\pi^0 \rightarrow \gamma\gamma$ events (see Figure 3.13, where the solid curve is a fit indicating $\sigma_\theta = \frac{3.87\ (\text{mrad})}{\sqrt{E\ (GeV)}}$).

3.2.5 The superconducting magnet

In order to measure the momenta of charged tracks, a magnetic field of 1.5T is applied inside the *BABAR* tracking volume. Owing to the complicated geometry at the interaction point (as the HER and LER beams must be separated after collision), the B-field does not have the same axis as the PEP-II beam axis.

Hardware

The inner radius of the solenoid is 1.4 m and the outer radius 1.73 m. It is made of 20 Rutherford NbTi/Cu wires in an aluminium matrix and cooled to 4.5K by liquid helium. The current density is higher at the ends of the solenoid than at the centre in order to maintain field uniformity. To achieve this two winding types are used: thinner at the ends (3.6 mm) with 210 turns and thicker in the centre (6.2 mm) with 315 turns. It is surrounded by a cryostat, consisting of a

tube vacuum vessel and thermal shielding at 80K.

3.2.6 The Instrumented Flux Return (IFR)

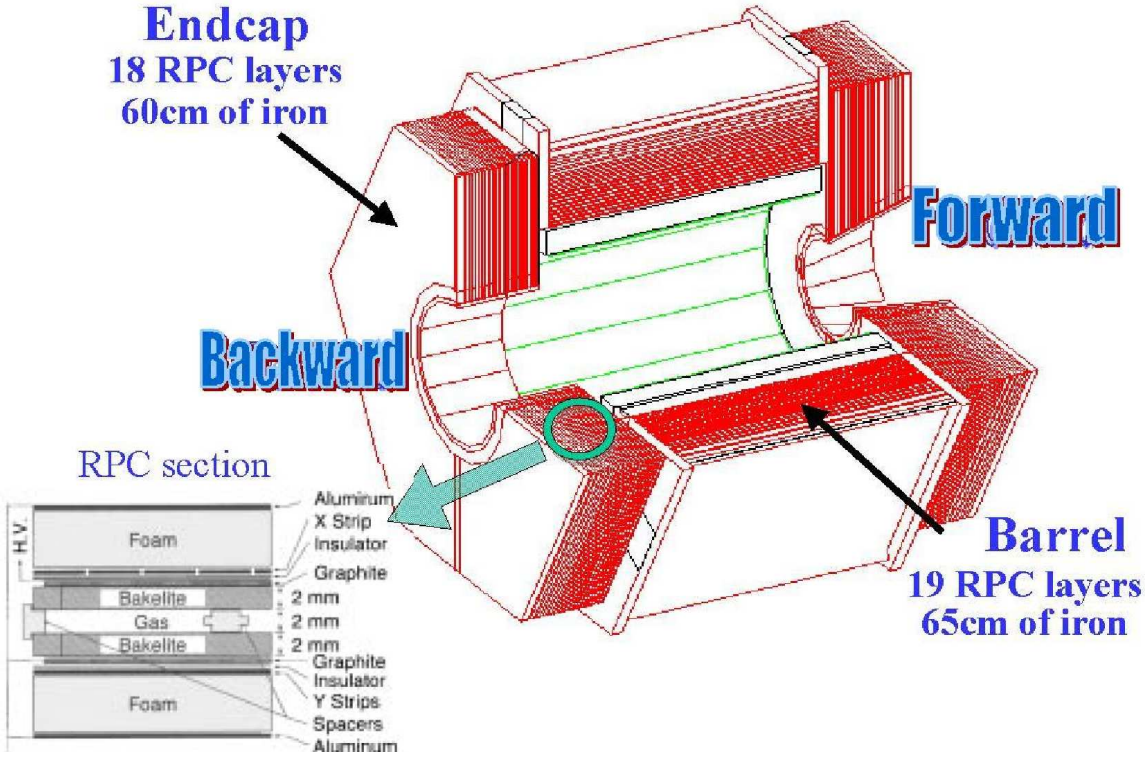

Figure 3.15: Schematic diagram of the IFR.

Muon detection is important for tagging semi-leptonic B decays. The IFR is designed to detect muons with energy greater than 500 MeV, giving a B tagging efficiency of 9%. The IFR also detects neutral hadrons such as K_L^0.

The IFR is also the external flux path for the solenoid B-field, as well as the seismic and gravitational load path for the barrel detector.

Hardware

The IFR is constructed in 3 segments - the barrel and two end-caps. It is 3.75 m long with an inner radius of 1.78 m and outer radius 3.01 m. It is constructed

from sheets of iron with increasing thickness, from 2 cm in the innermost barrel layer to 5 cm in the outermost and from 5 cm to 10 cm in the end-caps. The iron layers contain 30 mm gaps which are filled with resistive plate capacitors (RPCs). These detect streamers from ionising particles using external capacitive readout strips.

Performance

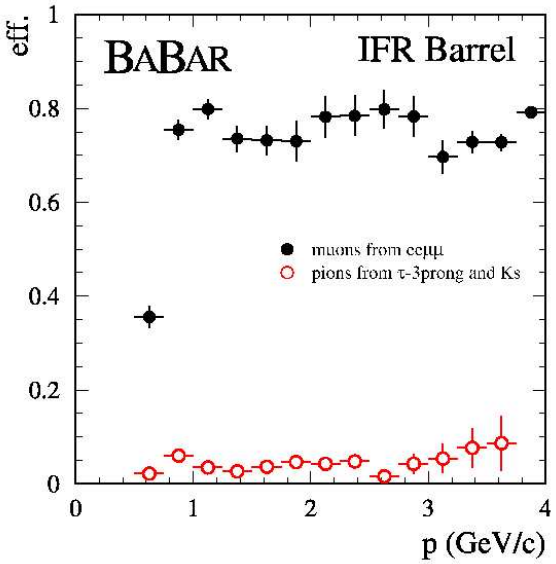

Figure 3.16: μ identification efficiency vs π contamination.

Muons are identified by comparing the number of traversed interaction lengths in the entire detector with what is expected for a muon of a particular momentum. Additional μ/π discrimination is provided by the projected intersections of a track with the RPC planes - hadronic interactions produced by a pion are expected to give a larger number of strip clusters than those produced by a muon. Cluster shape distribution functions are also used. The performance of muon selection has been tested on kinematically identified muons from $\mu^+\mu^- ee$ and $\mu^+\mu^-\gamma$ decays and using pions from 3-prong τ decays and $K^0_L \to \pi^+\pi^-$ decays (see Figure 3.16).

Chapter 4

Photon quality in the EMC

4.1 Introduction

The *BABAR* Electromagnetic Calorimeter (EMC) has strict performance criteria. It must measure electromagnetic showers with excellent energy and angular resolution over a large energy range - this allows the detection of photons from π^0 and η decays as well as from electromagnetic and radiative processes. It is also used for electron identification and as a complement to the IFR for μ and K_L^0 detection. Both hardware and software contribute to achieving the best possible reconstruction efficiencies. In this chapter, the accurate identification of photons will be discussed and the design of a new scheme of photon quality measurement described.

4.2 Photon quality

Photons and electrons passing through the *BABAR* detector produce an electromagnetic shower in the calorimeter, which typically spreads over many adjoining crystals forming a cluster of energy deposits. Pattern recognition software has been developed to distinguish single clusters ('bumps'), with only one energy maximum from merged clusters with more than one maximum. Clusters must contain at least one seed crystal with an energy of above 10 MeV. Surrounding crystals are considered part of the cluster if their energy exceeds a threshold of

1 MeV, or if they are contiguous neighbours of a crystal with at least a 3 MeV signal.

A bump is assigned to a charged particle if a track can be associated with it. Each track is projected onto the calorimeter and the distance between the point where the track hits the calorimeter and the bump centroid is calculated. If this is consistent with the angle and momentum of the track the bump is associated with the charged particle, otherwise it is assumed to originate from a neutral particle.

This process is not always accurate, and the main sources of photon mis-identification are as follows:

- Badly reconstructed charged particles: the energy deposit is not matched to the track through the rest of the detector.
- Split-offs: the shower created by the EMC hit contains other particles, e.g. neutrons, which fly off and are identified as photons unassociated with the track or particle that spawned them.

The *BABAR* reconstruction software calculates a number of variables which can be used by analysts to differentiate between real and fake photons. These variables are typically used alone, but they can be combined to form a much more powerful discriminant.

4.3 Monte Carlo studies

True photon clusters tend to have a compact cluster shape, while split-off clusters tend to have lower energy, an extended cluster shape and are often found close to a track-associated cluster.

Using generic $b\bar{b}$ Monte Carlo (MC) simulation events, the various cluster shape quantities available in EMC data were compared for signal and background. For each event, all reconstructed EMC candidate neutral bumps were examined

and separated into 'signal' (bumps identified as true photons in the simulation) and 'background' (everything else - mainly identified as electrons and pions).

The variables examined in this study include 6 measures of cluster shape:

- The ratio of energy deposited in the central crystal of a cluster, to the energy deposited in the surrounding nine ('s1s9' - see Figure 4.1).

- The ratio of energy deposited in the surrounding nine crystals,p to the surrounding twenty five ('s9s25' - see Figure 4.2).

- The second moment in $\theta - \phi$ (see Figure 4.3):

$$\text{second moment} = \sum_{crystal\ i} \frac{E_i.((\theta_i - \theta_0)^2 + (\phi_i - \phi_0)^2)}{\sum_i E_i} \tag{4.1}$$

  where $\theta_i(\phi_i)$ and $\theta_0(\phi_0)$ are the centroid position of the i^{th} crystal and of the bump respectively.

- The lateral moment of the shower shape ('LAT' - see Figure 4.4):

$$LAT = \frac{\sum_{i=3}^{N} E_i r_i^2}{\sum_{i=3}^{N} E_i r_i^2 + E_1 r_0^2 + E_2 r_0^2} \tag{4.2}$$

  where E_i is the energy deposited in the ith crystal such that $E_1 > E_2 > ... > E_N$, r_i is the radial coordinate in the plane perpendicular to the line pointing from the interaction point to the shower centre, and r_0 is the average distance between two crystals, approximately 5cm for the *BABAR* calorimeter. The sum starting from i=3 omits the two crystals containing the highest amounts of energy.

- The absolute value of the complex Zernike moment (2,0) (see Figure 4.5):

$$Zernike\ moment = \sum_{r_i \le R_0}^{n} \frac{E_i}{E}.f_{nm}(\frac{r_i}{R_0})e^{-im\phi_i}, \tag{4.3}$$

  where $R_0 = 15\,\text{cm}$ and

$$f_{nm}(\rho_i \equiv \frac{r_i}{R_0}) = \sum_{s=o}^{(n-m)/2} \frac{(-1)^s (n-s)! \rho^{n-2s}}{s!(\frac{(n+m)}{2} - s)!(\frac{(n-m)}{2} - s)!} \tag{4.4}$$

  with $m, n \ge 0$ integers, $m \le n$ and $n - m$ even.

- The absolute value of the complex Zernike moment (4,2) (see Figure 4.6).

As well as these variables, the total energy deposited in the calorimeter (see Figure 4.8) and the distance of closest approach ('doca') between the neutral cluster of interest and the nearest charged track cluster (where 'nearest' means smallest doca - see Figure 4.7) were also studied as potentially useful discriminants.

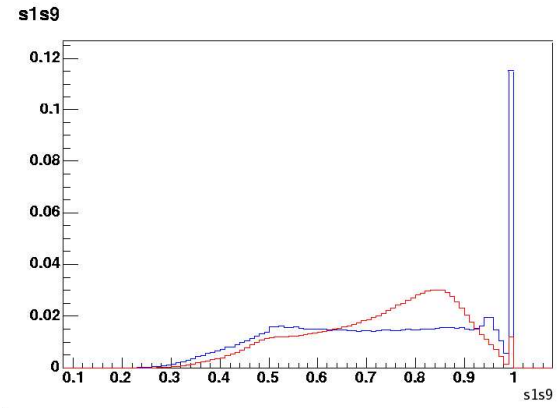

Figure 4.1: s1s9 for generic $b\bar{b}$ MC. Red: true photons, blue: background.

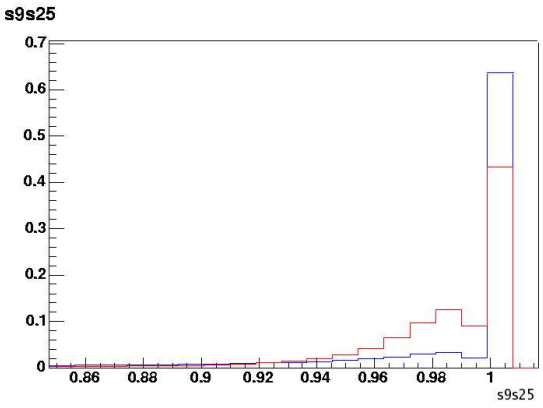

Figure 4.2: s9s25 for generic $b\bar{b}$ MC. Red: true photons, blue: background.

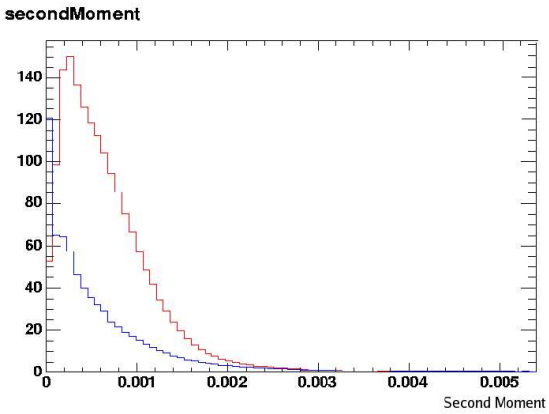

Figure 4.3: Second moment for generic $b\bar{b}$ MC. Red: true photons, blue: background.

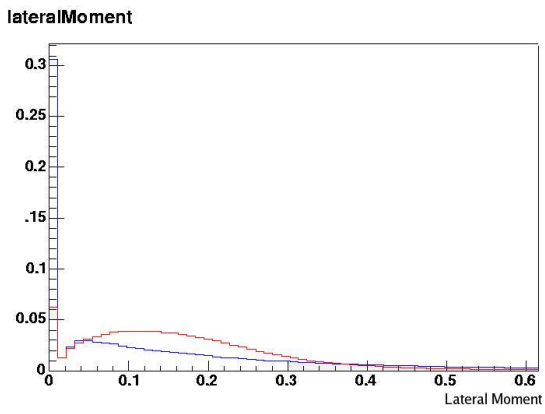

Figure 4.4: Lateral moment for generic $b\bar{b}$ MC. Red: true photons, blue: background.

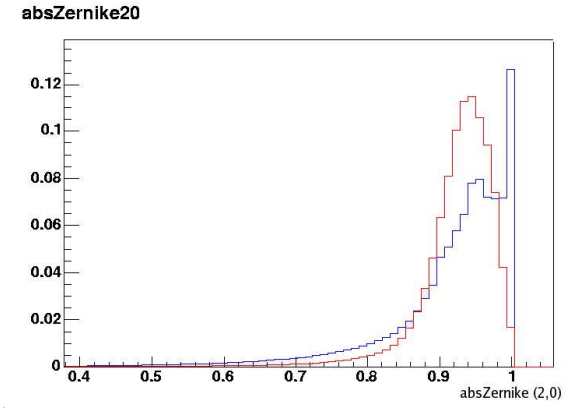

Figure 4.5: Absolute Zernike moment (2,0) for generic $b\bar{b}$ MC. Red: true photons, blue: background.

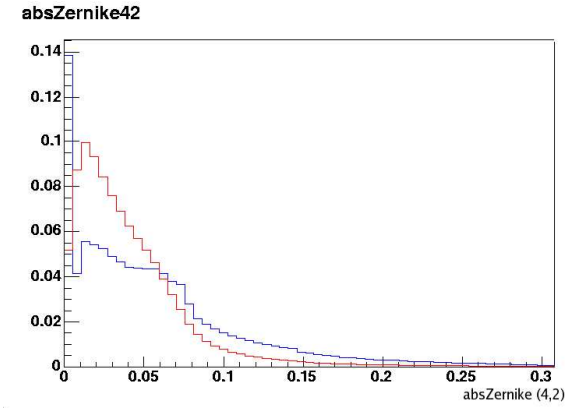

Figure 4.6: Absolute Zernike moment (4,2) for generic $b\bar{b}$ MC. Red: true photons, blue: background.

It was found that making direct cuts on all individual variables, although effective, did not significantly improve background rejection compared to cutting on one variable alone. Combining cluster shape variables into an algorithm designed to discriminate between real and fake photons is a better option. A Fisher discriminant was studied but found to be unsuitable as it does not account for the strong correlations between variables. A Neural Network (NN) was determined to be the best method, as it allows for correlations between variables and gives the best separation between signal and background.

The energy deposited in the calorimeter for each EMC cluster is a very powerful discriminator, but by using it as an input to the Neural Network a bias would be introduced in favour of higher-energy particles, which is undesirable in most analyses. Therefore the MC sample was split into different energy bins and separate NNs trained on each bin. This allows the retention of some of the discriminating power of the variable while avoiding any artificial energy cut. Finer binning was used at low energy:

- 50 MeV bins up to 0.5 GeV
- 100 MeV bins 0.5 - 1 GeV

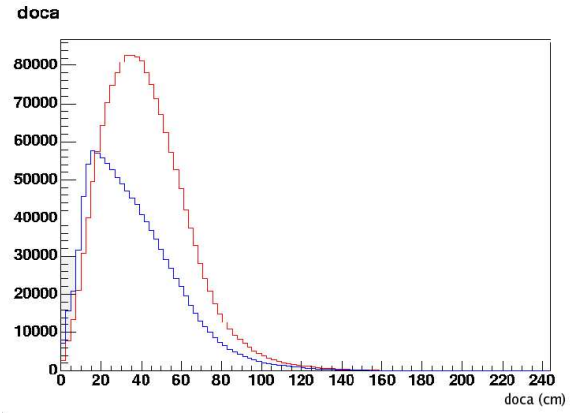

Figure 4.7: Distance of closest approach for generic $b\bar{b}$ MC. Red: true photons, blue: background.

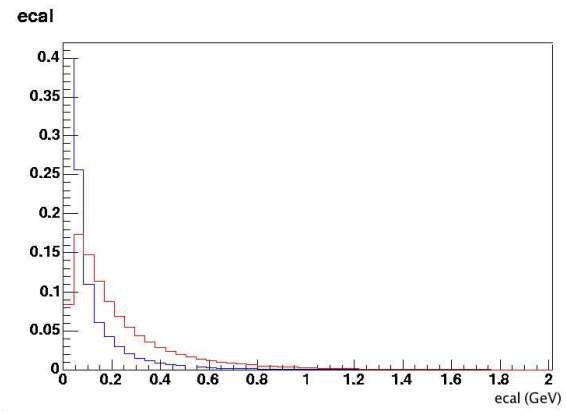

Figure 4.8: Energy deposited in calorimeter for generic $b\bar{b}$ MC. Red: true photons, blue: background.

- 200 MeV bins 1 - 2 GeV
- 500 MeV bins 2 - 3.5 GeV
- one bin 3.5 GeV and above

giving a total of 23 bins in cluster energy.

4.4 Neural Networks

Most Neural Networks are multilayer perceptrons (MLP), the model used in this analysis. The multilayer perceptron is a Neural Network that can be trained to transform input data into a desired response, widely used for pattern recognition, data analysis and classification.

The building blocks of an MLP are simple neurons called perceptrons. A perceptron calculates a single output from multiple inputs by forming a linear combination, according to it's input weights.

A multilayer perceptron consists of a set of source neurons (nodes) as the input layer, one or more hidden layers of computation nodes and an output layer. The network learns using the back-propagation algorithm which consists of two steps. In the 'forward' pass, the predicted outputs corresponding to the given

inputs are calculated. The first layer - the input layer - simply normalises the input parameters and passes them on to the first hidden layer. The input to node j in the first hidden layer is given by:

$$input_j = \Sigma_i w_{ji} output_i \tag{4.5}$$

where $output_i$ is the output from input node i and w_{ji} is the weight connecting input node i to node j. In the first forward pass small random weights are assigned. The output of node j is then given by the activation function of this input:

$$output_j = f(input_j) \tag{4.6}$$

which is sent on to all nodes in the following layer. The activation function is generally chosen to be the logistic sigmoid

$$f(x) = \frac{1}{1 + e^{-x}}, \tag{4.7}$$

used because it is close to linear near the origin and saturates quickly when moving away from the origin, thus acting as a thresholding device. In the 'backward' pass, partial derivatives of the error function with respect to the input parameters are propagated back through the network. The weights for each neuron can then be re-calculated for the chosen optimisation algorithm. This process is repeated until weights have converged. It has been shown that MLPs can approximate virtually any function to any desired accuracy, given enough hidden layers and enough data [31].

This study used the ROOT TMultiLayerPerceptron function [30]. Only one hidden layer containing 5 neurons was needed to give good discrimination between signal and background. One output node provided the likelihood (from 0 - 1, with 1 being most photon-like) of the sample EMC cluster being created by a photon. The optimisation algorithm used was the default - stochastic minimisation. In this algorithm, the weights are updated after each iteration according to the formula:

$$w_{ij}(t+1) = w_{ij}(t) + \Delta w_{ij}(t) \tag{4.8}$$

with $\Delta w_{ij}(t) = -\eta(de_p/dw_{ij} + \delta) + \epsilon\Delta w_{ij}(t-1)$. By default, $\eta = 0.1$, $\delta = 0$ and $\epsilon = 0$. 50 training iterations were necessary for best convergence. The MC sample was split into two equal, random sets - one used to train the network and the other to evaluate it.

4.5 Results

Example NN output plots for low (Figure 4.9), mid (Figure 4.10) and high (Figure 4.11) energy ranges are given here.

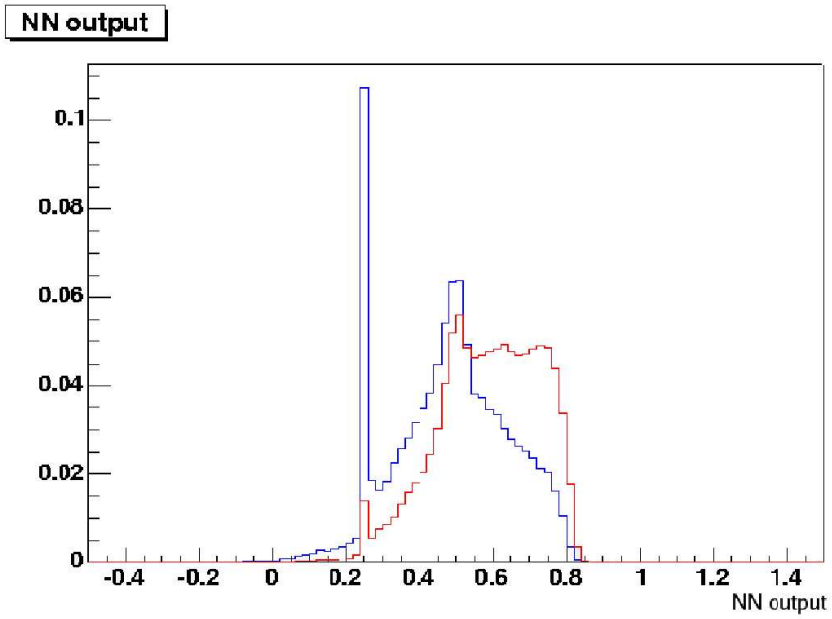

Figure 4.9: Neural Net output in the bin 0.05 - 0.1 GeV. Red: signal, blue: background.

There is clear discrimination between signal photons (red) and background non-photons (blue). Discrimination is much improved at higher energies, as expected.

The spike in the low energy plot has been examined in more detail. All EMC candidates that contribute to the spike have 'extreme' cluster shape variables - LAT=0, s1s9=1 etc. They are the result of EMC single-crystal hits or electronic noise.

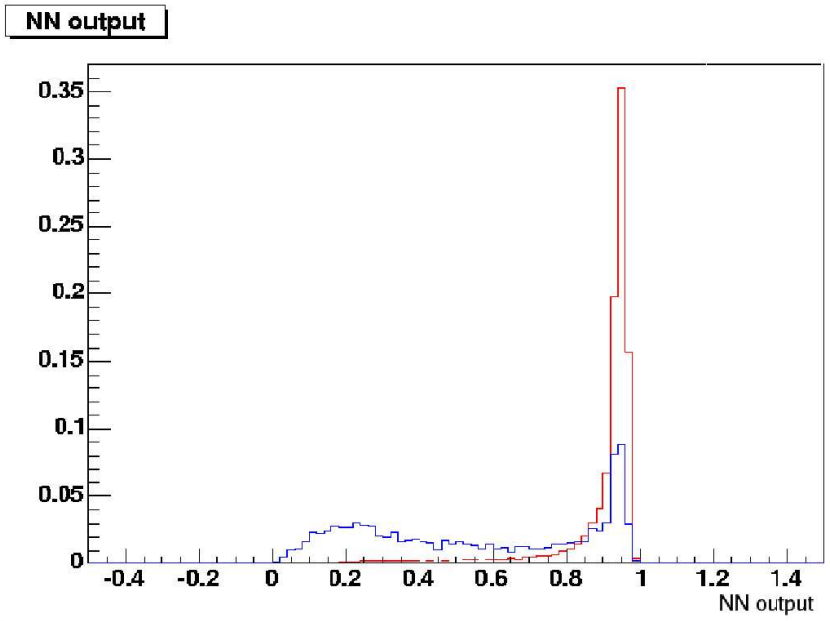

Figure 4.10: Neural Net output in the bin 0.4 - 0.5 GeV. Red: signal, blue: background.

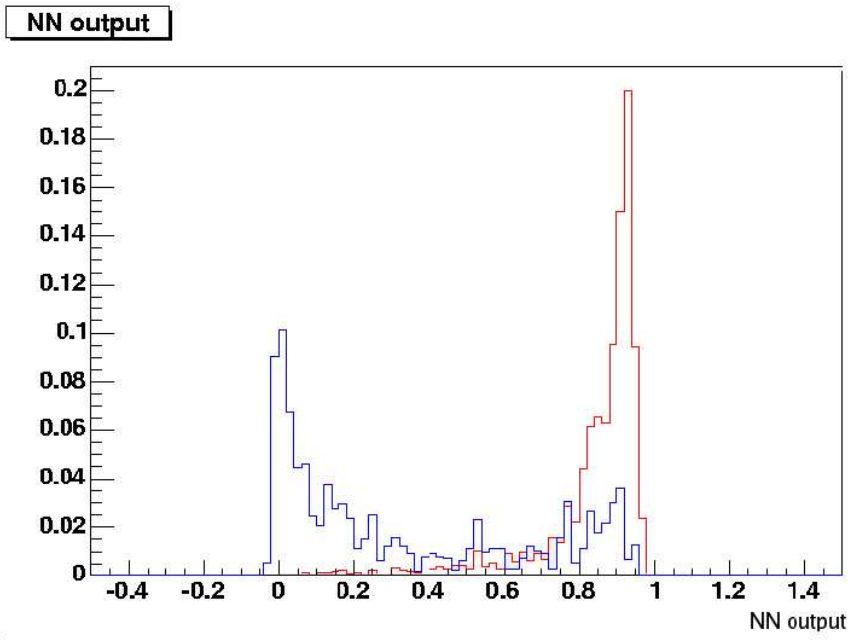

Figure 4.11: Neural Net output in the bin 1.8 - 2.0 GeV. Red: signal, blue: background.

4.6 Photon quality measure

The NN output shapes vary from energy bin to bin, so using the raw NN output value as the basis of a global photon quality measure is inappropriate. In the different types of MC samples, the background NN output shapes vary considerably but the signal distributions remain very similar. The proportion of signal remaining, if a cut were made at that NN output value, is a more appropriate measure as it is independent of the distribution range of the NN output. Figure 4.12 demonstrates how this would function for an example NN output. The total output distribution is shown in black, with the signal component in red and background in blue. The quality measure returned to the user is shown in green. For example, if an EMC candidate had a NN output value of 0.1 the corresponding 'photon quality' value would be 0.9, because 90% of the signal would remain of a cut were made at that point.

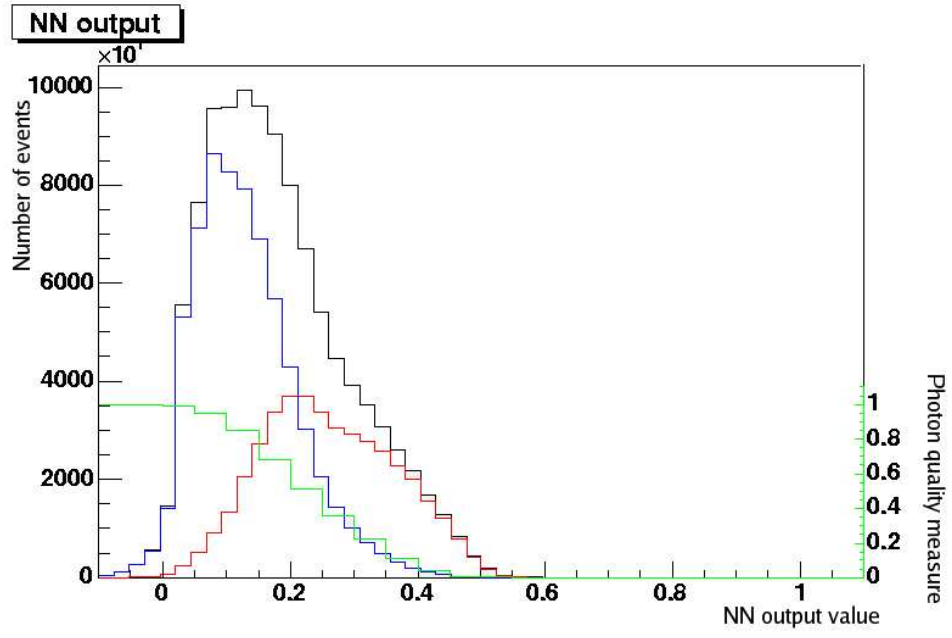

Figure 4.12: Photon quality measure. Black: total signal distribution, red: signal component, blue: background component, green: photon quality measure (right hand scale).

The distribution of photon quality values for a generic $b\bar{b}$ MC sample is shown

in Figure 4.13, with signal in red and background in black. It is clear that true photons tend to have low values and non-photons (split-offs, mis-identified charged particles) tend to have values near 1. The user can make a cut on this distribution according to their analysis requirements.

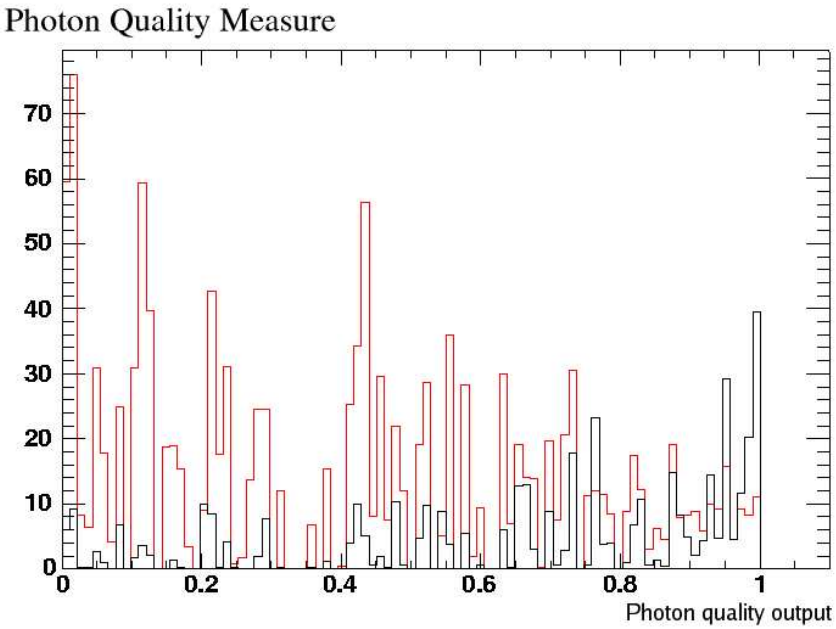

Figure 4.13: NN photon quality output. Signal in red, background in black.

To investigate the improvement over traditional photon quality measurements, the performance of the NN measure was compared to a simple cut on the lateral moment of the EMC cluster, a quantity which is often used in *BABAR* analysis. The plots in Figure 4.14 - Figure 4.16 show the efficiency (fraction of remaining signal) vs purity (1 - fraction of remaining background) for increasing cut value. An additional cut was applied to the LAT plots so that LAT$\neq$0, which removes EMC signal-crystal clusters caused by electronic noise. Figure 4.14 shows the improvement over the whole energy range. The efficiency is improved most in the low energy range (Figure 4.15), while in the high energy range (Figure 4.16) both the LAT cut and the NN cut are equally impressive.

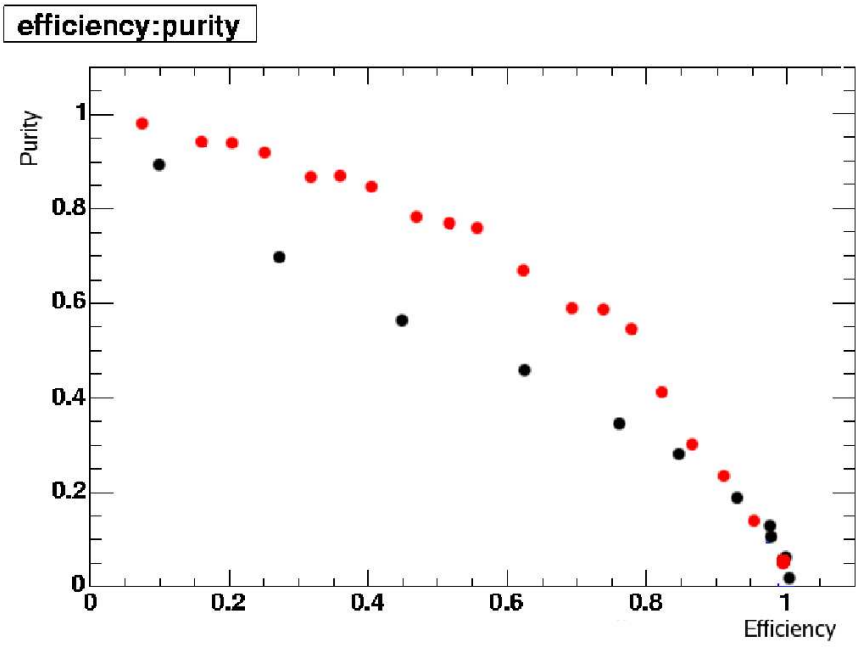

Figure 4.14: Comparison of effectiveness of NN photon measure compared to LAT cut alone. Red: NN, black: LAT cut with LAT$\neq$0.

4.7 Summary

Photon identification is a key element of the *BABAR* EMC operation, and a vital part of any analysis that relies on accurate photon energy measurements. It has been shown that a multi-variate technique is a powerful method of distinguishing true photons from fakes, performing better (especially in the low-energy region) than than using direct cuts on individual cluster shape variables.

A Neural Net has been chosen as the ideal discriminator, as it can account for correlations between variables and gives good separation of true and fake photons in simulation Monte Carlo events. This measure has now been implemented in the *BABAR* analysis framework as an alternative photon quality measure.

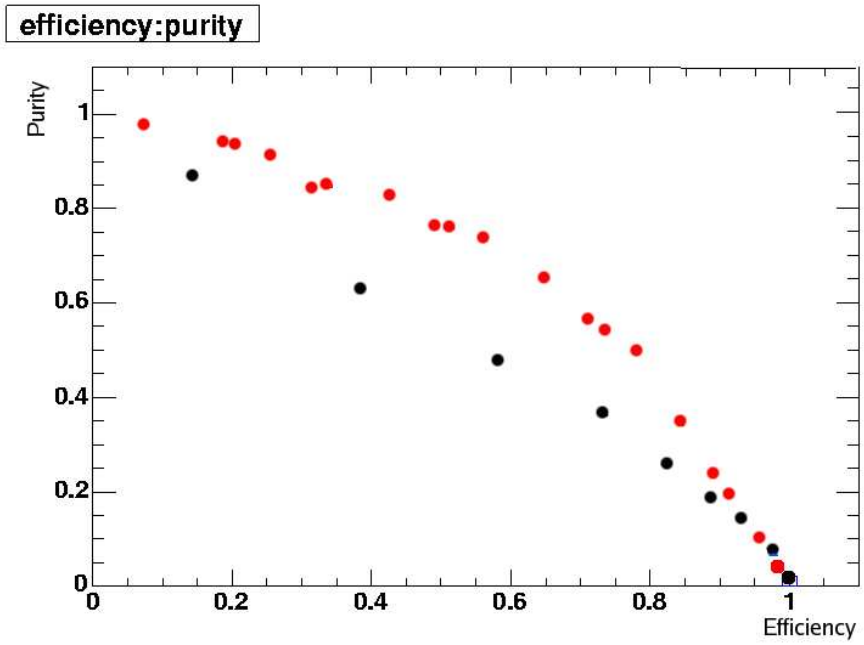

Figure 4.15: Comparison of effectiveness of NN photon measure compared to LAT cut alone in energy region <200 MeV. Red: NN, black: LAT cut with LAT≠0.

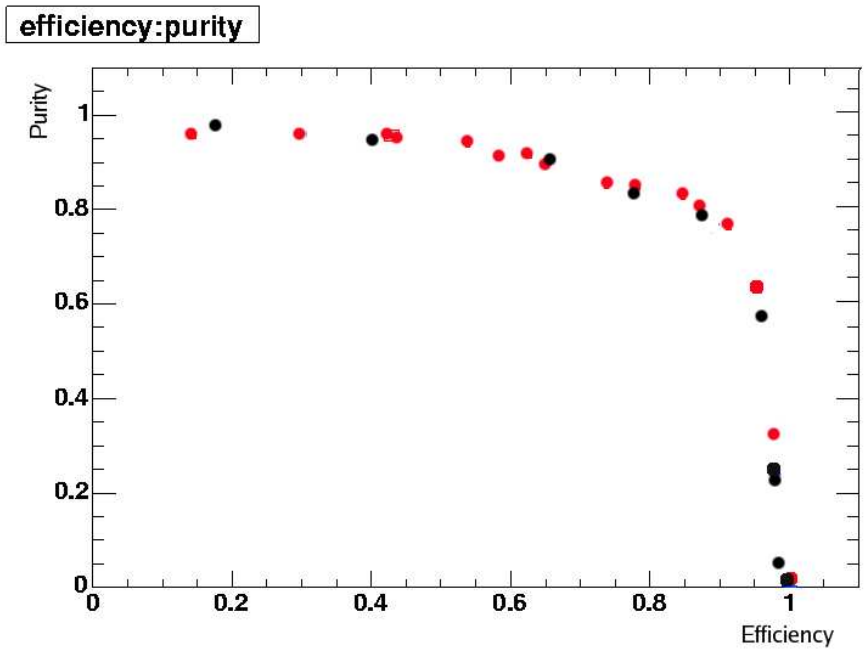

Figure 4.16: Comparison of effectiveness of NN photon measure compared to LAT cut alone in energy region >1 GeV. Red: NN, black: LAT cut with LAT≠0.

Chapter 5

Design of the $b \to d\gamma$ analysis

5.1 Introduction

There are several stages of data processing in the search for the $b \to d\gamma$ transition, from basic event reconstruction and background reduction to fitting and signal extraction. This chapter describes the selection of interesting candidate decays from the raw *BABAR* dataset and the cuts applied to reduce backgrounds.

5.2 Outline of analysis strategy

In the *BABAR* experimental framework, an analysis proceeds in several stages. In the first level of data processing, the large dataset is skimmed by applying a loose set of cuts to select events of interest. This analysis skimmed the data twice, once with loose cuts to pick out radiative penguin-like decays, using the fact that $b \to d\gamma$ (and $b \to s\gamma$) decays are characterised by a high energy photon in the event. The reduced dataset was then skimmed again with tighter selection requirements to reduce the amount of generic B background to be processed in the following stages.

In the next stage, more detailed reconstruction was carried out using the reduced dataset. Various useful properties of the event and the particles were calculated and stored, to be used later on in the analysis. Loose cuts were also applied. The reconstruction of the inclusive $b \to d\gamma$ decay was approximated at

iType	$b \to d\gamma$ decay mode	$b \to s\gamma$ decay mode
1	$B^0 \to \pi^+\pi^-\gamma$	$B^0 \to K^+\pi^-\gamma$
2	$B^+ \to \pi^+\pi^0\gamma$	$B^+ \to K^+\pi^0\gamma$
3	$B^+ \to \pi^+\pi^-\pi^+\gamma$	$B^+ \to K^+\pi^+\pi^-\gamma$
4	$B^0 \to \pi^+\pi^-\pi^0\gamma$	$B^0 \to K^+\pi^-\pi^0\gamma$
5	$B^0 \to \pi^+\pi^-\pi^+\pi^-\gamma$	$B^0 \to K^+\pi^-\pi^+\pi^-\gamma$
6	$B^+ \to \pi^+\pi^-\pi^+\pi^0\gamma$	$B^+ \to K^+\pi^-\pi^+\pi^0\gamma$
7	$B^+ \to \pi^+\eta\gamma$	$B^+ \to K^+\eta\gamma$

Table 5.1: Table of decay iTypes.

this stage by a semi-inclusive reconstruction (as described in Section 2.6.1). The seven different decay channels or 'iTypes' listed in Table 5.1 were combined to create a sum-of-exclusive-modes approximation of the inclusive $b \to d\gamma$.

Once the interesting events were reconstructed and their properties calculated, more detailed selections could be made. From this point in the analysis, all decay channels were treated equally with quality cuts and background suppression techniques optimised for the dataset as a whole, not for individual iTypes. At this stage, a large number of background decays remained which were removed as follows:

- Combinatoric backgrounds were reduced with candidate quality cuts (described in Section 5.5).
- Continuum backgrounds were suppressed using a combination of event shape variables (described in Section 5.7).
- Background from other B decays ('generic B' or '$b\bar{b}$' backgrounds), including 'cross-feed' ('X-feed') from mis-reconstructed signal decays, were reduced with a π^0/η veto and accurate particle identification (described in Section 5.7).

Once backgrounds had been reduced by an optimal amount, the signal was extracted using a multi-dimensional likelihood fit described in detail in Chapter 6.

All cuts and selections described in this chapter were optimised using *BABAR* Monte Carlo simulations of signal and background decays. They were then applied to data with no further adjustments or improvements, to ensure the analysis was not constructed in such a way as to be biased in favour of extracting an expected signal

5.2.1 Kinematic variables

Two kinematic variables are widely used to characterise signal decays in *BABAR* analysis: ΔE^*, the energy difference between the beam and the reconstructed B-meson and $m_{\rm ES}$, the beam-constrained mass.

In the $\Upsilon(4S)$ rest frame (the c.m. frame, denoted by *), ΔE^* is defined as:

$$\Delta E^* = E^*_\gamma + E^*_X - E^*_{beam} \tag{5.1}$$

Here, $E^*_{beam} = \frac{1}{2}\sqrt{s}$, where $\sqrt{s}$ is the total energy in the c.m. frame of the e^+e^- system and E^*_γ (E^*_X) is the energy of the primary photon (hadronic decay product) in the c.m. frame. The distribution of ΔE^* for signal events peaks around zero, with a resolution function due to the energy response of the detector. The position of the peak depends on the particle identification, since a wrong mass assignment results in a shift in ΔE^*. Most background decays have a non-peaking distribution in ΔE^*whereas some $b\bar{b}$ background decays, for example badly reconstructed $b \to d\pi^0$ or $b \to d\eta$, come from true B meson decays. These have a similar ΔE^* distribution as the true signal decays, but as they are mis-reconstructed the energy of the decays will not be correctly calculated and the central peak is shifted from zero.

The ΔE^* distribution for data in the low hadronic mass region for $b \to s\gamma$ is shown in Figure 5.1. This is the hadronic mass region 0.6 GeV/c^2 - 1.0 GeV/c^2, which contains the $B \to K^*\gamma$ resonance and is used as a control sample (as described in Section.7.2).

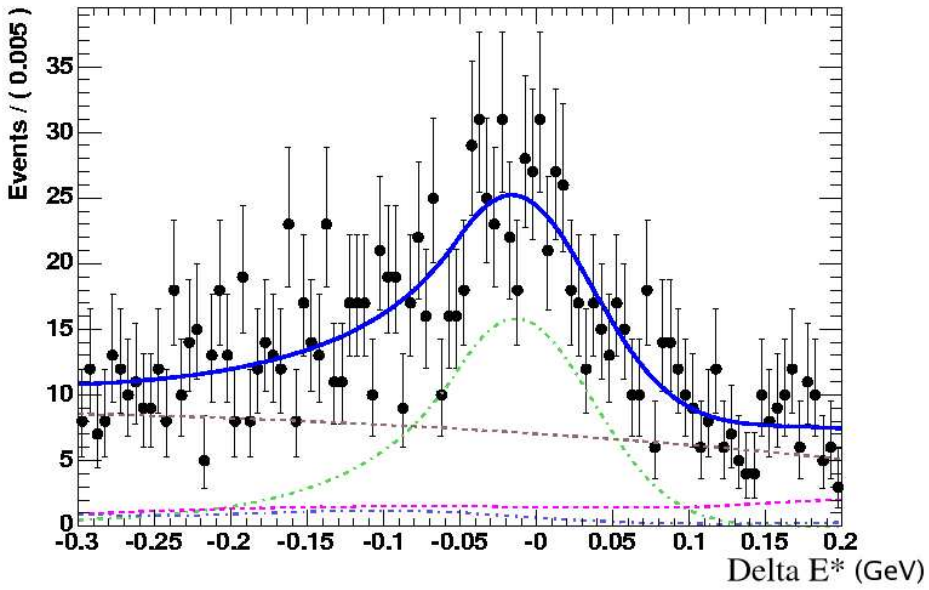

Figure 5.1: ΔE^* for data in the K^* control sample. The fit for the signal is shown in green, continuum background in brown, $b \to s\gamma$ cross-feed in pink and generic B background in blue.

The beam-constrained mass $m_{\rm ES}$ is defined as:

$$m_{\rm ES} = \sqrt{E^{*2}_{beam} - p^{*2}_B} \tag{5.2}$$

where p^{*2}_B is the B momentum in the c.m. frame. In calculating p^{*2}_B the photon momentum is scaled so that $E^*_\gamma + E^*_X - E^*_{beam} = 0$. The rescaling of photon momentum reduces the asymmetry in the signal distribution, which comes from energy leakage in the calorimeter. This value of $m_{\rm ES}$ is largely independent of the calorimetric energy measurement of the photon and the resolution of $m_{\rm ES}$ is dominated by the beam energy spread. The narrow distribution of $m_{\rm ES}$ for true signal events makes it an ideal discriminator, peaking at the B mass of $5.280\,{\rm GeV}/c^2$. Background decays (apart from the mis-reconstructed $b\bar{b}$ decays described above) have no peaking structure, but fall off at the kinematic limit of $5.290\,{\rm GeV}/c^2$.

The $m_{\rm ES}$ distribution for the K^* control data is shown in Figure 5.2.

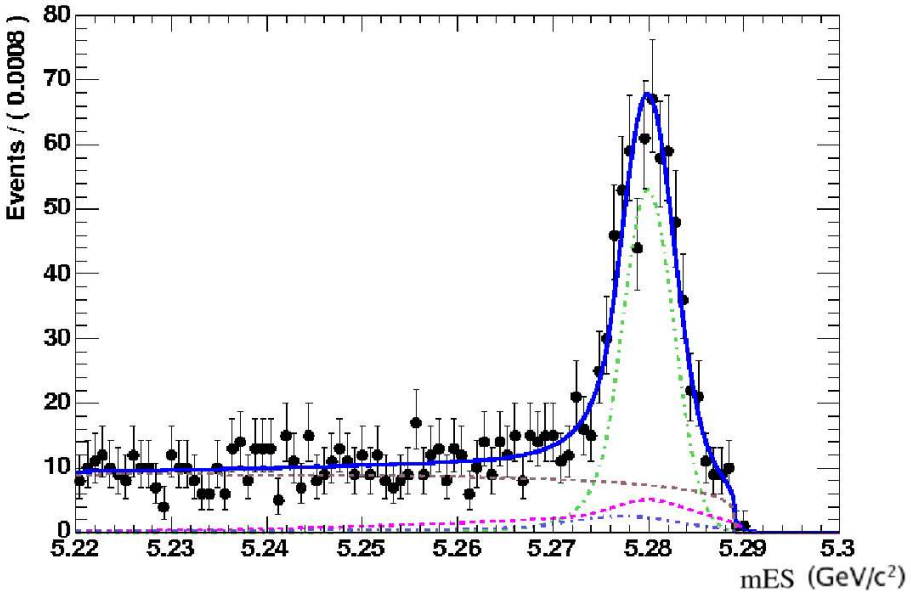

Figure 5.2: ΔE^* for data in the K^* control sample. Signal is shown in green, continuum background in brown, $b \to s\gamma$ cross-feed in pink and generic B background in blue.

5.3 Skimming

The *BABAR* collaboration has a large amount of Monte Carlo (MC) simulated events, along with over 300 million real $B\bar{B}$ events at the $\Upsilon(4S)$ resonance. Full reconstruction is very computer-intensive, so in order to reduce the amount of data to be processed the MC and data samples are skimmed. The skimming process performs very basic reconstruction, where a few useful variables are calculated and used to differentiate between possible signal and background events.

This analysis took advantage of the skimming procedure to reduce both MC and data sets to manageable amounts. A new skim (called BToXdGamma) was constructed, taking as input the BtoXGamma skim developed for the *BABAR* Radiative Penguin analysis group.

The BtoXGamma skim looks specifically for a high-energy photon and requires that the event satisfies the following criteria:

- $1.15\,\text{GeV} < E^*_{\gamma,max} < 3.5$ GeV

  to pick out the high-energy photons, where $E^*_{\gamma,max}$ is the largest c.m. energy of any neutral EMC energy deposit.

- $N_{GTL} \geq 2$

  where N_{GTL} is the number of charged tracks in the event that satisfy the Good Tracks Loose criteria:

  - a successful helical fit.
  - a minimum transverse momentum of $0.1\,\text{GeV}/c$.
  - a maximum total momentum of $10\,\text{GeV}/c$.
  - a minimum number of 12 DCH hits.
  - a maximum DOCA (where DOCA here is the distance of closest approach of the particle in question to the interaction point), of 1.5 cm in x/y plane.
  - a range of DOCA along the beam z axis -10 cm < DOCA(z) < 10 cm.

- $R_2 < 0.9$

  R_2 is the ratio of the second Fox-Wolfram (FW) moment to the zeroth FW moment in the c.m. frame of the event. The Fox-Wolfram moments are the rotationally invariant moments of the angular energy distribution. They measure the 'jettiness' of the event. Spherically symmetric (signal) events have a moment closer to zero, while axial (continuum) events have a moment closer to one.

  A cut on this variable also reduces the number of radiative Bhabha scattering events ($e^+e^- \to e^+e^-\gamma$), another problematic background.

The BtoXGamma skim is a standard *BABAR* skim, available to all users. However, large amounts of unwanted backgrounds still pass this skim and a tighter set

of selections specific to this analysis are required to avoid processing unnecessary amounts of data.

The BToXdGamma skim takes all events that pass the BtoXGamma selections and imposes additional cuts on the reconstructed B mesons and their decay products as follows:

- π^0s reconstructed from two daughter photons, with some additional criteria:
  - π^0 energy in lab frame over 0.2 GeV.
  - Daughter photons possess energy in lab frame over 0.03 GeV.
  - Daughter photons have lateral moment values between 0.0 and 0.8 (see Section 4.3 for a description of the lateral moment).
  - π^0 mass between 0.115 and 0.150 GeV/c^2.
  - Momentum in lab frame greater than 0.3 GeV/c.
- Charged daughters, with the cut:
  - Momentum in lab frame greater than 0.3 GeV/c.
- Hadronic X_d daughters of B meson:
  - Reconstructed X_d mass less than 1.8 GeV/c^2, to remove generic B backgrounds that dominate above this limit.
  - Probability χ^2 of decay daughters originating from same vertex position greater than 0.001.
- B meson candidates:
  - $|cos(\theta_{Thrust})|$ less than 0.8 (see Section 5.7.1 for a full description).
  - $m_{\rm ES}$ between 5.0 and 5.3 GeV/c^2.
  - $|\Delta E^*|$ less than 0.5 GeV.

The efficiencies for these skims for the various MC and data samples are given in Table 5.2.

MC/data type	BtoXGamma skim	BToXdGamma skim
signal MC	73.2%	30.2%
generic B MC	2.5%	0.02%
continuum uds MC	11.4%	0.18%
continuum ccbar MC	7.5%	0.15%
data	6.0%	0.17%

Table 5.2: BtoXGamma and BToXdGamma skim efficiencies.

5.4 Event reconstruction

After the MC and data samples have been reduced by the skim, the remaining events are put through the full event reconstruction. We reconstruct each of the seven hadronic decay modes using very loose selection cuts, taking tracks from the ChargedTracks list which contains all charged candidates with pion mass hypothesis assigned. Neutral particles are taken from the EMC list CalorNeutral, containing single EMC energy deposits, or 'bumps', which are not matched with any track.

The high energy photon candidate is again required to have energy in the region $1.15\,\mathrm{GeV} < \mathrm{E}^*_\gamma < 3.5\,\mathrm{GeV}$. No additional cuts are applied to the charged and neutral daughters, but loose selection cuts are applied to the reconstructed B-meson. Charged tracks are assumed to be pions by default in the *BABAR* software, but in order to include $b \to s\gamma$ decays in this analysis their energy must also be calculated assuming kaon mass. Therefore ΔE^* and m_{ES} are calculated in two ways: (a) assuming all tracks are pions and (b) assuming any one of them is a kaon. We then require that at least one of the kaon/pion hypotheses has ΔE^* in the range -0.5 - 0.5 GeVand m_{ES} greater than 5.2 GeV/c^2.

All other selection and quality cuts are applied after the reconstruction stage.

5.5 Quality cuts

Due to the very loose cuts applied in the event reconstruction, a large number of candidate decays are reconstructed in each event. To remove fake signal events from random combinatorics, a number of quality cuts are applied. These are optimised on signal Monte Carlo simulation by maximising the ratio of the number of signal events that pass the cut, to the square root of the number of signal plus number of background events that pass. Cuts are not optimised on each hadronic decay mode individually, but on all decay modes combined.

5.5.1 High-energy photon quality cuts

The primary high-energy photon candidate is selected from all neutral EMC bumps, unassociated with any charged track. The following selection criteria are applied:

- Only neutral bumps with energy in the c.m. frame between 1.15 GeV and 3.5 GeV are considered.
- The number of EMC crystals included in the EMC energy deposit must be greater than 4.
- The neutral bumps contain no noisy or dead crystals.
- The neutral bumps must be at least 25cm from any other neutral bumps or charged tracks. This cut reduces the backgrounds from split-offs.
- The shape of the EMC energy deposit can be characterised by the second moment. Merged π^0s have an elliptical energy distribution and therefore a large second moment, whereas the signal photon is symmetric around the centroid and tends to have a small second moment. A cut requiring the second moment to be less than 0.002 is applied which removes almost all merged π^0s with virtually no loss in signal efficiency.

- A π^0 (η) veto is applied to the high energy photon. The invariant mass of the candidate photon, when combined with any other neutral bump of energy greater than 30(250) MeV in the laboratory frame, must not lie in the range 105 MeV - 155 MeV (500 MeV - 590 MeV). This veto rejects many of the background photons from π^0/ η decays, a significant part of the generic B background (see Section 5.6.2 for more details).

5.5.2 Charged track quality cuts

Charged particles are selected from the track list ChargedTracks with the additional requirement that the momentum in the laboratory frame be greater than 0.3 GeV/c. This removes a large number of combinatoric backgrounds, where low-energy charged particles are wrongly combined to fake a signal decay.

5.5.3 Neutral pion quality cuts

Neutral pions are reconstructed from two photons. Only π^0s with reconstructed mass between 0.117 GeV/c^2 and 0.145 GeV/c^2 are considered. This mass window is asymmetric around the nominal π^0 mass to reflect the tail of the π^0 mass distribution resulting from energy leakage in the EMC.

5.5.4 X_d and B candidate quality cuts

Tracks and π^0s that pass the above quality cuts are combined to form a hadronic X_d candidate and cuts are applied to this combination. The X_d is then combined with the high energy photon candidate to make a B meson candidate. Additional cuts on ΔE^* and $m_{\rm ES}$ can then be applied.

- In many *BABAR* analyses, precise vertexing of the decay particles is required for physics analysis, for example to determine the displacement of two B-mesons in a time-dependent CP analysis. Various vertexing tools are available within the *BABAR* framework to calculate decay vertices. This analysis uses a simple algorithm to determine if the tracks reconstructed in

the event originate from the same point which would indicate they are all daughters of the same decaying B meson. This can significantly suppress combinatoric backgrounds. The vertexing fit probability χ^2 is required to be greater than 0.02.

- The reconstructed X_d hadronic mass already has an upper bound of 1.8 GeV/$c^2$and here a cut on the lower hadronic mass bound is introduced at 0.6 GeV/c^2. Below this limit very few signal events exist and generic B backgrounds are dominant.

- An additional cut on ΔE^* is applied at this stage, so that -0.3< GeV ΔE^* $< 0.2\,\mathrm{GeV}$.

- Similarly, the loose m_{ES} cut applied at the skim level is tightened to m_{ES} $> 5.22\,\mathrm{GeV}/c^2$.

5.6 Description of the backgrounds

5.6.1 Continuum background

Continuum decays are mis-reconstructed as signal when they contain a high-energy photon. This is produced mainly through two processes - Initial State Radiation (ISR) and highly asymmetric π^0/η decays. Figure 5.3 shows the event shapes in the c.m. frame of an asymmetric π^0/η continuum background (jet-like), compared to the decay of a pair of B mesons (spherical).

These two contributions have subtly different event shapes. Usually, the asymmetric $\pi^0/\ \eta$ is the result of one of the decays in a jet, the axial nature of which is evident in the centre-of-mass frame. ISR decays are slightly different, as the high energy photon carries away a significant portion of the incoming electron's energy before collision. The centre-of-momentum frame of the collision in this case is boosted compared to the usual centre-of-mass frame of the experiment. The resulting jets no longer appear back-to-back but rather each jet axis is bent

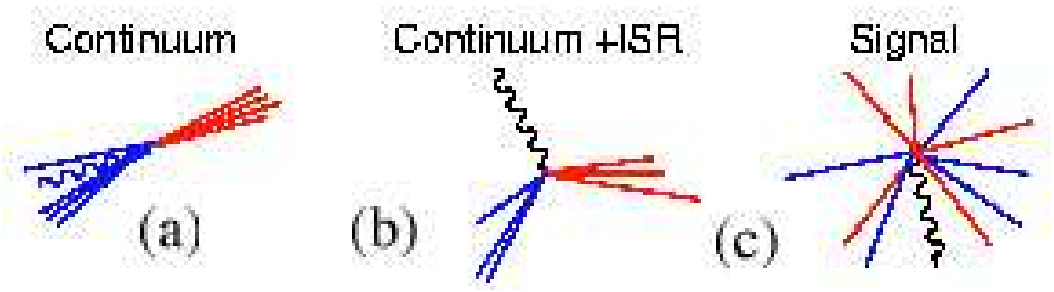

Figure 5.3: Event shape for (a) π^0/η continuum background (jet-like), (b) continuum background (ISR) and (c) signal decay (spherical) in the c.m. frame.

away from the direction of the ISR photon.

5.6.2 *B* backgrounds

Some amount of $b\bar{b}$ background is present in every decay mode. It is not as significant in quantity as the continuum background in this analysis, but nevertheless it must be carefully studied and understood. As generic B backgrounds are mis-reconstructed real B meson decays they share many characteristics of signal B decays. Some peak in both $m_{\rm ES}$ and ΔE^* thereby 'faking' true signal decays. This contribution could significantly bias the signal yield if not fully understood and modeled. Monte Carlo studies have been performed and it has been determined that the majority of B backgrounds which peak in ΔE^* and $m_{\rm ES}$ come from decays where the high energy photon is the result of a highly asymmetric π^0/η decay - from $b \to d\pi^0$ and $b \to d\eta$ decays.

There are other B backgrounds which peak in ΔE^* and $m_{\rm ES}$, known as 'cross-feed' backgrounds. These are dominated by $b \to s\gamma$ decays where a charged kaon is mis-identified as a pion. A smaller B background comes from $b \to d\gamma$ cross-feed, where a signal mode is mis-reconstructed as the wrong iType. Strict particle identification (PID) is required to combat the $b \to s\gamma$ cross-feed, described in more detail in Section 5.10. The dominant source of the remaining $b\bar{b}$ background is combinatoric $b \to c$ decays.

5.7 Background suppression variables

This section describes the variables used to improve background suppression, particularly the backgrounds from continuum and generic B decays described in the previous section.

Very few of the following discriminatory variables can be used in a direct cut. Differences between signal and background distributions tend to be too small to cut effectively whilst retaining an acceptable signal efficiency and variables are often highly correlated with one another. This analysis chooses instead to combine variables by a multi-variate method, using a neural network.

5.7.1 Event shape variables for continuum suppression

As described in Section 5.6.1, continuum events have a distinctive jet-like topology with subtle differences existing between ISR and asymmetric π^0/η decays. In general, the contribution from π^0/η decays dominates. This analysis must utilise variables that profit from both distinctive event topologies.

$cos\Theta_{B^*}$

Due to conservation of angular momentum, the polar angle of the $\Upsilon(4S)$ decay in the c.m. frame follows a $1 - cos^2\theta$ distribution, which is reflected in the polar angle distribution of the B ($cos\Theta_{B^*}$) with respect to the beam axis in the c.m. frame (see Figure 5.4). Continuum decays are uniformly distributed in $cos\Theta_{B^*}$ due to the small correlation between the thrust axis of the event and the beam axis.

$cos\theta_T$

Jet-like continuum events naturally show a high degree of correlation between the high energy photon direction and the jet axis. In a signal event, the decaying B-mesons are almost at rest in the c.m. frame. There is no correlation between the two B decay axes and so no relationship exists between the direction of the

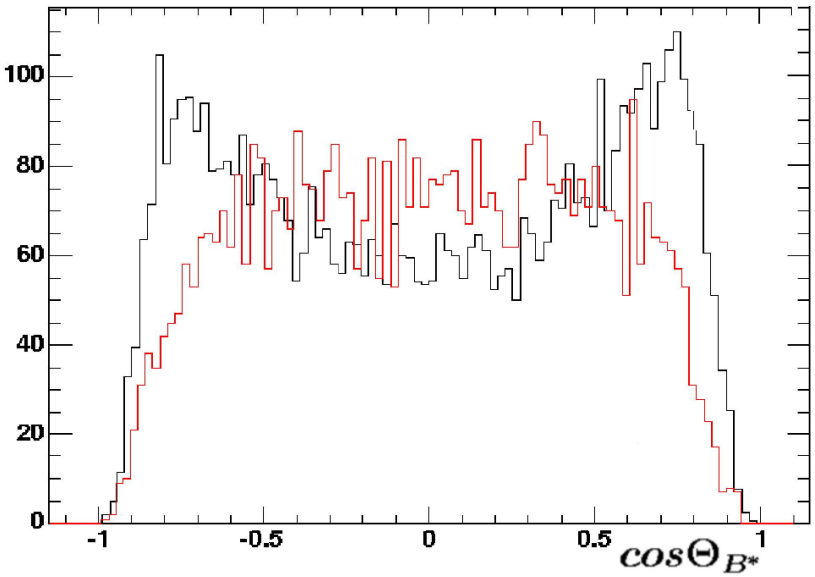

Figure 5.4: $cos\Theta_{B^*}$ distribution. Red: signal, black: continuum background

high energy γ and the other B decay.

θ_T is the angle between the daughter γ and the thrust of the rest of the event in the c.m. frame. The rest of the event (RoE) contains all charged particles (assuming pion mass) and all neutral particles (assuming photon mass) in the event that are not associated with the reconstructed B-meson. It is assumed to contain all decay products of the other B-meson.

The thrust axis $\vec{t}$ is a unit vector along the direction of maximum thrust T:

$$T = \frac{\Sigma_{i=1}^{N_{RoE}} |\vec{p_i}.\vec{t}|}{\Sigma_{i=1}^{N_{RoE}} |\vec{p_i}|} \tag{5.3}$$

There exists a two-fold ambiguity in T, allowing for $\vec{t}$ and $-\vec{t}$. The $|cos\theta_T|$ distribution peaks at one for continuum jet-like events and has a flat distribution for signal events. It is a very powerful discriminator and is used in the BToXdGamma skim to remove unwanted background events with the cut at $|cos\theta_T| < 0.8$. Even with such a cut applied, it remains a helpful variable for use in the Neural Net - see Figure 5.5.

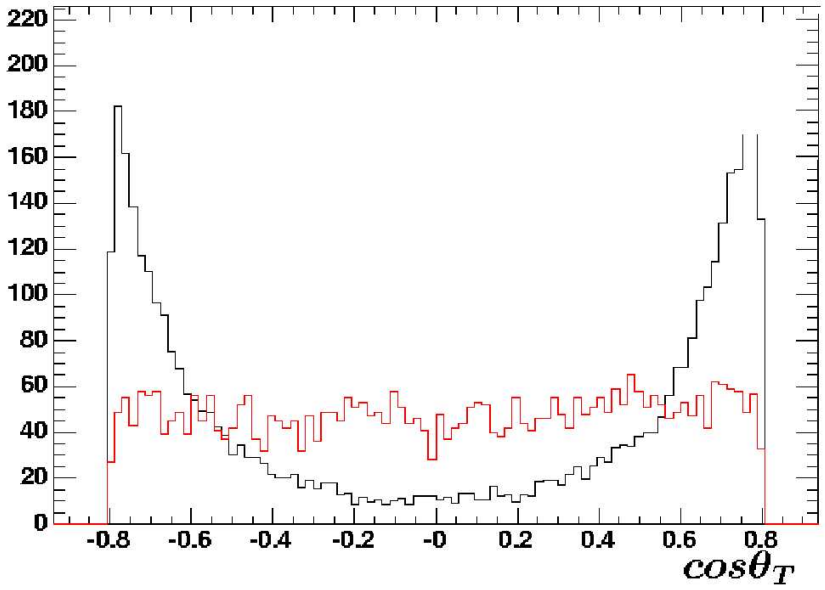

Figure 5.5: $cos\theta_T$ distribution. Red: signal, black: continuum background.

R_2'

As mentioned in Section 5.3, the 'jettiness' of an event can be measured with the second Fox-Wolfram moment. It can be used to successfully identify ISR events if calculated in the recoil frame relative to the γ. R_2' is the normalised second FW moment of the event-minus-photon in the recoil frame of the $\gamma$and is shown in Figure 5.6.

L-moments

A complete picture of event topology can be obtained by expanding the event shape in Legendre moments, which are calculated with respect to two directions:

- the direction of the high energy photon.
- the thrust axis of the rest of the event.

Over N particles, the longitudinal L-Moment is:

$$L_i = \frac{\Sigma_{j=1}^{N} |\vec{p_j}| x |cos\theta_j|^i}{\Sigma_{j=1}^{N} |\vec{p_j}|} \tag{5.4}$$

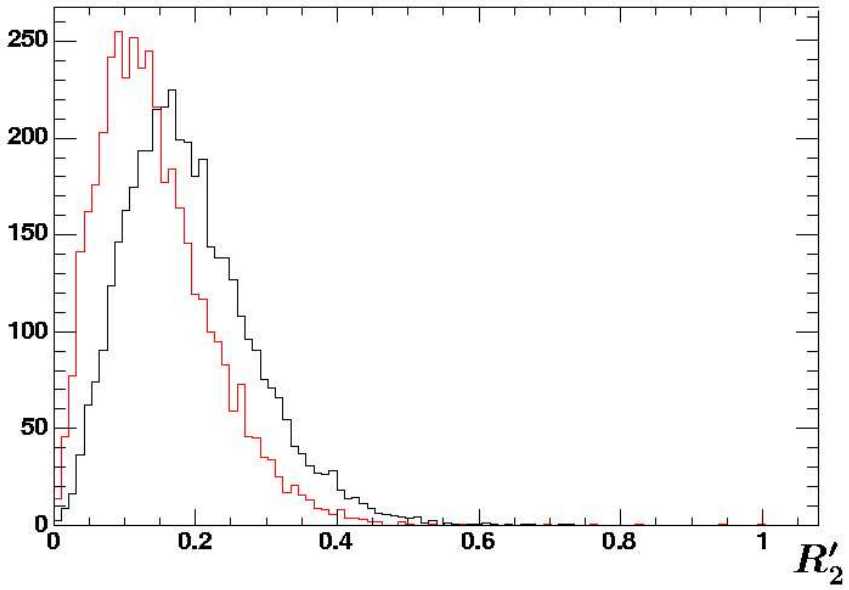

Figure 5.6: R_2' distribution. Red: signal, black: continuum background.

with θ_j = angle of $\vec{p_j}$ wrt the given axis and $cos\theta_j = (\vec{p_j}.\vec{a})/|\vec{p_j}|$. The perpendicular L-Moments simply replace $cos\theta_j$ with $sin\theta_j$. Figure 5.7 shows the distributions of the L-Moments used in this analysis.

5.7.2 Tagging variables

If a candidate B meson is properly reconstructed, the other particles in the rest of the event must result from the other B decay. Properties of the other B decay, such as the net kaon and lepton content, can be used to tag the flavour of the reconstructed candidate B. In this analysis, such information is only used to distinguish B meson decays from continuum decays.

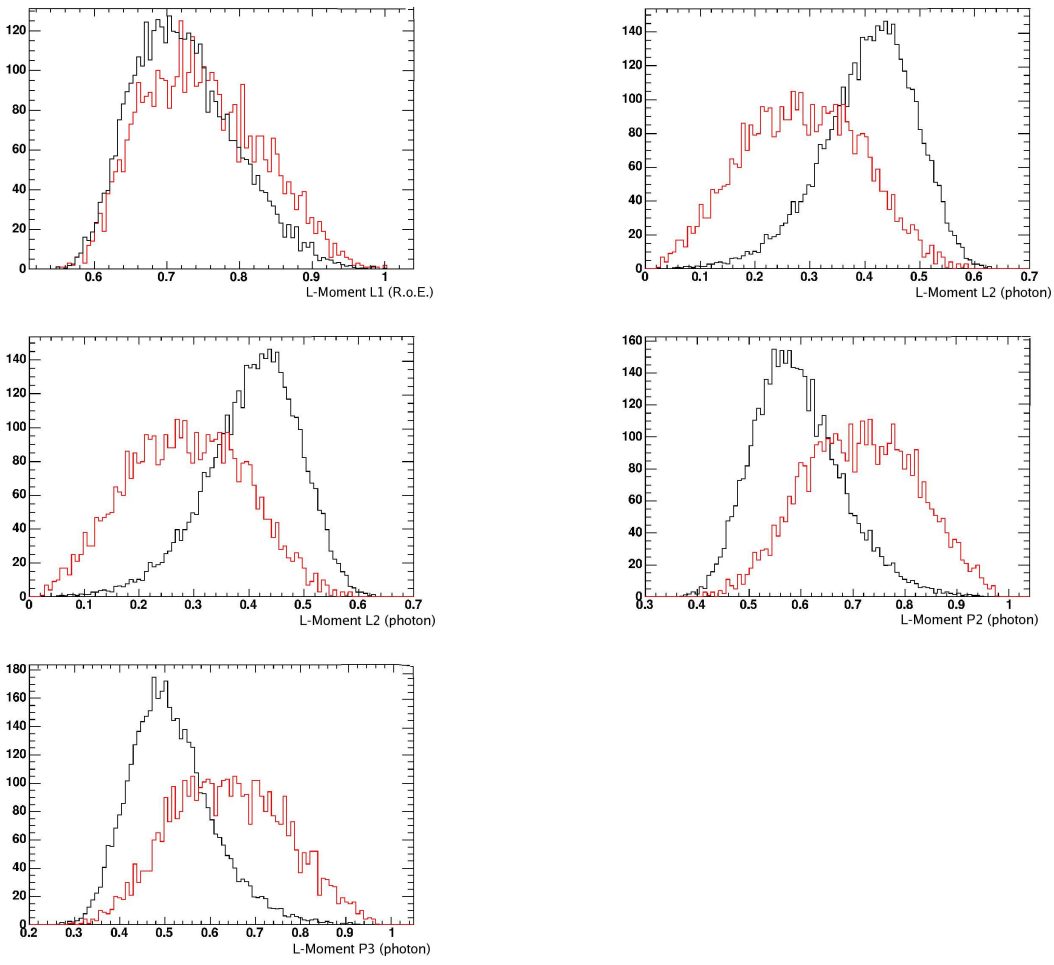

Figure 5.7: The distribution and shape of the L-Moments used in this analysis. Red: signal, black: continuum background.

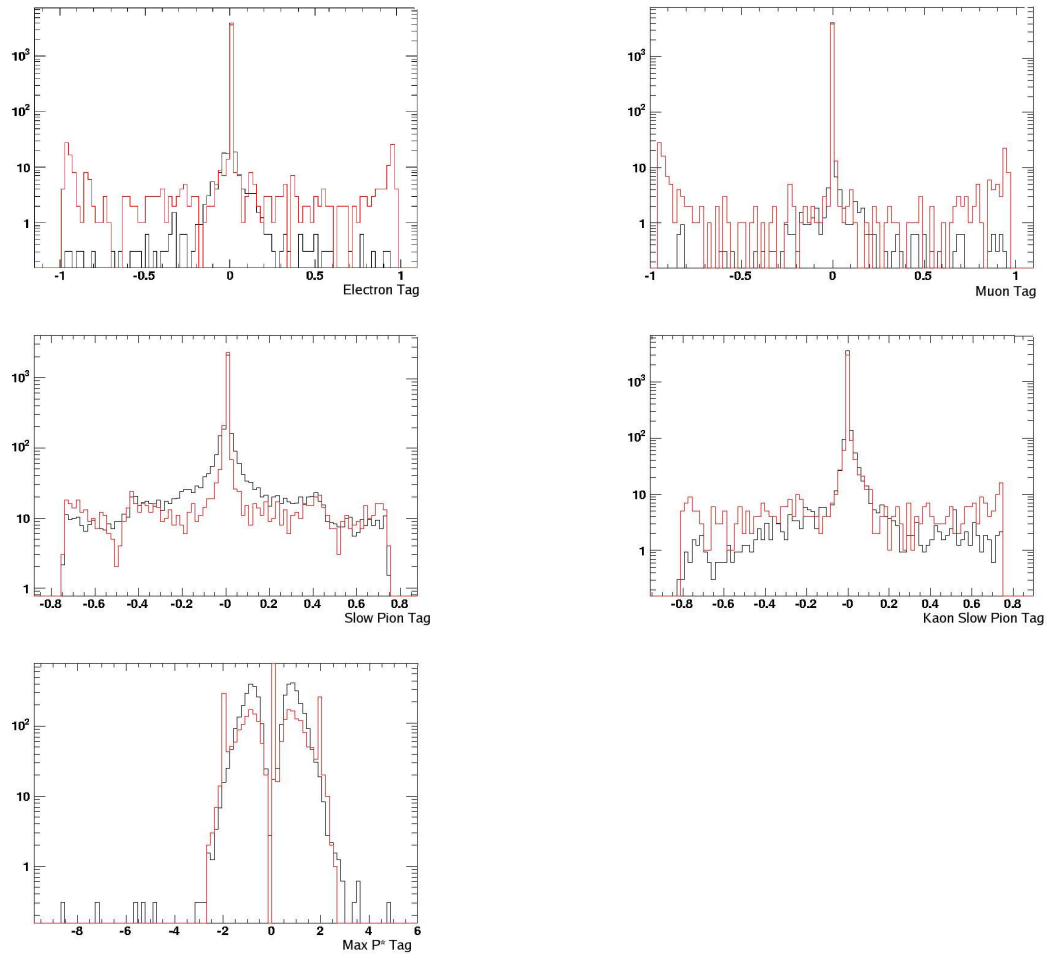

Figure 5.8: The distribution and shapes of the tagging variables used in this analysis. Red: signal, black: background.

Standard *BABAR* tagging variables

In the *BABAR* experiment, various B tagging algorithms have been developed to give the flavour of the non-reconstructed B and categorise it.

Electron Tag

The electron tag variable is the output of a Neural Net designed to recognise direct e^-s from the semi-leptonic decay of a B meson. The NN inputs are as follows:

- p^*, the c.m. momentum of the e^-.

- E_{90}^{W}, the energy in a hemisphere defined by the direction of the virtual $W^{\pm}$ of the assumed semi-leptonic B decay in the c.m. frame of the $\Upsilon(4S)$.

- $cos\theta_{miss}$, the angle between the e^- candidate momentum $\vec{p_e}$ and the missing momentum of the assumed tag B, p_{miss}.

The output of the neural net ranges from 0.0 - 1.0, with 1.0 denoting electron-like products of a semi-leptonic decay. The output of the tagging algorithm is simply the NN output multiplied by the sign of the charge of the e^-.

Muon Tag

As for the electron tag, but taking muon candidates.

Slow-Pion Tag

This variable uses a neural net to identify slow-pion daughters of a D^*, produced in a B-meson decay. It examines the members of the SlowPion list, which is made up of charged candidates not already identified as leptons or kaons and which have momentum $p^* < 0.25\,\mathrm{GeV}/c$.

The neural net takes as inputs:

- p^*: the c.m. momentum of the candidate pion.

- $|cos\theta_{thrust}|$: the angle between the candidate pion momentum and the rest of the event thrust axis, in the $\Upsilon(4S)$ rest frame.

- the output of PidKaonMicroSelector for the candidate pion (see Section 5.10 for a description).

The tagging output is constructed as for the electron tag, with the NN output multiplied by the sign of the charged slow-pion.

Kaon Slow Pion Tag

The kaon slow pion tag is a combination of the kaon and slow-pion tagging variables. It searches for correlated kaons and slow pions from the same B decay chain. Kaons and slow-pions are analysed in pairs, with neural net inputs as follows:

- The output of the tight PID selector for Kaons (see Section 5.10 for a full description).
- Slow-pion tag output for the slow-pion candidate.
- $cos\theta_{K,\pi}$: the angle between the kaon and slow-pion momenta, in the $\Upsilon(4S)$ rest frame.

The tag output value is the NN output value for the best kaon - slow-pion pair, multiplied by the flavour of the parent B-meson.

$\boldsymbol{P^*_{max}}$

The maximum c.m. momentum of all charged tagging candidates in the rest of the event is calculated, provided the charged particles pass the criteria:

- DOCA in x-y plane $< 0.1\,\mathrm{cm}$.
- DOCA in y plane $< 4\,\mathrm{cm}$.
- $p_{lab} < 10\,\mathrm{GeV}/c$.

where DOCA is as described in Section 5.3. This variable is more useful for flavour-tagging than for continuum background discrimination, but when combined with other variables it adds some power.

5.8 Neural Net for continuum suppression

As mentioned in Section 5.7, many variables useful in discriminating between signal and continuum decays do not lend themselves to making direct cuts. Instead, it is more effective to combine them into a multivariate measure which can more easily be cut upon. A neural network is an ideal method of combination, as it is a powerful discriminator. It can be successfully trained on relatively small input data samples and it automatically accounts for correlations between variables. More detailed information can be found in Chapter 4.

5.8.1 Neural Net configuration

This analysis used the ROOT TMultiLayerPerceptron function [30]. Many different combinations and permutations of input variables and network structure were tested and the optimal combination was found to be as follows.

The input variables are (as defined in Section 5.7):

- $cos\theta_B$.
- $cos\theta_T$.
- R_2'.
- The first longitudinal L-moment, taken wrt the thrust axis of the rest of the event.
- The second and third longitudinal L-moments, taken wrt the thrust axis of the high energy candidate photon.
- The second and third perpendicular L-moments, taken wrt the thrust axis of the high energy candidate photon.
- Electron Tag output.
- Muon Tag output.

- Slow-pion Tag output.
- Kaon Slow-pion Tag output.
- P^*_{max} Tag output.

The network has 13 input nodes and performed best with two hidden layers, the first with 10 and the second with 5 nodes. One output node exists, which gives a measure of the event shape with 0.0 being least and 1.0 being most signal-like. The batch training method was used, with equal number of signal and continuum Monte Carlo events used as training and test samples. 800 training cycles were necessary for optimal discrimination. The neural net output for signal and continuum background can be seen in Figure 5.9. The cut value of NN$>$ 0.87 was chosen by optimising the ratio of signal to continuum background.

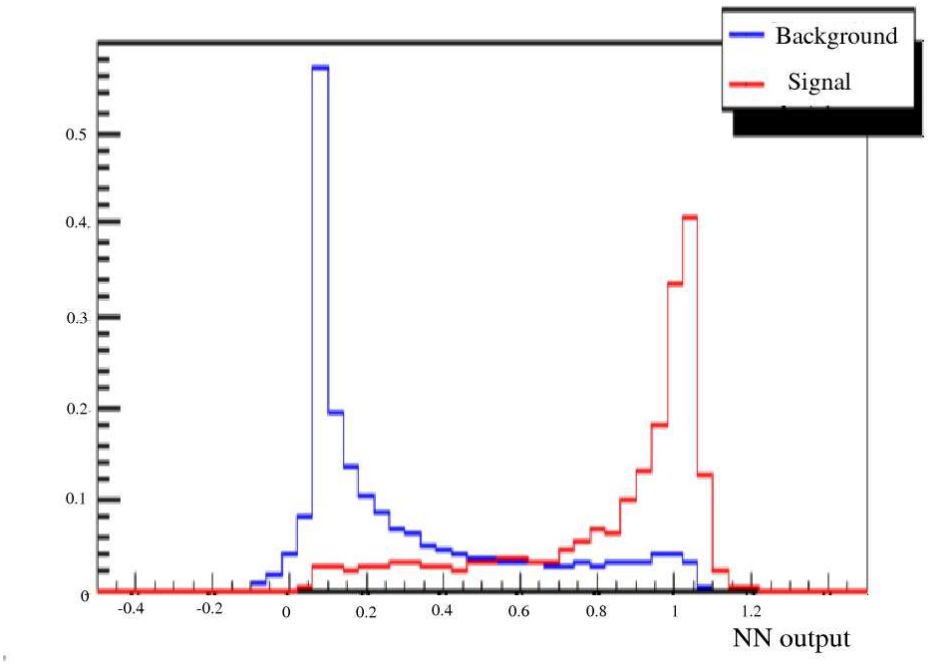

Figure 5.9: Neural net output. Red: signal, blue: continuum background. Plots normalised to the same area.

The output for generic B background is shown in Figure 5.10 and the effect of

MC/data type	cut at NN>0.87
signal MC	41.4%
generic B MC	33.6%
continuum uds MC	4.6%
continuum ccbar MC	4.3%
data	7.9%

Table 5.3: Neural net cut efficiencies.

the cut on the NN output for the various signal and background types are given in Table 5.3.

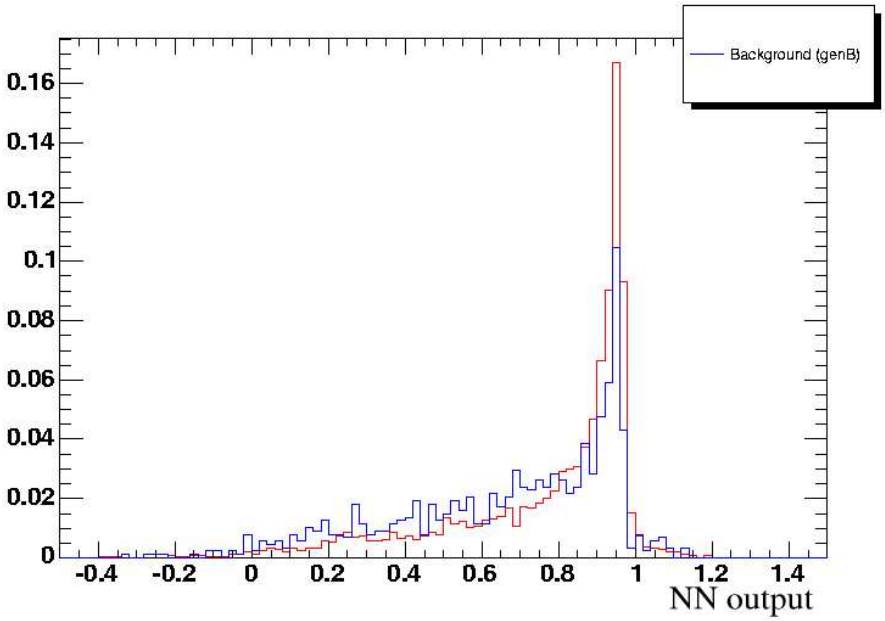

Figure 5.10: Neural net output. Red: signal, blue: generic B background. Plots normalised to the same area.

5.9 Generic B background suppression

Generic B backgrounds are hard to eliminate as they come from mis-reconstructed real B-meson decays and share many of the characteristics of signal decays.

The π^0/η veto described in Section 5.5.1 removes much of this background, but inevitably some remains and must be modelled. As mentioned in Section

5.6.2, the main contribution to generic B background in the $b \to d\gamma$ analysis is from asymmetric $b \to d\pi^0$ and $b \to d\eta$ decays. These have not been measured before in *BABAR*and a dedicated analysis is underway to measure the branching fractions of these decays.

For this thesis, signal-like peaking B backgrounds that are not removed with the π^0/η veto will simply be modelled with a peaking component in the likelihood fit. In later measurements it will be necessary to subtract the $b \to d\pi^0$ and $b \to d\eta$ backgrounds explicitly.

5.10 Kaon-pion discrimination

The *BABAR* Particle Identification (PID) Group has developed many analysis tools used to classify charged tracks into particle type. This analysis makes use of PID hadron selectors to discriminate between charged pions and kaons, a selection which is essential for the removal of the large peaking cross-feed background component from $b \to s\gamma$ decays.

In the *BABAR* framework, tracks are reconstructed with the assumption that all are charged pions. When considering all charged tracks in an event we look for one possible kaon candidate amongst them that would indicate a $b \to s\gamma$ decay, rather than $b \to d\gamma$ - for example, a $B^0 \to K^+\pi^-\gamma$ decay instead of $B^0 \to \pi^+\pi^-\gamma$.

Hadronic PID selectors are constructed using information from the three inner *BABAR* detector components - the Silicon Vertex Tracker, the Drift Chamber and the Detector of Internally Reflected Čerenkov Radiation. These systems are described in detail in Chapter 3.

The SVT and DCH provide measurements of the energy dE/dx deposited in them as well as a measure of the momentum of the charged particle. The DIRC provides information on the Čerenkov photons produced within it - the measured Čerenkov angle and the number of detected photons. As shown in Equation 3.1, the Čerenkov angle is related to the speed β of the particle as it travels through

the DIRC. This information, combined with the momentum measurements, allows for estimation of the mass of the charged particle.

A direct estimate of the particle type from the inferred mass is not the optimal use of data. Instead, the PID group has developed two methods of classification. The likelihood (LH) selectors use a calculation of the probability likelihood for each particle hypothesis - e^-, μ^-, π^-, K^- and proton. The SMS selectors combine the available information in a neural net trained to recognise particle type. In each case there exist binary selections (in ascending level of agreement with the particle hypothesis) - VeryLoose, Loose, Tight and VeryTight. The selectors are not mutually exclusive.

Because of the large backgrounds from $b \to s\gamma$ decays expected in this analysis, very tight particle identification is required to eliminate charged kaons from the pool of charged candidates. The PID LH selector PionVeryTight was selected for identification of charged pions. All charged daughters must pass this selection in order to be considered for the $b \to d\gamma$ sample. Its requirements are as follows:

- Kaon vs pion likelihood distribution < 0.2.
- Proton vs pion likelihood distribution < 0.5.
- Fails the Tight electron LH selector.
- Fails the VeryTight muon LH selector.

The efficiency of this selector varies as a function of particle momentum. At low momentum ($p < 2\,\mathrm{GeV}/c$) it has the greatest discriminatory power, as shown in Figures 5.11 and 5.12.

To select kaons for the $b \to s\gamma$ sample, the kaon-pion likelihood of each track is evaluated using PID information and the most kaon-like of all tracks is designated the possible $b \to s\gamma$ kaon candidate. The PID selector is simply reversed when applied to this candidate - the requirement for a $b \to s\gamma$ decay is that one charged daughter in the decay fails the PionVeryTight selector.

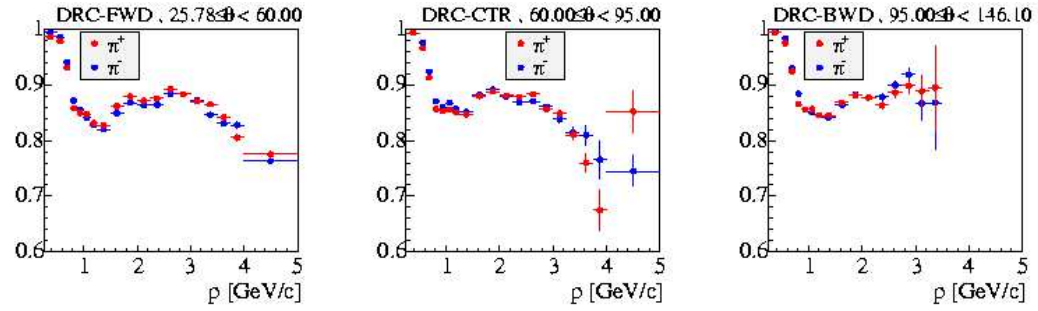

Figure 5.11: Pion selection efficiency for the PionVeryTight LH selector, in bins of polar angle.

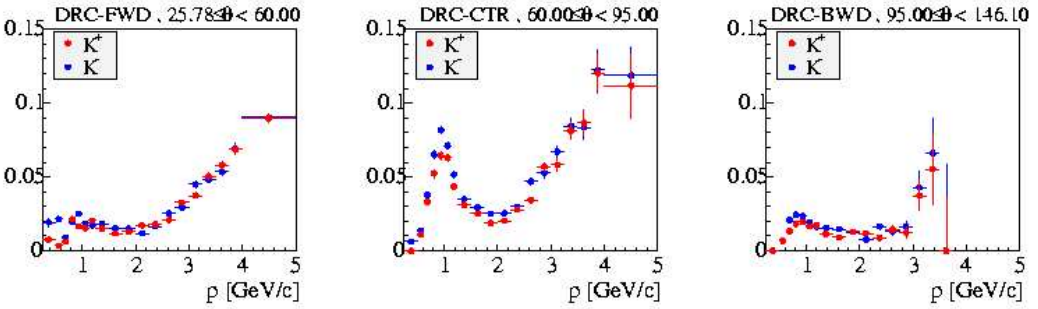

Figure 5.12: Kaon mis-identification for the PionVeryTight LH selector, in bins of polar angle.

5.11 Best candidate selection

Reconstructed events may contain more than one signal candidate, resulting from the mis-reconstruction of other particles in the event. After all selection cuts are applied there exists (on average) 1.21 candidates per event. Only one is selected.

Where a vertex exists in the event (i.e. for a candidate decay mode that contains more than one charged daughter), the best vertex χ^2 probability is used as the best candidate selector. Where no vertex exists, the best $\pi^0(\eta)$ mass is used. On very rare occasions, a mixture of different candidate decay modes is reconstructed, some with and some without a vertex. In this case, the candidate with the $\pi^0(\eta)$ mass or vertex probability closest to the ideal is chosen.

Cut Type	Cut Value	Efficiency (%)	Cumulative Efficency (%)
Mass region	0.6 - 1.8 GeV/c^2	100	
γ Second Moment	< 0.002	99.5	99.5
γ No. EMC Crystals	> 4	100	99.5
γ Dist. to charged bump	> 25 cm	97.1	96.7
γ noisy/dead EMC crystals	None	100	96.7
γ invariant mass - η Veto	500 MeV/c^2 - 590 MeV/c^2	99.0	95.6
γ invariant mass - π^0 Veto	105 MeV/c^2 - 155 MeV/c^2	89.5	86.1
Vertex $\chi 2$ Probability	> 0.02	68.4	58.4
π^0 Mass	177 MeV/c^2 - 145 MeV/c^2	96.2	55.9
Track Momentum	> 0.3 GeV/c	62.7	35.9
π^0 Momentum	> 0.3 GeV/c	80.4	30.6
$\lvert \cos \Theta_T \rvert$	< 0.8	83.7	24.8
Neural Net output - continuum suppression	> 0.87	41.4	11.5
ΔE^*	-0.3 GeV - 0.2 GeV	75.1	9.2
$m_{\rm ES}$	> 5.22 GeV/c^2	76.0	7.2
Kaon + pion PID	Passes	93.6	6.6
Best Candidate Selection		76.0	5.2

Table 5.4: Cut efficiencies for $b \to s\gamma$ signal MC.

5.12 Efficiencies

The efficiencies for each cut made alone and all the cuts cumulatively, are shown for $b \to s\gamma$ signal Monte Carlo in Table 5.4 and for $b \to d\gamma$ in Table 5.5. The efficiencies are calculated based on the number of events that have already passed the skim and beta level reconstruction.

Cut Type	Cut Value	Efficiency (%)	Cumulative Efficency (%)
Mass region	0.6 - 1.8 GeV/c^2	100	
γ Second Moment	< 0.002	99.1	99.1
γ No. Crystals	> 4	100	99.1
γ Dist. to charged bump	> 25 cm	98.5	98.8
γ noisy/dead EMC crystals	None	100	97.4
γ invariant mass - η Veto	500 MeV/c^2 - 590 MeV/c^2	93.3	90.4
γ invariant mass - π^0 Veto	105 MeV/c^2 - 155 MeV/c^2	88.8	79.4
Vertex $\chi 2$ Probability	> 0.02	65.1	58.6
π^0 Mass	177 MeV/c^2 - 145 MeV/c^2	91.1	53.8
Track Momentum	> 0.3 GeV/c	57.2	36.4
π^0 Momentum	> 0.3 GeV/c	75.5	28.8
$\lvert \cos\Theta_T \rvert$	< 0.8	83.7	26.2
Neural Net output - continuum suppression	> 0.87	47.2	14.3
ΔE^*	-0.3 GeV - 0.2 GeV	74.2	12.9
$m_{\rm ES}$	> 5.22 GeV/c^2	76.9	11.2
Pion PID	Passes	72.6	8.7
Best Candidate Selection		77.4	6.8

Table 5.5: Cut efficiencies for $b \to d\gamma$ signal MC.

Chapter 6

Fitting

6.1 Introduction

Following the selection cuts made in Chapter 5, we were left with two mutually exclusive samples of $b \to s\gamma$ and $b \to d\gamma$ decays separated by PID. The hadronic mass range of each sample covers $0.6\,\mathrm{GeV}/c^2$ - $1.8\,\mathrm{GeV}/c^2$. However, the low mass region is dominated by the $B \to K^*\gamma$ resonance in the $b \to s\gamma$ sample and the $B \to (\rho, \omega)\gamma$ resonances in the $b \to d\gamma$ sample. As a result of this, the two samples were split into low ($0.6\,\mathrm{GeV}/c^2$ - $1.0\,\mathrm{GeV}/c^2$) and high ($1.0\,\mathrm{GeV}/c^2$ - $1.8\,\mathrm{GeV}/c^2$) mass regions. Both low mass regions and the $b \to s\gamma$ high mass region were used as control samples for cross-checks of the analysis technique, as the branching fractions for the $B \to K^*\gamma$, inclusive $b \to s\gamma$ and $B \to (\rho, \omega)\gamma$ decays have been measured. The high mass $b \to d\gamma$ region was then used to measure the inclusive $b \to d\gamma$ branching fraction.

The signal and backgrounds were modeled from ΔE^* and m_{ES} distributions taken from the Monte Carlo samples with all cuts applied. This chapter describes the construction of the likelihood fit which was applied to these distributions and used to extract the number of signal events in the dataset. The tests performed to check the robustness of the fit are also described in this chapter, tests necessary to ensure the fit does not fail to converge and that it introduces no bias in the measured results. All fits presented here are based on studies of the high mass

	Signal	$b \to s\gamma$ cross-feed	B background	Continuum background	data
$b \to s\gamma$	0.1461	0.1123	-0.1159	-0.0504	-0.0212
$b \to d\gamma$	0.1076	0.0976	0.1251	-0.0392	-0.0765

Table 6.1: Correlations between ΔE^* and $m_{\rm ES}$ for the $b \to s\gamma$ and $b \to d\gamma$ Monte Carlo samples and data.

regions.

The number of signal events (signal 'yield') extracted from these fits can be converted into a measurement of the signal branching fraction using an estimated efficiency of the selection criteria, a process which is described in detail in Chapter 7.

6.2 The likelihood fit

The likelihood function $\mathcal{L}$ over a set of independent variables $\overrightarrow{x}$ is constructed from a set of Probability Density Functions (PDFs) $P(\overrightarrow{x})$. For M candidate signal and background hypotheses and for N events:

$$\mathcal{L} = exp\left(-\sum_{i=1}^{M} n_i\right) \cdot \left(\prod_{j=1}^{N}\left[\sum_{i=1}^{M} n_i P_i(\overrightarrow{x_j})\right]\right) \tag{6.1}$$

where n_i is the yield (the number of events) for each candidate hypothesis i. For this analysis, $\mathcal{L}$ is constructed as if the variables $\overrightarrow{x}$ are uncorrelated for each candidate hypothesis. In the fit, $\mathcal{L}$ is maximised over the parameter space to give the most likely values of the floating parameters which include the number of signal events.

The likelihood fits are implemented in the RooFit [36] package for the ROOT [37] data analysis framework. A two-dimensional likelihood fit is used in this analysis, with the ΔE^* and $m_{\rm ES}$ distributions as the inputs $\overrightarrow{x_j}$. The correlations between the variables for each candidate hypothesis as measured by the fitting software are given in Table 6.1. Given that the correlations are small, the two-dimensional PDF for each candidate hypothesis can be simplified to a product of two one-dimensional PDFs, with the *BABAR* Monte Carlo used to determine the

shapes of the PDFs.

6.2.1 Definition of PDFs

The PDFs to be used in this analysis are as follows:

- The Argus function is an empirical formula developed to model phase-space of multi-body decays near a threshold [35]. The formula is:

$$P(x) = x\left(1-\left(\frac{x}{m}\right)^2\right)^p \times exp\left(c\left(1-\left(\frac{x}{m}\right)^2\right)\right) \tag{6.2}$$

  where x is the observed $m_{\rm ES}$, $m \approx 5.29$ is the threshold value (the c.m. energy), c is the slope parameter and p is the power parameter, which is usually fixed at 0.5.

- The Gaussian function is a simple symmetric peaking distribution, described by the formula:

$$P(x) = exp\left(-0.5\left(\frac{x-\mu}{\sigma}\right)^2\right) \tag{6.3}$$

  where x is the observable, μ is the mean and σ the width of the peak.

- The Crystal-Ball (CB) function is a Gaussian with a tail on the low side that is useful in modelling the effect of radiative energy loss. The formula is as follows:

$$P(x<-|\alpha|) = \frac{(\frac{n}{|\alpha|})^n e^{-\frac{1}{2}\alpha^2}}{(\frac{n}{|\alpha|}-|\alpha|-x)^2}, \qquad P(x>-|\alpha|) = exp\left(-\frac{1}{2}\left(\frac{x-\mu^2}{\sigma}\right)\right) \tag{6.4}$$

  The parameter α describes the point at which the tail joins the peaking shape and n is the tail shape parameter.

- The polynomial function is used to describe the ΔE^* background in B-decay studies:

$$P(x) = 1 + \sum_{i=1}^{M} a_i x^i \tag{6.5}$$

  In this analysis we use a 2nd degree polynomial, with $M = 2$.

mode	Candidate hypothesis	$m_{\rm ES}$	ΔE^*
$b \to s\gamma$	Signal	Crystal-Ball	Crystal-Ball
	$b \to s\gamma$ cross-feed	Gaussian + Argus	Gaussian + Polynomial
	generic B background	Gaussian + Argus	Gaussian + Polynomial
	Continuum background	Argus	Polynomial
$b \to d\gamma$	Signal	Crystal-Ball	Crystal-Ball
	$b \to s\gamma$ cross-feed	Gaussian + Argus	Gaussian + Polynomial
	generic B background	Gaussian + Argus	Gaussian + Polynomial
	Continuum background	Argus	Polynomial

Table 6.2: PDF shapes used in the likelihood fit for each candidate hypothesis.

6.2.2 Composition of PDFs

ΔE^* and $m_{\rm ES}$ are described in the likelihood fit by a sum of 2D PDFs, one for each candidate hypothesis. The parameters of these PDFs were obtained from fits to ΔE^* and $m_{\rm ES}$ distributions of Monte Carlo simulated signal and background decays. The PDF shapes used are summarised in Table 6.2.

When the likelihood fit is applied to real data, several parameters defining the shapes of of the $m_{\rm ES}$ and ΔE^* distributions are allowed to 'float' - they become variables in the parameter space over which the likelihood function is maximised. The Monte Carlo simulation of detector response is not perfect, so in order to avoid possible systematic errors associated with this it is preferable to float as many shape parameters as possible. However, it is not possible to float everything as the maximisation fit may fail to converge if the likelihood function is too general. As many parameters as possible are therefore allowed to float, as described below and summarised in Table 6.3. The systematic errors stemming from fixing parameters are described in Section 7.6.

Signal $b \to s\gamma$ and $b \to d\gamma$ were described in both ΔE^* and $m_{\rm ES}$ by a Crystal-Ball function. The means of both shapes were allowed to float in the $b \to s\gamma$ likelihood fit with other parameters fixed. In the $b \to d\gamma$ likelihood fit, both were completely fixed to the $b \to s\gamma$ signal shape.

The $b \to s\gamma$ cross-feed background in both samples was modeled in ΔE^* with

a Gaussian that fits the peaking component and a polynomial function that fits the combinatoric component. In $m_{\rm ES}$, the peaking component was fitted with a Gaussian and the combinatoric with an Argus.

Generic B backgrounds were fitted with the same shapes as the $b \to s\gamma$ cross-feed background to allow for a possible peaking component. $b \to d\gamma$ cross-feed was ignored in the $b \to s\gamma$ sample as it is vanishingly small, but included in the $b \to d\gamma$ sample. $b \to d\gamma$ cross-feed has the same shape as generic B background in this sample and is combined with this background in the fit.

The $b \to s\gamma$ cross-feed and generic B shapes were completely fixed from Monte Carlo in the final likelihood fit. The generic B yield was fixed and in the $b \to d\gamma$ sample the $b \to s\gamma$ cross-feed yield was fixed using the branching fraction found in the $b \to s\gamma$ fit. In the fit to the $b \to s\gamma$ sample, the $b \to s\gamma$ cross-feed component is proportional to the $b \to s\gamma$ signal yield. The ratio of signal yield to the combined signal plus cross-feed yield was therefore fixed, but the total number of signal+cross-feed candidates found was allowed to float. From Monte Carlo simulation, the ratio of $b \to s\gamma$ signal to signal+cross-feed was found to be 0.385.

Continuum background in both samples was fitted with a polynomial in ΔE^* and an Argus function in $m_{\rm ES}$. The shape parameters of the polynomial and Argus shapes and the yield from this component were floated in the likelihood fit for both samples. Fits to signal and each background category to simulations for the $b \to s\gamma$ and $b \to d\gamma$ samples are shown in Figures 6.1 to 6.4.

Table 6.3 summarises the fixed and floating parameters in the final likelihood fit.

6.3 Toy Monte Carlo studies

The final likelihood function was constructed by summing the individual 2-D PDFs shown in Table 6.2. To validate the fit and ensure these PDFs do not

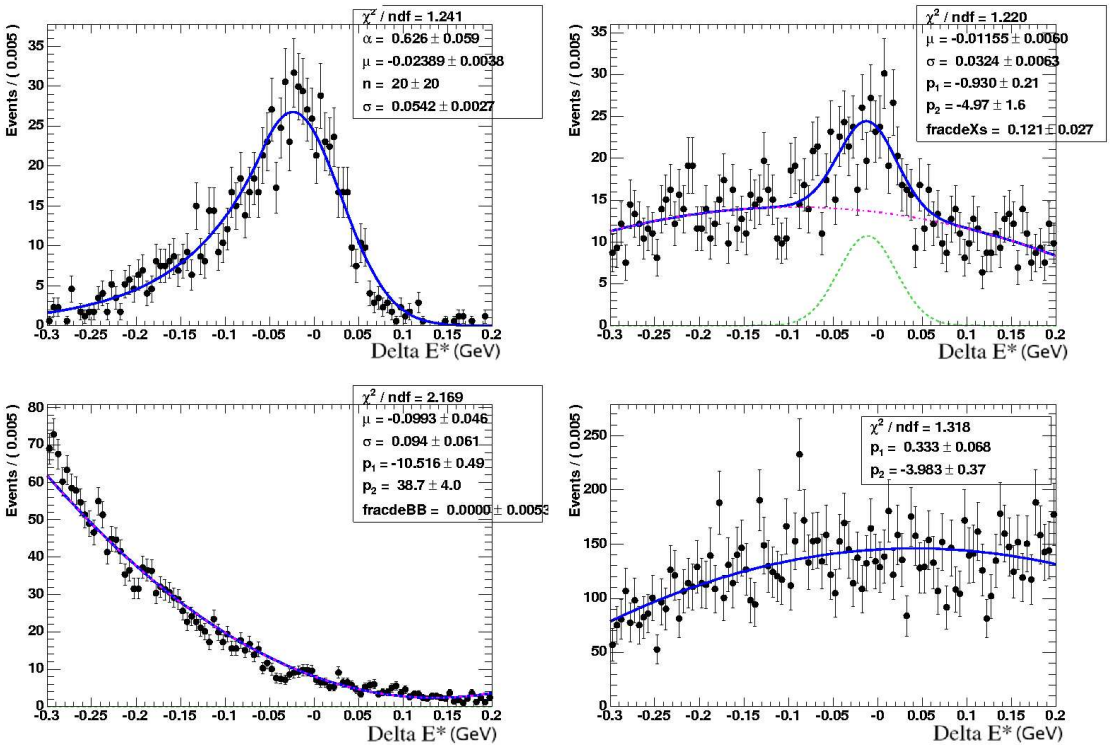

Figure 6.1: The PDFs for ΔE^* in each $b \to s\gamma$ Monte Carlo type. Top left: signal. Top right: $b \to s\gamma$ cross-feed (peaking component in green, combinatoric component in pink). Bottom left: generic B background (peaking component in green, combinatoric component in pink). Bottom right: continuum background.

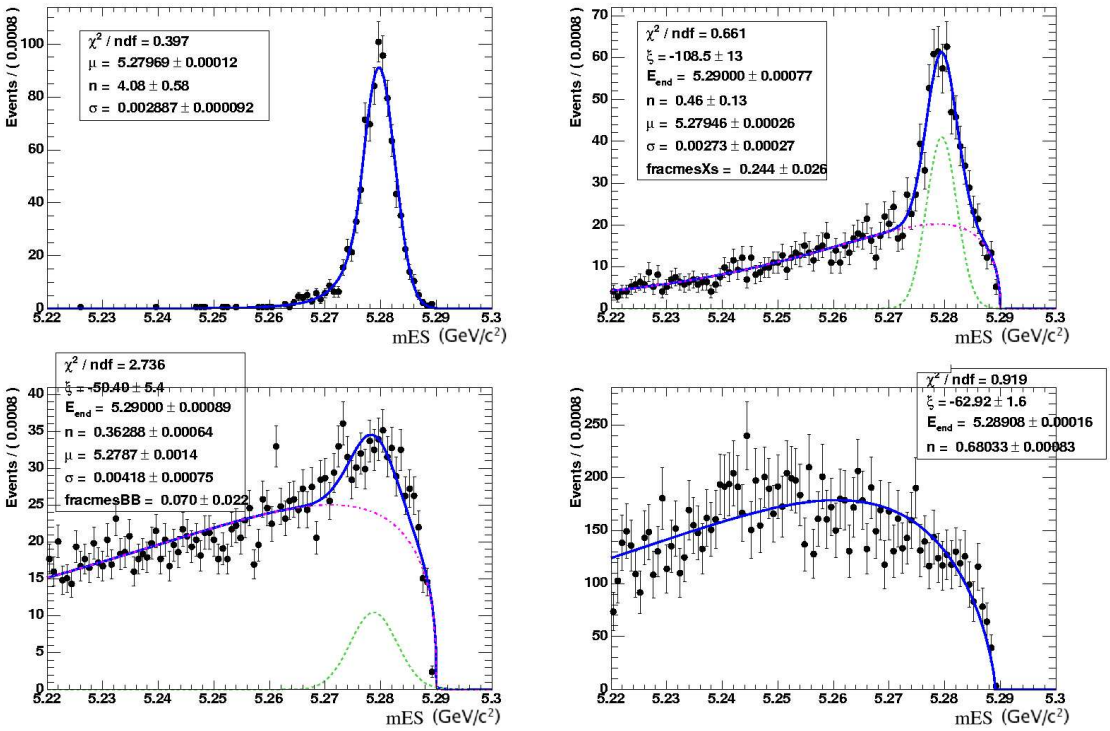

Figure 6.2: The PDFs for $m_{\rm ES}$ in each $b \to s\gamma$ Monte Carlo type. Top left: signal. Top right: $b \to s\gamma$ cross-feed (peaking component in green, combinatoric component in pink). Bottom left: generic B background (peaking component in green, combinatoric component in pink). Bottom right: continuum background.

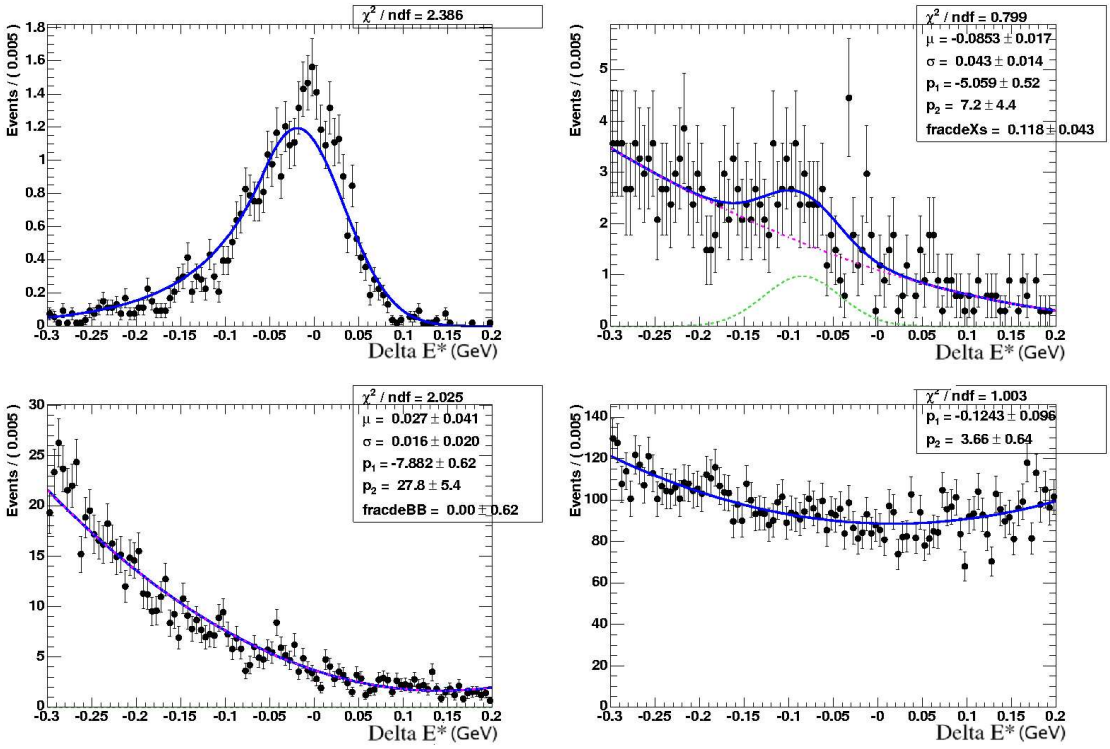

Figure 6.3: The PDFs for ΔE^* in each $b \to d\gamma$ Monte Carlo type. Top left: signal. Top right: $b \to s\gamma$ cross-feed (peaking component in green, combinatoric component in pink). Bottom left: generic B background (peaking component in green, combinatoric component in pink). Bottom right: continuum background.

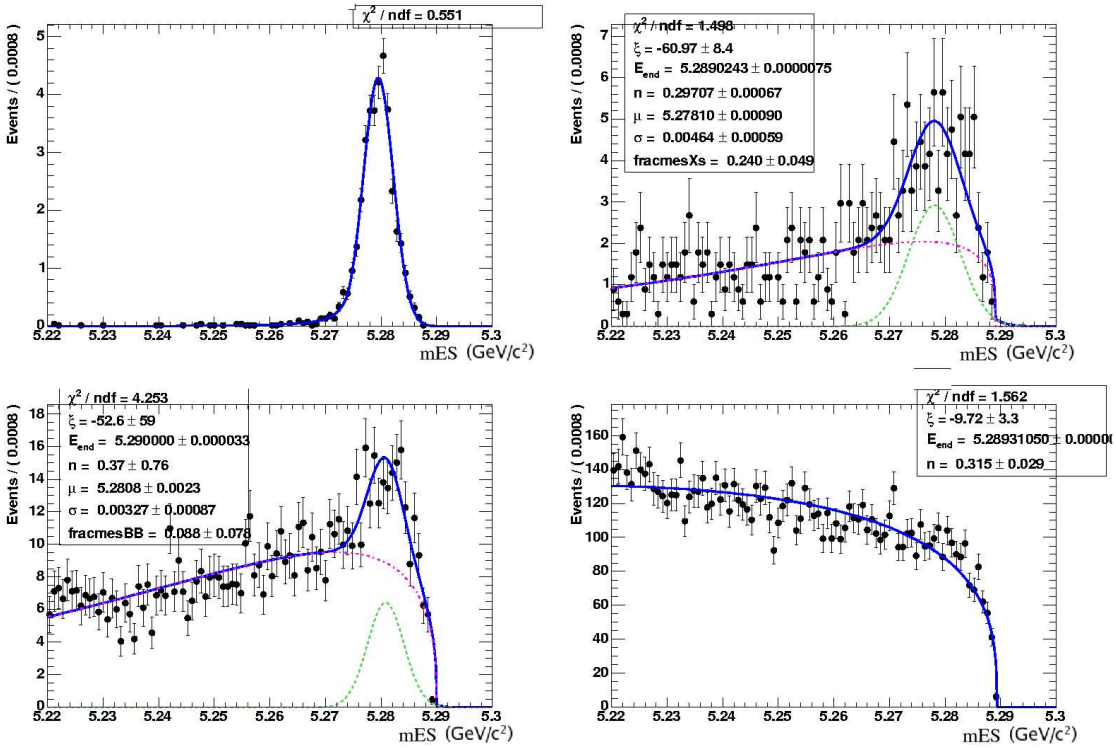

Figure 6.4: The PDFs for m_{ES} in each $b \to d\gamma$ Monte Carlo type. Top left: signal. Top right: $b \to s\gamma$ cross-feed (peaking component in green, combinatoric component in pink). Bottom left: generic B background (peaking component in green, combinatoric component in pink). Bottom right: continuum background.

mode	Candidate hypothesis	PDF	fixed	floated
$b \to s\gamma$	Signal		Ratio of Sig:cross-feed	Sig+cross-feed yield
		$m_{\rm ES}$ CB	α, n, σ	μ
		ΔE^* CB	α, n, σ	μ
	$b \to s\gamma$ cross-feed		Ratio of Sig:cross-feed	Sig+cross-feed yield
		$m_{\rm ES}$ Gaussian	μ, σ	
		$m_{\rm ES}$ Argus	m, c, p	
		ΔE^* Gaussian	μ, σ	
		ΔE^* Polynomial	$P01, P02$	
	generic B background		yield	
		$m_{\rm ES}$ Gaussian	μ, σ	
		$m_{\rm ES}$ Argus	m, c, p	
		ΔE^* Gaussian	μ, σ	
		ΔE^* Polynomial	$P01, P02$	
	Continuum background			yield
		$m_{\rm ES}$ Argus	m, p	c
		ΔE^* Polynomial		$P01, P02$
$b \to d\gamma$	Signal			yield
		$m_{\rm ES}$ CB	α, n, μ, σ	
		ΔE^* CB	α, n, μ, σ	
	$b \to s\gamma$ cross-feed		yield	
		$m_{\rm ES}$ Gaussian	μ, σ	
		$m_{\rm ES}$ Argus	m, c, p	
		ΔE^* Gaussian	μ, σ	
		ΔE^* Polynomial	$P01, P02$	
	generic B background		yield	
		$m_{\rm ES}$ Gaussian	μ, σ	
		$m_{\rm ES}$ Argus	m, c, p	
		ΔE^* Gaussian	μ, σ	
		ΔE^* Polynomial	$P01, P02$	
	Continuum background			yield
		$m_{\rm ES}$ Argus	m, p	c
		ΔE^* Polynomial		$P01, P02$

Table 6.3: Summary of parameters fixed/floated in the final likelihood fit.

produce any inherent bias in the signal yield, several toy Monte Carlo studies were performed.

Toy Monte Carlo studies are a tool for examining the robustness of the likelihood fit and for estimating some of the systematic uncertainties associated with a fitting procedure. In a toy Monte Carlo study, the likelihood fit is applied to many (usually 1000) prototype datasets (referred to as toy datasets or toy experiments), generated using the Monte Carlo method. The $m_{\rm ES}$ and ΔE^* distributions of the simulated toy datasets can either be taken as the PDFs used in the likelihood fit, or taken from Monte Carlo events that have been passed through the full detector simulation.

If the ΔE^* and $m_{\rm ES}$ distributions are uncorrelated for each candidate hypothesis and the distributions are perfectly modeled by the empirical fit to the fully simulated *BABAR* Monte Carlo, then the likelihood fit applied to the toy experiments should reproduce the values of the floating parameters used to generate the toy experiments. There are statistical fluctuations of the floating fit parameters, but the ensemble distributions of each parameter should follow a Gaussian shape with the mean at the generator value.

A commonly used figure of merit is the 'pull' of a floating parameter p, which is a test of the stability of the fit. For an unbiased likelihood fit, the pull distribution obtained from a large set of toy experiments is a Gaussian distribution with a mean of zero and a width $\sigma_p = 1$:

$$pull = \left(\frac{p_{generator} - p_{fit}}{\sigma_p} \right).$$

Significant deviations from these values in the pull distributions are indicative of a possible problem with the likelihood fit.

6.3.1 Pure toy Monte Carlo studies

Pure toy Monte Carlo studies are so-called because the toy datasets are generated purely from the PDFs used in the likelihood fit. In this analysis, they were used

	Signal BF	Signal	$b \to s\gamma$ cross-feed	Generic B	Continuum
$b \to s\gamma$	3.55×10^{-4}	935	1493	1968	12912
$b \to d\gamma$	1×10^{-5}	38	334	752	9684

Table 6.4: Expected yields for each fit component and the branching fractions (BF) used to estimate yields, assuming 222 million $B\bar{B}$ pairs. $b \to s\gamma$ branching fractions taken from world average [1] and $b \to d\gamma$ branching fraction estimated.

to test the robustness of the fitting procedure, to ensure the fit always converges and to obtain an initial estimate of the fit's sensitivity to expected signal levels.

The selection efficiencies described in Chapter 5, combined with the best available measurements of the branching fractions of the various data types gave a projected composition of the real $202\,\text{fb}^{-1}$ dataset for each of the modes described in Table 6.4 using the formula:

$$\text{yield} = \text{n}B\bar{B}\text{ pairs} \times \text{efficiency} \times BF \tag{6.7}$$

with n$B\bar{B}$ pairs = 222×10^6 (see Section 7.1) and BF is the branching fraction. These expected yields were used to set the proportions of each signal and background type and the PDFs described in Section 6.2.2 were used to model the shapes of each type. Together this information was used to generate ensembles of toy datasets for each mode.

Each toy dataset contained a randomly generated number of candidates of each type, generated from a Poisson distribution with the mean at the expected yield. Poissonian statistical fluctuations were allowed for all free parameters. The likelihood function described in Section 6.2 was maximised over each of the toy datasets in the ensemble and the fitted values of the floating parameters compared to the input values. 1000 such toys were produced in each study. Figure 6.5 shows the pull distribution (fitted with a Gaussian) of the signal yield for the $b \to s\gamma$ fit and Figure 6.6 for the $b \to d\gamma$ fit. Table 6.6 and Table 6.5 give the pull and error on the pull for each variable floated in the likelihood fit.

The signal yields and the errors on the signal yields are shown in Figure 6.7 and summarised in Table 6.7. It should be noted that the 'signal' yield measured

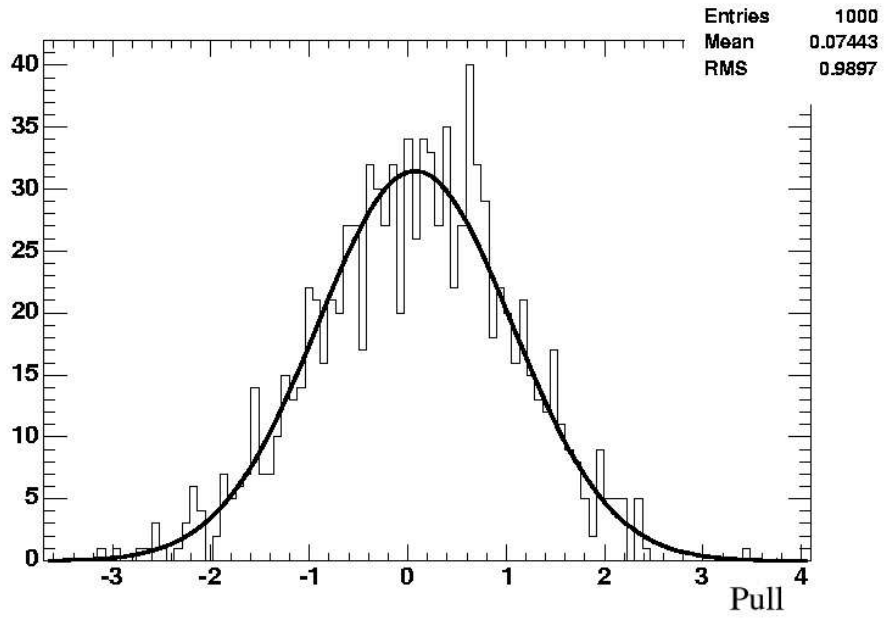

Figure 6.5: Pull distribution for the number of the combined signal and cross-feed events found in the $b \to s\gamma$ fit, based on 1000 generated pure toy Monte Carlo experiments.

	$N_{Sig+Xfeed}$	N_{Cont}	c	P01	P02
$b \to s\gamma$	0.074 ± 0.031	-0.045 ± 0.032	-0.089 ± 0.030	-0.012 ± 0.032	0.007 ± 0.031

	$\mu_{m_{\rm ES}}$	$\mu_{\Delta E^*}$
$b \to s\gamma$	0.014 ± 0.032	-0.013 ± 0.032

Table 6.5: Pull and error on pull for those variables floated in the $b \to s\gamma$ pure toy fits.

for $b \to s\gamma$ is in fact the yield of signal and cross-feed combined, with a ratio of signal/signal+cross-feed = 0.385. The number of signal events can easily be extracted from the total and the statistical error on the $b \to s\gamma$ signal yield was taken to be the same percentage as the uncertainty on the combined yield. The pulls of the variables floated in the likelihood fit were found to be small in most cases, but even the larger pulls give a small shift in the overall signal yield compared to the statistical error and can therefore be ignored. The small pulls of the signal yields indicated the fit was an unbiased estimator of the signal yield under the assumption that the PDFs of the fit correspond to the true PDFs.

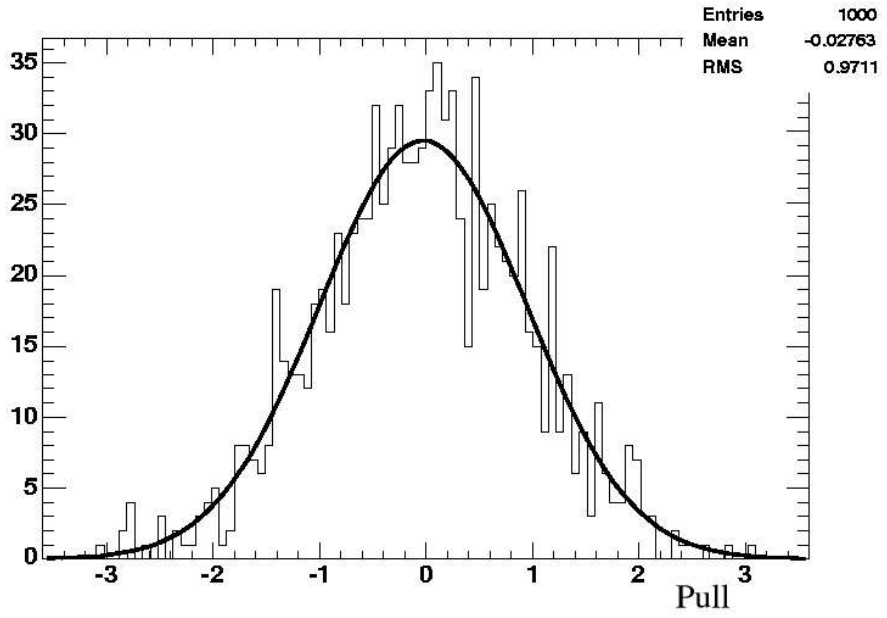

Figure 6.6: Pull distribution for the number of signal events found in the $b \to d\gamma$ fit, based on 1000 generated pure toy Monte Carlo experiments.

	N_{Sig}	N_{Cont}	c	P01	P02
$b \to d\gamma$	-0.028 ± 0.031	-0.0089 ± 0.031	0.11 ± 0.61	-0.048± 0.032	-0.096 ± 0.032

Table 6.6: Pull and error on pull for those variables floated in the $b \to d\gamma$ pure toy fits.

6.3.2 Embedded toy Monte-Carlo studies

Although correlations between ΔE^* and $m_{\rm ES}$ for signal Monte Carlo were small (see Table 6.1), it was worth examining the effect these correlations have on the fit by performing an embedded toy Monte Carlo study.

BABAR Monte Carlo simulations resemble real data more than a PDF-generated distribution, which includes only statistical fluctuations. By including the ΔE^*

	Toy input	Mean Fit Yield	Mean Fit Error	Error(%)
$b \to s\gamma$ $N_{Sig+Xfeed}$	2338	2347.0	107 6	4.6
$b \to d\gamma$ N_{Sig}	38	37.9	27.6	72.8

Table 6.7: The estimated sensitivity from the pure toy likelihood fit for each decay mode with 222 million $B\bar{B}$ pairs.

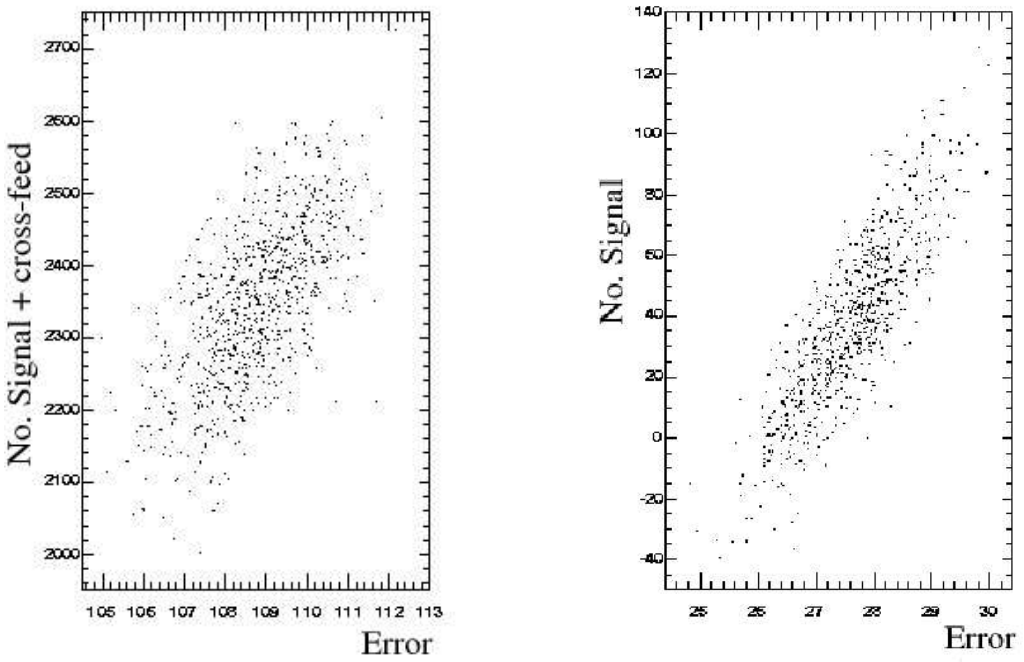

Figure 6.7: The signal yield and error distributions for each decay type for pure toy Monte Carlo studies. Left: $b \to s\gamma$. Right: $b \to d\gamma$.

and $m_{\rm ES}$ distributions of events from the fully simulated Monte Carlo these correlations could be introduced into the toy samples. Any possible bias in the signal yield created by ignoring the correlations could be studied in this way.

ΔE^* and $m_{\rm ES}$ values from individual signal Monte Carlo events were included in the PDF-generated distributions of $b \to s\gamma$ cross-feed, generic B and continuum backgrounds to create a 'signal-embedded' toy study. Embedded toy Monte Carlo studies represent a necessary compromise. Ideally, every dataset in a toy study would draw all of its events from fully simulated Monte Carlo to preserve correlations between the variables. However, simulation is time and computer intensive and not enough signal (and certainly not enough generic B and continuum background) Monte Carlo exists to create the desired ensemble of 1000 completely independent toy datasets. A random selection of ΔE^* and $m_{\rm ES}$ pairs from signal Monte Carlo events was therefore included with the recognition that the toy datasets produced from them were not completely independent.

	$N_{Sig+Xfeed}$	N_{Cont}	c	P01	P02
$b \to s\gamma$	0.24 ± 0.032	-0.161 ± 0.027	0.18 ± 0.031	0.075 ± 0.031	0.040 ± 0.032

	$\mu_{m_{\rm ES}}$	$\mu_{\Delta E^*}$
$b \to s\gamma$	0.024 ± 0.032	-0.043 ± 0.032

Table 6.8: Pull and error on pull for those variables floated in the $b \to s\gamma$ signal-embedded toy fits.

The study consists of 1000 toy datasets generated to represent 222 million $B\bar{B}$ pairs, using the expected yields given in Table.6.4. Figure 6.8 and Figure 6.9 show the pull distribution for the signal yield in each decay type, fitted with a Gaussian. The pulls are summarised in Table 6.8 for the $b \to s\gamma$ sample and Table 6.9 for the $b \to d\gamma$ sample. The signal yields and the associated errors are shown in Figure 6.10 and summarised in Table 6.10.

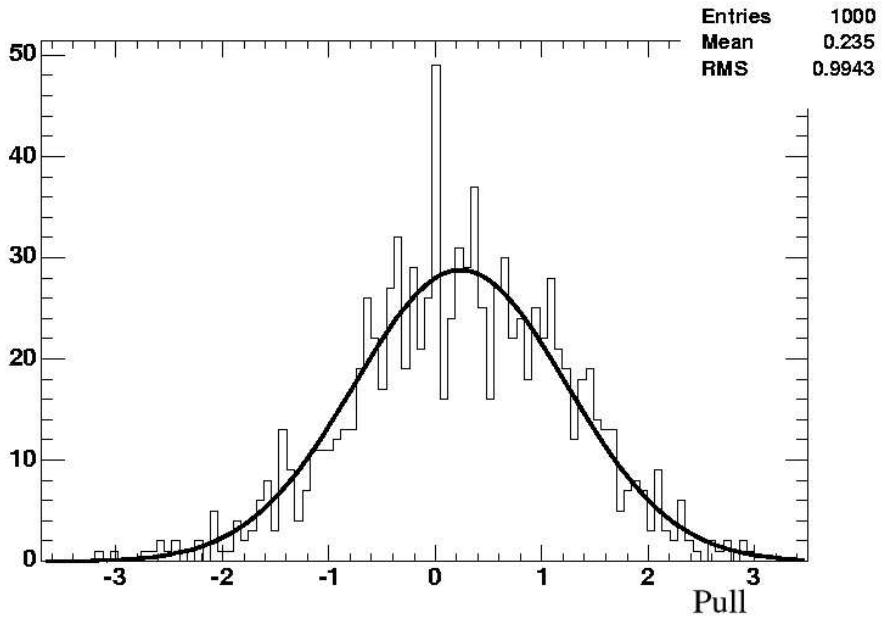

Figure 6.8: Pull distribution for the number of signal events found in the $b \to s\gamma$ fit, based on 1000 generated toy Monte Carlo experiments with $b \to s\gamma$ signal Monte Carlo events embedded.

From the small pulls observed in both the $b \to s\gamma$ and the $b \to d\gamma$ signal-embedded toy studies, it can be concluded that ignoring correlations between the fit variables ΔE^* and $m_{\rm ES}$ does not give a significant bias in the fit results and

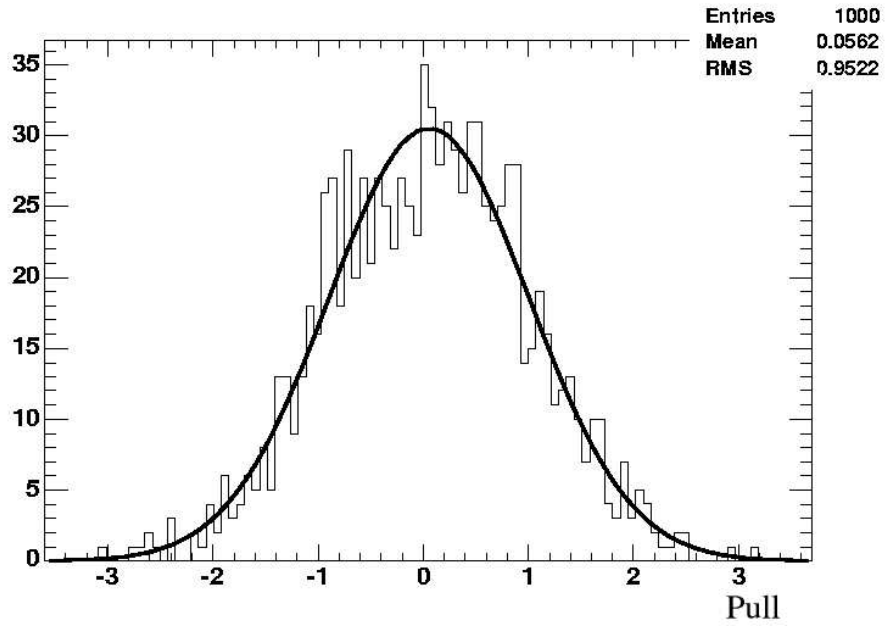

Figure 6.9: Pull distribution for the number of signal events found in the $b \to d\gamma$ fit, based on 1000 generated toy Monte Carlo experiments with $b \to d\gamma$ signal Monte Carlo events embedded.

	N_{Sig}	N_{Cont}	c	P01	P02
$b \to d\gamma$	0.056 ± 0.030	-0.051 ± 0.078	0.20 ± 0.09	0.042 ± 0.032	0.025 ±0.31

S

Table 6.9: Pull and error on pull for those variables floated in the $b \to d\gamma$ signal-embedded toy fits.

no systematic error will be assigned from this source. The largest pull observed was 0.240±0.032, given in Table 6.8, which comes from the number of signal plus cross-feed in the $b \to s\gamma$ sample. This arises from the interplay of the continuum shape and the combinatoric component of the cross-feed shape. In a dedicated $b \to s\gamma$ measurement this should be studied in more detail and a systematic error assigned, but here it is much smaller than the expected statistical error of 5% and can be neglected.

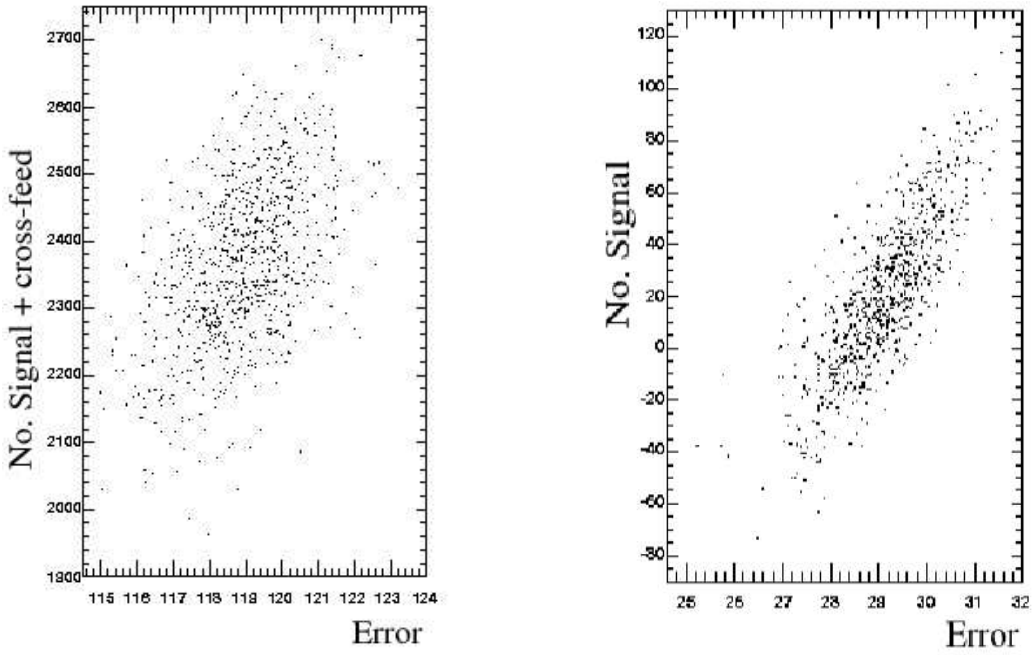

Figure 6.10: The signal yield and error distributions for each decay type for signal-embedded toy Monte Carlo studies. Left: $b \to s\gamma$. Right: $b \to d\gamma$.

	Toy input	Mean Fit Yield	Mean Fit Error	Error(%)
$b \to s\gamma$ $N_{Sig+Xfeed}$	2338	2367	118.9	5.0
$b \to d\gamma$ N_{Sig}	38	40.2	27.6	68.6

Table 6.10: The estimated sensitivity from the signal-embedded toy likelihood fit for each decay mode with 222 million $B\bar{B}$ pairs.

Chapter 7

Results

7.1 Introduction

The previous chapter described the fitting procedure and verified that no bias in the signal yield was produced by the fit technique in Monte Carlo studies. The likelihood fit could then be applied to data and used to extract the number of signal events contained in the dataset.

This analysis used the full Runs 1 - 4 *BABAR* dataset, with some cross-checks performed on the Runs 1 - 2 dataset. The number of $B\bar{B}$ pairs and corresponding luminosity for each run is summarised in Table 7.1. All expected yields calculated from Monte Carlo simulation have been normalised to this data sample.

Branching fractions were calculated from the signal yield obtained from the

Run number	Number of BB pairs $\times 10^6$	Luminosity (fb^{-1})
Run 1	21.1 ± 0.2	19.2
Run 2	65.9 ± 0.7	59.9
Run 3	30.1 ± 0.4	27.4
Run 4	105.3 ± 1.0	95.7
Total: Runs 1 - 2 dataset	87.0 ± 1.0	79.1
Total: Runs 1 - 4 dataset	222.4 ± 2.3	202.2

Table 7.1: The B counting and luminosity of the Runs 1 - 4 on-peak data used in this analysis.

likelihood fit to the data using Equation 6.7 rearranged in the form:

$$BF = \frac{\text{yield}}{\text{efficiency} \times \text{n}B\bar{B}\text{ pairs}} \ . \tag{7.1}$$

The selection efficiencies are described in Chapter 5 and summarised in Table 5.4 for the $b \to s\gamma$ decays and Table 5.5 for the $b \to d\gamma$ decays.

7.2 $B \to K^*\gamma$ cross-check

The $B \to K^*\gamma$ decay has been well studied in both the *BABAR* and Belle experiments and its branching fraction is known to a good precision. For this reason, the low mass (0.6 - 1.0 GeV/c^2) region of the $b \to s\gamma$ hadronic system, which contains the $B \to K^*\gamma$ resonance, was used as a control region to verify the fit technique and efficiency calculations. Figure 7.1 shows the hadronic mass spectrum measured in the recent *BABAR* $b \to s\gamma$ analysis [3], showing the K^* resonance peak at low hadronic mass. Non-resonant $b \to s\gamma$ contributions in this area are small and were treated as $b \to s\gamma$ cross-feed.

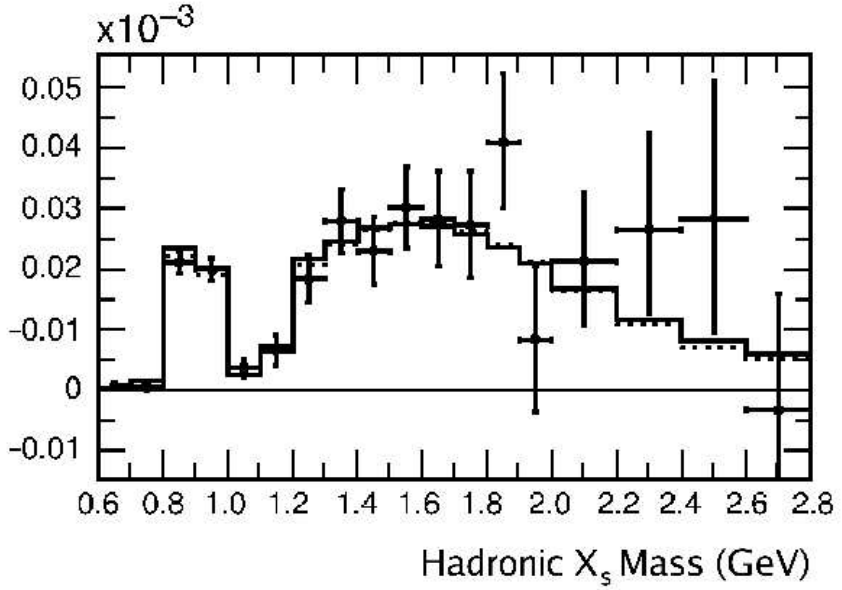

Figure 7.1: $b \to s\gamma$ hadronic mass spectrum taken from the recent *BABAR* analysis [3]. Data points are shown with the theoretical predictions (histogram).

Decay Mode	*BABAR* Result ($\times 10^{-5}$)	World Average ($\times 10^{-5}$)
$B^0 \to K^{*0}(K^{*0} \to K^+\pi^-)\gamma$	3.92 ± 0.20	
$B^0 \to K^{*0}(K^{*0} \to K^0_S\pi^0)\gamma$	4.02 ± 0.99	
Combined $B^0 \to K^{*0}\gamma$	3.92 ± 0.20	4.01 ± 0.20
$B^+ \to K^{*+}(K^{*+} \to K^+\pi^0)\gamma$	4.90 ± 0.45	
$B^+ \to K^{*+}(K^{*+} \to K^0_S\pi^+)\gamma$	3.52 ± 0.35	
Combined $B^+ \to K^{*+}\gamma$	3.87 ± 0.28	4.03 ± 0.26
Total $B \to K^*\gamma$	3.97 ± 0.34	4.02±0.33
Direct A_{CP}	-0.012 ± 0.036	-0.01±0.03

Table 7.2: Results from the recent $B \to K^*\gamma$ *BABAR* analysis [34] and the world average [1]. Statistical error only.

As K^0_S is not explicitly reconstructed, only the exclusive decay modes $B^0 \to K^{*0}(K^{*0} \to K^+\pi^-)\gamma$ and $B^+ \to K^{*+}(K^{*+} \to K^+\pi^0)\gamma$ were used in the cross-check. Exactly the same fit technique was used as that described in Chapter 6 for the $b \to s\gamma$ Monte Carlo sample. The ratio of signal to combined signal plus cross-feed in this sample was 0.815 and was fixed throughout the likelihood fit. The error on the signal yield was taken as the percentage uncertainty on the combined signal plus cross-feed yield.

The analysis of the K^* region was performed in several stages. The Runs 1 - 2 dataset was fitted first and the branching fraction obtained. This could then be compared to the branching fraction given by the likelihood fit to the full Runs 1 - 4 dataset. The full sample was also split into charged and neutral modes and the individual exclusive branching fractions compared to those found in [34]. A measurement of direct *CP* violation in the K^* system was made by splitting the sample into decays containing K^+ and decays containing K^-.

7.2.1 $B \to K^*\gamma$ - Runs 1 - 2 results

The expected yield for the Runs 1 - 2 dataset of 87.0 million $B\bar{B}$ pairs is shown in column 2 of Table 7.3. Yields were calculated using Equation 6.7, with the selection efficiencies obtained from Monte Carlo simulation (as described in Chapter 5) and the expected branching fraction taken from the experimental world average

Candidate Hypothesis	Expected yield	Fit result
Signal	286	
Cross-feed	65	
Signal + cross-feed	351	340± 23
Generic B	26	*fixed*
Continuum	382	318 ± 63
Branching Fraction	$(4.02 \pm 0.33) \times 10^{-5}$	$(3.70 \pm 0.25) \times 10^{-5}$

Table 7.3: The expected yield and fit results for the K^* control region for the Runs 1 - 2 dataset of 87.0×10^6 $B\bar{B}$ pairs. The expected yields are estimated from Monte Carlo trial fits, with the experimental world average as the expected BF. Statistical error only. The ratio of $N_{Sig}/(N_{Sig} + N_{X-Feed})$ is fixed at 0.815.

for the total $B \to K^*\gamma$ decay [1].

The fit to data is shown in projection plots superimposed on histograms of the data, with cuts applied to the variables not plotted. Figure 7.2 shows the ΔE^* projection with $5.274\,\mathrm{GeV}/c^2 < m_{\mathrm{ES}} < 5.286\,\mathrm{GeV}/c^2$ and Figure 7.3 shows the m_{ES} projection with $-0.15\,\mathrm{GeV} < \Delta\mathrm{E}^* < 0.10\,\mathrm{GeV}$. The same plots without the cuts on ΔE^* and m_{ES} are given in Appendix A. The fitted yields from Runs 1 - 2 data are shown in column 3 of Table 7.3.

The extracted branching fraction of $(3.70 \pm 0.25) \times 10^{-5}$ is in agreement with the expected value of $(4.02 \pm 0.33) \times 10^{-5}$, although somewhat lower. It is also in agreement, within statistical errors, with the results found by the *BABAR* Runs 1 - 2 analysis [34], which measured $BF(B \to K^*\gamma) = (4.22 \pm 0.30) \times 10^{-5}$ in these two decay modes.

Although this analysis used the same dataset as the *BABAR* dedicated exclusive analysis [34] to measure the branching fraction, the analysis methods are significantly different. The techniques used to optimise selection cuts and minimise backgrounds, together with the different likelihood fits used in each analysis, mean that the overlap between signal events in each study is not complete but it is significant. The different statistical errors in each analysis, as well as the different central values of branching fraction, is indicative of an underlying systematic difference between the two analyses but it is beyond the scope of this thesis to

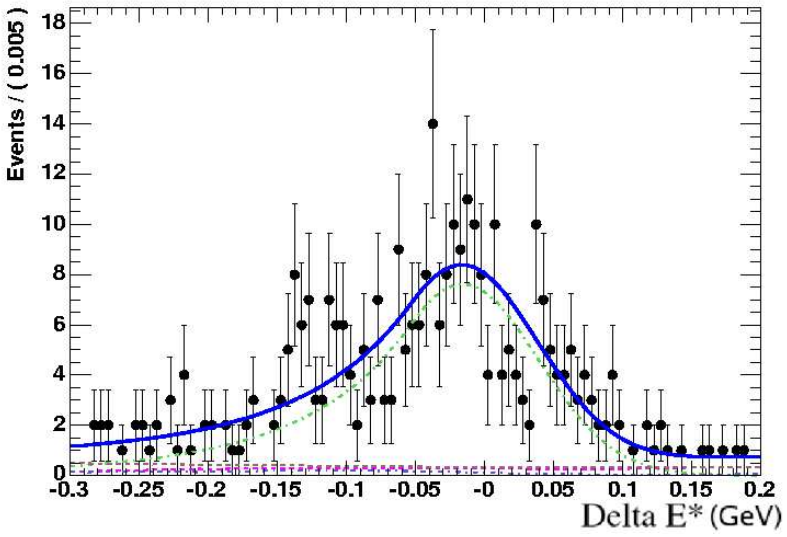

Figure 7.2: ΔE^* distribution in data for the K^* control region for the Runs 1 - 2 dataset, with the cut $5.274\,\mathrm{GeV}/c^2 < m_{\mathrm{ES}} < 5.286\,\mathrm{GeV}/c^2$ applied. Signal is shown in green, $b \to s\gamma$ cross-feed in pink, generic B background in blue and continuum background in brown.

investigate the cause in detail.

7.2.2 $B \to K^*\gamma$ - Full dataset results

The next stage in the cross-check is to look at the K^* region in the full Runs 1 - 4 dataset. The expected yields are shown in column 2 of Table 7.4 and the results of the maximum likelihood fit are summarised in column 3. The fits to data in the ΔE^* and m_{ES} distributions are shown in Section A.1 of Appendix A.

The total branching fraction found was $(3.74 \pm 0.16) \times 10^{-5}$, compared with the expected value of $(4.02 \pm 0.33) \times 10^{-5}$ for the world average and $BF(B \to K^*\gamma) = (4.22 \pm 0.30) \times 10^{-5}$ measured by the *BABAR* analysis [34] in these two decay modes. The measured branching fraction is within 1 σ of the world average and is in excellent agreement with the branching fraction of $(3.70 \pm 0.25) \times 10^{-5}$ measured in this analysis with the Runs 1 - 2 dataset. There is no published result for the full *BABAR* Runs 1 - 4 dataset at this time, so no direct comparison can be made between this result and other analyses performed at *BABAR*. It is,

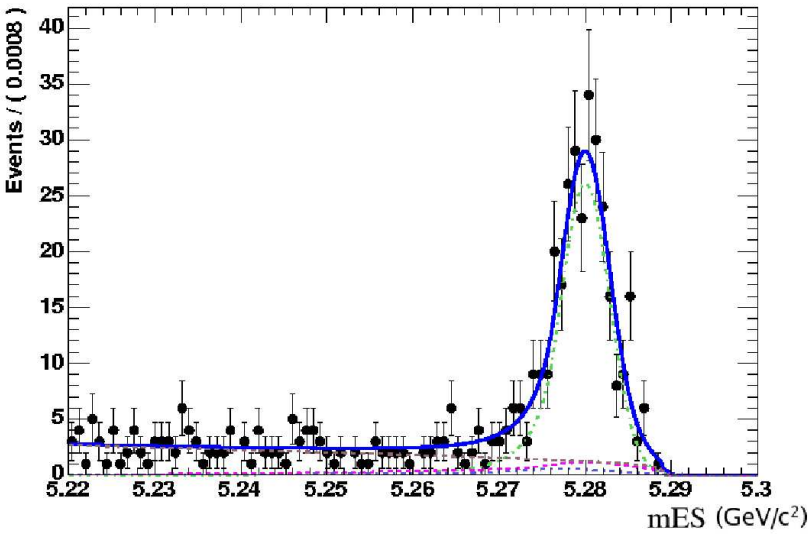

Figure 7.3: $m_{\rm ES}$ distribution in data for the K^* control region for the Runs 1 - 2 dataset, with the cut $-0.15\,\text{GeV} < \Delta\text{E}^* < 0.10\,\text{GeV}$ applied. Signal is shown in green, $b \to s\gamma$ cross-feed in pink, generic B background in blue and continuum background in brown.

however, consistent with the measurement of the Runs 1 - 2 published analysis.

7.2.3 Separating charged and neutral exclusive K^* decays

To further check agreement between this analysis and published data, the $B \to K^*\gamma$ full data sample was split into the charged and neutral component modes, $B^0 \to K^{*0}(K^{*0} \to K^+\pi^+)\gamma$ and $B^+ \to K^{*+}(K^{*+} \to K^+\pi^0)\gamma$ and fitted separately to extract the branching fraction for each. The results and comparison to [34] are given in Table 7.5. The fits to data in the ΔE^* and $m_{\rm ES}$ distributions are shown in Section A.1 of Appendix A.

The measured branching fractions of $(3.52 \pm 0.18) \times 10^{-5}$ for the $B^0 \to K^{*0}(K^{*0} \to K^+\pi^-)\gamma$ decay and $(4.44 \pm 0.43) \times 10^{-5}$ for the $B^+ \to K^{*+}(K^{*+} \to K^+\pi^0)\gamma$ decay are in agreement with the results found in previous analyses (see Table 7.2) within statistical errors. Both results are lower than expected but not significantly lower, which has been the case throughout the measurements made in the $B \to K^*\gamma$ cross-check as discussed in Section 7.2.1.

Candidate Hypothesis	Expected yield	Fit result
Signal	767	
$b \to s\gamma$ cross-feed	175	
Signal+cross-feed	942	876 ± 40
Generic B	70	*fixed*
Continuum	1026	857 ± 63
Branching Fraction	$(4.02 \pm 0.33) \times 10^{-5}$	$(3.74 \pm 0.16) \times 10^{-5}$

Table 7.4: The expected yield and fit results for full dataset in the K^* control region. The expected yields are estimated from Monte Carlo trial fits, with the experimental world average as the expected BF. Statistical error only. The ratio of $N_{Sig}/(N_{Sig} + N_{X-Feed})$ is fixed at 0.815.

Mode	Fit result ($\times 10^{-5}$)	*BABAR* result [34] ($\times 10^{-5}$)
$B^0 \to K^{*0}(K^{*0} \to K^+\pi^-)\gamma$	3.52 ± 0.18	3.92 ± 0.20
$B^+ \to K^{*+}(K^{*+} \to K^+\pi^0)\gamma$	4.44 ± 0.43	4.90 ± 0.45

Table 7.5: The extracted BFs, with statistical error, for the individual $B \to K^*\gamma$ decay modes.

7.2.4 A_{CP} in $B \to K^*\gamma$

The direct *CP* asymmetry in the K^* system was measured by separating the charged kaon daughters into K^+ and K^- samples. As described in Section 2.4.5, direct *CP* asymmetry can be simply calculated from the yields n of each sample using the formula:

$$A_{CP} = \frac{n(K^+) - n(K^-)}{n(K^+) + n(K^-)} \tag{7.2}$$

In the likelihood fit, the samples were fitted together to ascertain the values of the various shape parameters to be fixed (see Table 6.3 for details). The samples were then separated according to charge and fitted again, with the continuum and generic B backgrounds assumed to be equal in quantity in both samples. The yields from this second likelihood fit are given in Table 7.6 and the corresponding direct *CP* asymmetry in Table 7.7. It should be noted that the yields shown are the sum of signal and cross-feed, but the direct *CP* asymmetry is calculated using the signal yield only.

The result obtained in this analysis of $A_{CP} = -0.079 \pm 0.036$ is consistent

Mode	Expected yield	Signal yield
$B \to K^*\gamma$ with K^+	471	423.3 ± 28.0
$B \to K^*\gamma$ with K^-	480	363.7 ± 22.7

Table 7.6: The expected and extracted yields for $B \to K^*\gamma$ decays, separated into K^+ and K^- samples. Statistical error only. Yields given are the sum of signal plus cross-feed components, with the ratio $N_{Sig}/(N_{Sig} + N_{X-Feed}) = 0.82$.

	This analysis	*BABAR* [34]	World Average [29]
A_{CP}	-0.079 ± 0.036	-0.012 ± 0.036	-0.01 ± 0.07

Table 7.7: Direct *CP* asymmetry measurements, with statistical error, for the $B \to K^*\gamma$ data sample.

with both the previous *BABAR* results [34] and the experimental world average of direct *CP* violation in the $B \to K^*\gamma$ system [29]. It is also consistent with the Standard Model prediction of 1%.

7.3 $b \to s\gamma$ cross-check

Having validated the analysis method and fit technique with the K^* region control sample, the high hadronic mass $b \to s\gamma$ region of 1.0 GeV/c^2- 1.8 GeV/c^2 was studied. Again, this was done in two stages - first the *BABAR* Runs 1 - 2 dataset was analysed, then the full Runs 1 - 4 dataset. This provided another level of validation, as the Runs 1 - 2 results could be compared to the published branching fraction measurement from *BABAR* [3] using Runs 1 - 2 data. The *BABAR* results are summarised in column 2 of Table 7.8 and the world average in column 3.

This analysis measured the partial branching fraction of the $b \to s\gamma$ inclusive decay in the hadronic mass range 1.0 GeV/c^2- 1.8 GeV/c^2. As such, it cannot be compared directly to the published *BABAR* $b \to s\gamma$ results which cover a larger mass range of 0.6 GeV/c^2- 2.8 GeV/c^2. The quoted world average is for the inclusive $b \to s\gamma$ decay with a cutoff on the photon energy $E_\gamma > 1.6$ GeV. For true comparison, the partial branching fractions measured here should be extrapolated to high mass using a fit to the photon energy spectrum with the assumption that

	BABAR Result ($\times 10^{-4}$)	World Average ($\times 10^{-4}$)
$b \to s\gamma$	3.41 ± 0.18	3.55 ± 0.24

Table 7.8: Branching fractions measurements from the latest $b \to s\gamma$ *BABAR* analysis [3] and the world average [1]. Statistical error only.

the model used to generate the simulation is correct. This introduces a model-dependent error which arises from the uncertainty on the mass of the b-quark of $\pm 50\,\mathrm{MeV}$which is larger than the statistical error of the measurement. For this reason, the extrapolated branching fraction is not quoted and the comparison with previously published results is not expected to be exact. This analysis used the same model as the previous *BABAR* analysis described in [3] and the similarities in results between the two give an indication of the accuracy of the model.

In the ratio of branching fractions $\frac{b\to d\gamma}{b\to s\gamma}$, this extrapolation is irrelevant as both samples use the same hadronic mass range.

Throughout the likelihood fits to data, the extracted yield is the sum of signal plus $b \to s\gamma$ cross-feed. The ratio of signal to signal and cross-feed combined is fixed throughout to 0.385.

7.3.1 $b \to s\gamma$ - Runs 1 - 2 results

The expected yields for $b \to s\gamma$ in the Runs 1 - 2 dataset are shown in Table 7.9. Yields were calculated as before, using Equation 6.7 with the selection efficiencies obtained from Monte Carlo simulation (as described in Chapter 5) and the expected branching fraction taken from the experimental world average for the total $b \to s\gamma$ decay [1].

The fits to data are shown as histograms of data points overlaid with PDF projections in Figures A.24 for m_{ES} and A.23 for ΔE^*in Section A.2 of Appendix A. The extracted branching fraction of $(3.94 \pm 0.31) \times 10^{-5}$ is slightly higher than either the recent *BABAR* result or the world average, but agrees within statistical error.

Candidate Hypothesis	Expected yield	Fit result
Signal	336	
$b \to s\gamma$ cross-feed	536	
Signal+cross-feed	872	1034 ± 80
Generic B	734	*fixed*
Continuum	4813	5602 ± 63
Branching Fraction	3.41×10^{-4}	$(3.94 \pm 0.31) \times 10^{-4}$

Table 7.9: The expected yield and fit results for the $b \to s\gamma$ region for the Runs 1 - 2 dataset of 87.0×10^6 $B\bar{B}$ pairs. Statistical error only. The ratio of $N_{Sig}/(N_{Sig} + N_{X-feed})$ is fixed to 0.385.

Candidate Hypothesis	Expected yield	Fit result
Signal	902	
$b \to s\gamma$ cross-feed	1436	
Signal+cross-feed	2338	2427 ± 123
Generic B	1968	*fixed*
Continuum	12912	15330 ± 172
Branching Fraction	3.41×10^{-4}	$(3.54 \pm 0.19) \times 10^{-4}$

Table 7.10: The expected yield and fit results for the $b \to s\gamma$ region for the Runs 1 - 4 dataset of 220×10^6 $B\bar{B}$ pairs. Statistical error only. The ratio of $N_{Sig}/(N_{Sig} + N_{X-feed})$ to 0.385.

7.3.2 $b \to s\gamma$ - Runs 1 - 4 results

The expected yields for the $b \to s\gamma$ sample, scaled to the full Runs 1 - 4 *BABAR* dataset, are shown in Table 7.10 together with the fit results from data. The projection plots of the different fit components superimposed on the histogram of data points is shown for $m_{\rm ES}$ in Figure 7.5 and for ΔE^* in Figure 7.4, with cuts applied to the variable not plotted.

The branching fraction of $(3.54 \pm 0.19) \times 10^{-4}$ extracted in this fit is again higher than the expected branching fraction taken from the previous *BABAR* Runs 1 - 2 analysis, but is in excellent agreement with the world average of $(3.55 \pm 0.24) \times 10^{-4}$. The result agrees within error with the Runs 1 - 2 measurement given in Section 7.3.1.

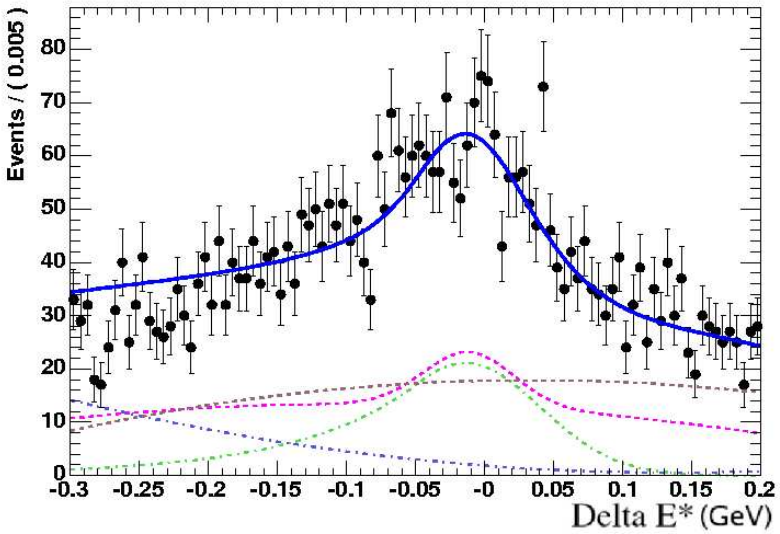

Figure 7.4: ΔE^* distribution in data for $b \to s\gamma$ for the full *BABAR* dataset of 222×10^6 $B\bar{B}$ pairs, with the cut $5.274\,\mathrm{GeV}/c^2 < m_{\mathrm{ES}} < 5.286\,\mathrm{GeV}/c^2$ applied. Signal is shown in green, $b \to s\gamma$ cross-feed in pink, generic B background in blue and continuum background in brown.

Mode	Expected yield	Fitted yield
$b \to s\gamma$ with K^+	1306	1527 ± 82
$b \to s\gamma$ with K^-	1292	1408 ± 87

Table 7.11: The expected and extracted yields for $b \to s\gamma$ decays, separated into K^+ and K^- samples. Statistical error only. Yields given are the sum of signal plus cross-feed components, with the ratio $N_{Sig}/(N_{Sig} + N_{X-Feed}) = 0.385$.

7.3.3 A_{CP} in $b \to s\gamma$

The direct *CP* asymmetry in the $b \to s\gamma$ system was measured using the same method used to measure A_{CP} in the $B \to K^*\gamma$ system. Decays were separated into those containing K^+s and those containing K^-s. The yields from the likelihood fits are given in Table 7.11 and the corresponding direct *CP* asymmetry in Table 7.12. It should be noted that the yields shown are the sum of signal and cross-feed, but the direct *CP* asymmetry is calculated using the signal yield only.

The result obtained in this analysis of $A_{CP} = 0.040 \pm 0.035$ is consistent with both the previous *BABAR* results and the experimental world average of direct *CP*

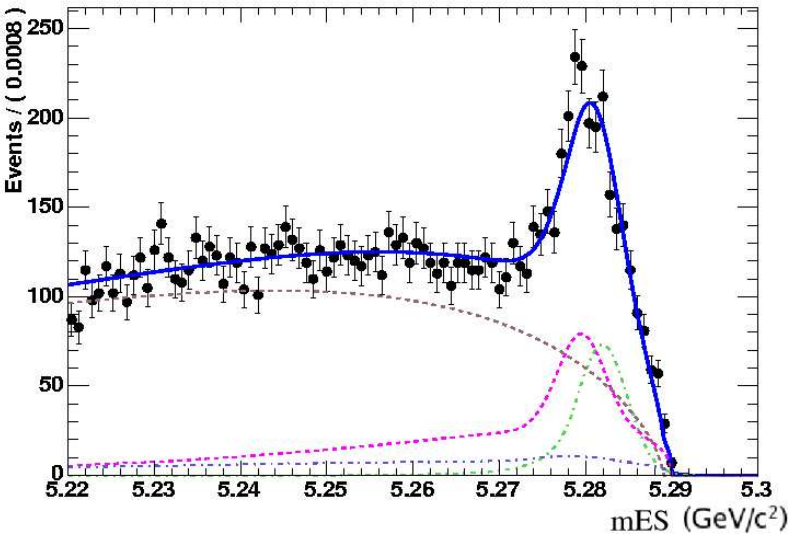

Figure 7.5: $m_{\rm ES}$ distribution in data for $b \to s\gamma$ for the full *BABAR* dataset of $222{\times}10^6$ $B\bar{B}$ pairs, with the cut $-0.15\,\text{GeV} < \Delta\text{E}^* < 0.10\,\text{GeV}$ applied. Signal is shown in green, $b \to s\gamma$ cross-feed in pink, generic B background in blue and continuum background in brown.

	This analysis	*BABAR* Result [23]	World Average [1]
A_{CP}	0.040 ± 0.035	0.025 ± 0.050	0.004 ± 0.037

Table 7.12: Direct *CP* asymmetry measurements, with statistical error, for the $b \to s\gamma$ data sample.

violation in the $b \to s\gamma$ system. It is also consistent with the theoretical Standard Model prediction of 1%.

Candidate Hypothesis	Expected yield	Fit result
Signal	26	39.0 ± 15.8
$b \to s\gamma$ cross-feed	266	*fixed*
Generic B	174	*fixed*
Continuum	2038	1876 ± 49
Branching Fraction	0.96×10^{-6}	$(1.46\pm0.59) \times10^{-6}$

Table 7.13: The expected yield and fit results for the $B \to (\rho,\omega)\gamma$ sample, for the Runs 1 - 4 dataset of 222×10^6 $B\bar{B}$ pairs. Statistical error only.

	This Analysis ($\times10^{-6}$)	*BABAR* ($\times10^{-6}$)	Belle ($\times10^{-6}$)	World Average ($\times10^{-6}$)
Combined $B \to (\rho,\omega)\gamma$	1.46 ± 0.59	0.6 ± 0.3	$1.34^{+0.34}_{-0.31}$	0.96 ± 0.23

Table 7.14: Branching fraction measurements from the latest $B \to (\rho,\omega)\gamma$ *BABAR* and BELLE analyses [22, 21] and the world average [1]. Statistical error only.

7.4 $B \to (\rho,\omega)\gamma$ cross-check

The next stage in the analysis was to examine the low-mass $b \to d\gamma$ region, which contains the $B \to (\rho,\omega)\gamma$ exclusive decays. The method described in Chapter 6 to fit $b \to d\gamma$ was used to fit this sample. The yields from the likelihood fit are given in Table 7.13, calculated as before using Equation 6.7 taking the world average [1] as the expected branching fraction and using an estimate of the signal efficiency. The branching fraction extracted from these results is shown in Table 7.14, together with the value measured by recent analyses and the world average for comparison.

Figures 7.7 and 7.6 show the projections of fits to the ΔE^* and $m_{\rm ES}$ distributions superimposed upon histograms of data points. Cuts are applied on the variable not plotted, as previously described. Full distributions without cuts can be seen in Section A.3 of Appendix A.

This measured branching fraction of $(1.46 \pm 0.59) \times 10^{-6}$ is somewhat higher than the recent *BABAR* published result and world average but agrees with both within errors. It is also in very good agreement with the BELLE result and all measurements to date are consistent with the Standard Model predictions

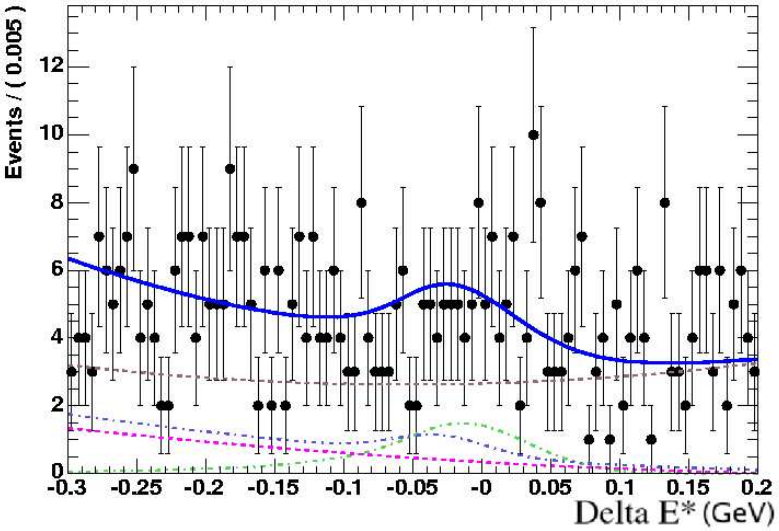

Figure 7.6: ΔE^* distribution in data for $B \to (\rho, \omega)\gamma$ for the full *BABAR* dataset of 222×10^6 $B\bar{B}$ pairs, with the cut $5.274\,\mathrm{GeV}/c^2 < m_{\mathrm{ES}} < 5.286\,\mathrm{GeV}/c^2$ applied. Signal is shown in green, $b \to s\gamma$ cross-feed in pink, generic B background in blue and continuum background in brown.

described in Section 2.5.3.

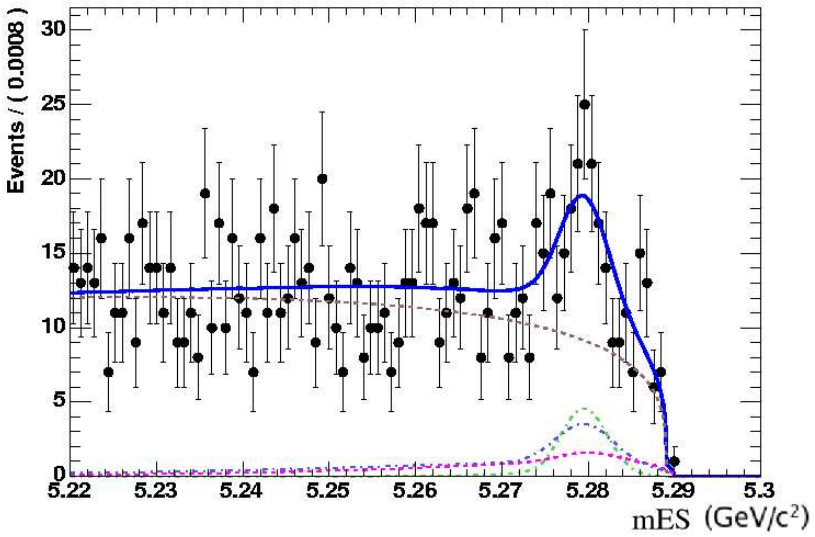

Figure 7.7: $m_{\rm ES}$ distribution in data for $B \to (\rho, \omega)\gamma$ for the full *BABAR* dataset of 222×10^6 $B\bar{B}$ pairs, with the cut $-0.15\,\text{GeV} < \Delta\text{E}^* < 0.10\,\text{GeV}$ applied. Signal is shown in green, $b \to s\gamma$ cross-feed in pink, generic B background in blue and continuum background in brown.

Candidate Hypothesis	Expected yield	Fit result
Signal	38	96 ± 28
$b \to s\gamma$ cross-feed	334	*fixed*
Generic B	752	*fixed*
Continuum	9684	8484 ± 28
Branching Fraction	1×10^{-5}	(2.47±0.72) $\times10^{-5}$

Table 7.15: The expected yield and fit results for the $b \to d\gamma$ region for the Runs 1 - 4 dataset of 222×10^6 $B\bar{B}$ pairs. Statistical error only.

7.5 $b \to d\gamma$

Finally, after the control samples had been measured and no problems with analysis technique uncovered, the $b \to d\gamma$ sample in the mass range 1.0 GeV/c^2 - 1.8 GeV/c^2 could be fitted. The results of the likelihood fit are shown in Table 7.15. The expected yield for signal is calculated based on an assumed branching fraction of 1×10^{-5}, as no measurement or predictions exist at present. Generic B contains the $b \to d\gamma$ self-cross feed, which comprises 76 expected events out of the total 752.

Figures 7.9 and 7.8 show the projections of fits to the ΔE^* and $m_{\rm ES}$ distributions in data, superimposed upon histograms of data points. Cuts are applied on the variable not plotted, as previously described. Full distributions without cuts can be seen in section A.4 of Appendix A.

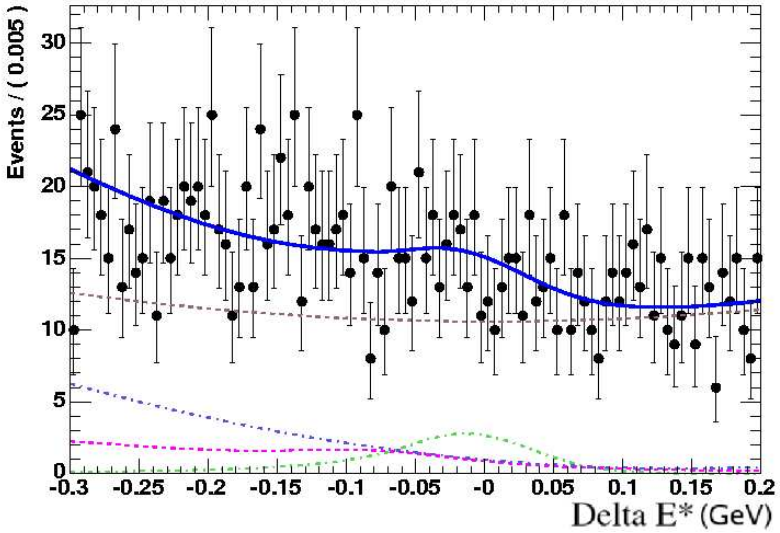

Figure 7.8: ΔE^* distribution in data for $b \to d\gamma$ for the full *BABAR* dataset of $222{\times}10^6$ $B\bar{B}$ pairs, with the cut $5.274\,\mathrm{GeV}/c^2 < m_{\mathrm{ES}} < 5.286\,\mathrm{GeV}/c^2$ applied. Signal is shown in green, $b \to s\gamma$ cross-feed in pink, generic B background in blue and continuum background in brown.

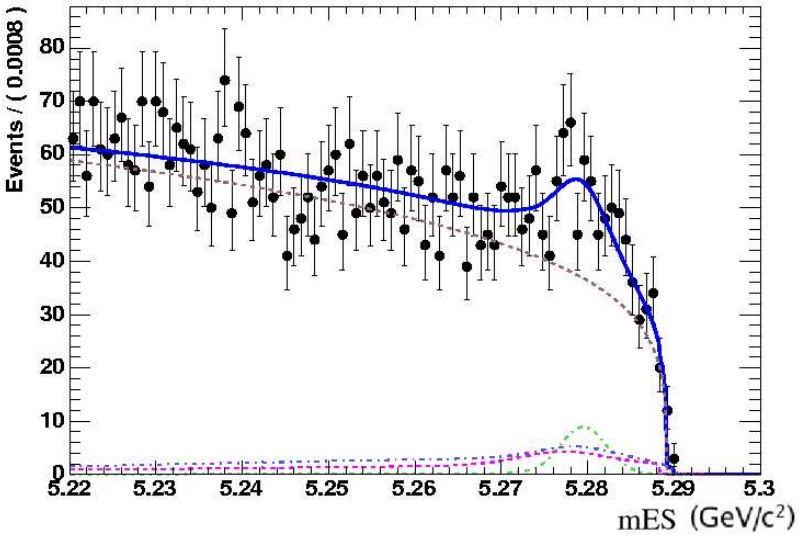

Figure 7.9: m_{ES} distribution in data for $b \to d\gamma$ for the full *BABAR* dataset of $222{\times}10^6$ $B\bar{B}$ pairs, with the cut $-0.15\,\mathrm{GeV} < \Delta\mathrm{E}^* < 0.10\,\mathrm{GeV}$ applied. Signal is shown in green, $b \to s\gamma$ cross-feed in pink, generic B background in blue and continuum background in brown.

7.6 Systematic errors

A great deal of effort goes into ensuring *BABAR* Monte Carlo simulation data models the experiment accurately, but some differences between simulation and data persist. Each of these deviations of Monte Carlo from real data introduces error in the measurement of the branching fraction. Rather than statistical fluctuations of the measurement about the true value, these are systematic errors tending to shift the mean of the measurement away from the true value in a specific direction.

As the ratio of branching fractions is measured in this analysis in order to extract $|\frac{V_{td}}{V_{ts}}|$, nearly all systematic errors due to selection efficiencies drop out in the final measurement. The only one that remains is the PID cut, as the pion selection and kaon rejection have different errors that do not cancel. Other systematic errors are described in this section, but no detailed analysis of them is necessary at this stage. Those that do not cancel in the ratio are small compared to the large statistical error.

7.6.1 B counting

The determination of the number of $\Upsilon(4S) \to B\bar{B}$ in *BABAR* data is described fully in [33]. The procedure gives a total of 222.4 ± 2.3 million $B\bar{B}$ pairs in the dataset used in this analysis. The error of 1.1% is multiplicative for each branching fraction measurement and as such drops out in the ratio of branching fractions.

7.6.2 Tracking efficiency

Studies made within the *BABAR* collaboration indicate that *BABAR* Monte Carlo overestimates the detection efficiency for charged particles, with the result that a downward correction must be made when applying this efficiency to real data. The efficiency correction is roughly 0.989 to be applied to each final state charged

track, with an estimated systematic uncertainty of 0.8%.

As both the $b \to s\gamma$ and $b \to d\gamma$ samples contain the same set of final states, this error drops out in the ratio of branching fraction.

7.6.3 π^0 and single photon efficiency

The data and Monte Carlo efficiencies of π^0s and photons are measured using a sample of π^0s from fully reconstructed $\tau^\pm$ decays. In general, Monte Carlo overestimates the efficiency with which π^0s are reconstructed. The correction factor to be applied is 0.971, with an associated 3% systematic error.

The efficiencies for the high energy B daughter photons do not differ significantly between data and Monte Carlo, so no correction is applied. A systematic error is assigned of 2.5%, which must be added linearly with the 3% π^0 error as the two are highly correclated.

Once again, these errors drop out in the ratio.

7.6.4 Systematic uncertainties in the π^0/η veto

The efficiencies of the π^0/η veto depend on the rest of the event (see Section 5.7.1 for a description of the rest of the event). A random calorimeter cluster generated by noise or machine backgrounds can accidentally combine with a true signal photon causing a failure of the veto, or indeed failure of the photon isolation cut. After calorimeter acceptance, this is the largest source of error for photon quality selection. An independent *BABAR* analysis indicated a discrepancy of 1% between data and Monte Carlo efficiencies for the π^0/η veto and a 2% discrepancy for the photon isolation cut. These differences are adopted as systematic errors in each decay mode and again drop out in the ratio measurement.

7.6.5 Neural Network systematic

Previous studies on the systematic errors from using neural networks assign an error of 3% to allow for differences between neural net discrimination in data and

Monte Carlo. As this drops out in the ratio measurement, no dedicated study was made of this error.

7.6.6 PID efficiency

There are small but measurable differences in the efficiency of PID selectors applied to Monte Carlo and real data. As different criteria are applied to pion and kaon selection, this is the only selection systematic error which does not cancel in the ratio of $\frac{BF(b\to d\gamma)}{BF(b\to s\gamma)}$. Significant work has already been carried out on data/simulation comparison for PID in the *BABAR* collaboration, comparing data and Monte Carlo control samples. For pion identification, a sample of charged pions from a so-called 'tau 3-1' decay is used, where one τ of a pair decays in a typical 1-prong mode (one charged particle plus a ν_τ) and the other in a rarer 3-prong mode (three charged tracks, nearly always pions, plus a ν_τ). This gives a very pure control sample of pions. Control samples of charged kaons (and pions) are obtained from D^* decays, with $D^{*+}\to D^0\pi^+$, $D^0\to\pi^+K^-$.

The ratio of data/simulation for the pion LH veryTight selector are shown for pion selections in Figure.7.10 and for kaon rejection in Figure.7.11.

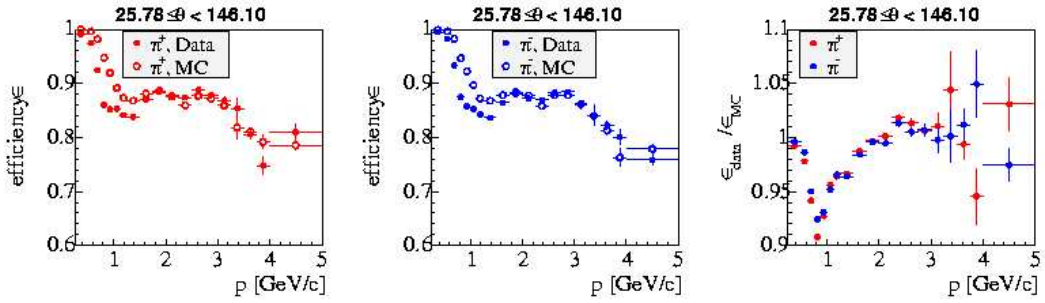

Figure 7.10: Data/Monte Carlo efficiency for pion selection in bins of polar angle.

PID studies indicate that Monte Carlo simulation underestimates the mis-identification rates. A conservative systematic error of 2% has been applied to pion identification and an error of 1% to kaon mis-identification.

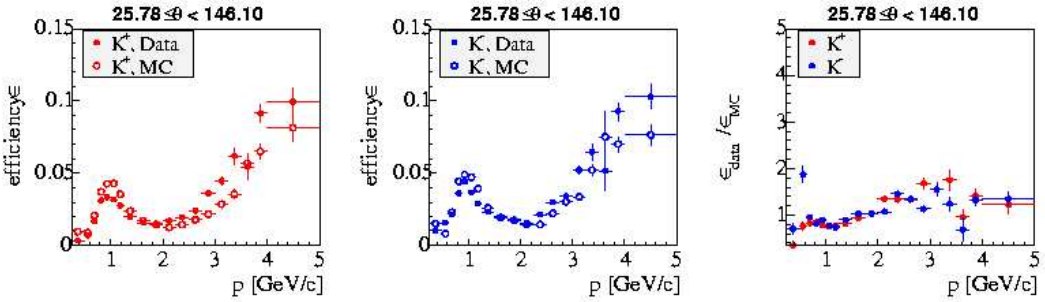

Figure 7.11: Data/Monte Carlo efficiency for kaon rejection in bins of polar angle.

7.6.7 Peaking background systematic

In the $B \to (\rho, \omega)\gamma$ and $b \to d\gamma$ measurements presented in this thesis, there is a significant background from mis-reconstructed B meson decays which peaks in ΔE^* and $m_{\rm ES}$. As described in Section 5.9, the peaking component stems mainly from $b \to d\pi^0$ and $b \to d\eta$ decays. These decays will eventually be studied and measured, but for now a systematic error arising from uncertainties in the amount of peaking background should be assigned.

The *BABAR* $B \to (\rho, \omega)\gamma$ analysis [22] carried out a detailed study of the peaking backgrounds in their data sample. The exclusive decays $B^+ \to \rho\pi^0/\eta$, $B^0 \to \rho^0\pi^0/\eta$ and $B^0 \to \omega\pi^0/\eta$ are the main contributors here and the branching fraction of each decay was varied by one standard deviation for a measured decay, or from zero to the upper limit for an unobserved decay. In that analysis a systematic error of $^{+4.1}_{-3.5}\%$ was assigned and this has been adopted for the $B \to (\rho, \omega)\gamma$ measurement made in this analysis.

A separate study was made in the $b \to d\gamma$ inclusive decay where the peaking component is smaller. As the inclusive decays $b \to d\pi^0$ and $b \to d\eta$ have not yet been measured, a more conservative approach must be taken. The peaking component of the generic B background was varied between zero and twice its predicted value. This gave an uncertainty on the signal yield of $\pm 13.2\%$, which has been taken as the systematic error.

7.6.8 Fit systematic errors

The efficiency systematic errors described above are all (with the exception of the PID systematic) associated with signal efficiency and as such are multiplicative and scale with signal yield. Fit systematics do not scale with signal yield and do not drop out in the measurement of the ratio of branching fractions. They arise from possible systematic deviations between the PDFs used in the likelihood fits and the true distributions in data. The uncertainties in signal yield associated with these effects are evaluated only after the likelihood fit has been applied to data.

Every parameter that is fixed in the likelihood fit is a possible source of error. Therefore, each fixed parameter was varied within limits ($\pm 1\sigma$) and its effect on signal yield determined by performing a new likelihood fit. The percentage change in yield for each shape parameter is shown in Table 7.16 for the $b \to s\gamma$ sample and Table 7.17 for the $b \to d\gamma$ sample. By far the dominant uncertainty in the $b \to s\gamma$ fit was the fixing of the ratio of signal to cross-feed. Varying any other parameter changes little in the likelihood yield. The $b \to d\gamma$ fit has many sources of systematic uncertainty, the most significant being the fixing of the signal shape and fixing the number of expected generic B and $b \to s\gamma$ cross-feed events. However, as the $b \to d\gamma$ signal shape was fixed using the the $b \to s\gamma$ signal shape, these errors cancel in the ratio of branching fractions. The total percentage deviation has been adopted as an additive systematic error on the fit yield.

An additional check of the yield systematic was performed after the data sample had been fitted. The yields found in the fit to data were used as inputs to toy studies of $b \to s\gamma$ and $b \to d\gamma$ Monte Carlo samples in place of the calculated expected yields (shown in Table 6.4). The ΔE^* and $m_{\rm ES}$ distributions were fitted in the same process as described in Section 6.3.1. The pulls for floating parameters were examined and are summarised in Table 7.18 for the $b \to s\gamma$ sample and 7.19

Variable	Change in yield with variation of + 1σ (%)	Change in yield with variation of -1σ (%)
Ratio Sig/XF	9.4	8.2
nBB	0.81	0.81
ΔE^* fit variables		
Signal α	0.93	1.00
Signal n	0.18	4.5
Signal σ	1.2	1.3
Cross-feed μ	0.065	0.18
Cross-feed σ	0.58	0.18
Cross-feed $P01$	0.23	0.26
Cross-feed $P02$	0.30	0.28
Generic B μ	0.0	0.0
Generic B σ	0.0	0.0
Generic B $P01$	0.015	0.0042
Generic B $P02$	0.003	0.015
$m_{\rm ES}$ fit variables		
Signal α	1.5	1.7
Signal n	0.15	0.16
Signal σ	0.55	0.74
Cross-feed μ	0.0	0.0
Cross-feed σ	1.3	1.2
Cross-feed m	1.8	2.0
Cross-feed c	0.71	0.81
Cross-feed p	0.42	2.0
Generic B μ	0.0	0.0
Generic B σ	0.19	0.27
Generic B m	1.0	2.0
Generic B c	0.29	0.23
Generic B p	0.32	0.81
Total	10.06	10.46

Table 7.16: Percentage effect on yield of likelihood fit to data of variations in fixed fit parameters in the $b \to s\gamma$ sample.

Variable	Change in yield with variation of + 1σ (%)	Change in yield with variation of -1σ (%)
nBB_{total}	4.2	3.8
$\mathrm{nBB}_{peaking}$	13.2	13.2
nXs	3.5	2.8
ΔE^* fit variables		
Signal μ	1.4	0.72
Signal α	1.5	1.4
Signal n	3.5	5.6
Signal σ	3.5	3.8
Cross-feed μ	0.14	2.1
Cross-feed σ	3.5	0.083
Cross-feed $P01$	0.3	0.021
Cross-feed $P02$	0.032	3.4
Generic B μ	0.025	0.013
Generic B σ	0.062	0.052
Generic B $P01$	0.067	0.034
Generic B $P02$	1.0	1.1
m_{ES} fit variables		
Signal μ	0.031	0.032
Signal α	0.15	0.094
Signal n	1.4	3.1
Signal σ	0.36	0.32
Cross-feed μ	0.32	0.32
Cross-feed σ	0.50	0.67
Cross-feed m	0.19	0.31
Cross-feed c	1.4	3.2
Cross-feed p	0.19	0.38
Generic B μ	2.4	2.6
Generic B σ	0.79	3.1
Generic B m	0.34	0.3
Generic B c	3.2	2.1
Generic B p	0.32	0.034
Total	9.67	11.37

Table 7.17: Percentage effect on yield of likelihood fit to data of variations in fixed fit parameters in the $b \to d\gamma$ sample.

	$N_{Sig+Xfeed}$	N_{Cont}	c	P01	P02
$b \to s\gamma$	0.19/1.01	-0.14/0.99	0.20/0.98	0.010/1.01	0.010

	$\mu m_{\rm ES}$	$\mu_{\Delta E^*}$
$b \to s\gamma$	-0.037/1.06	0.031/0.97

Table 7.18: Pull/RMS for those variables floated in the $b \to s\gamma$ pure toy fits, with the yields weighted to those found in data.

	N_{Sig}	N_{Cont}	c	P01	P02
$b \to d\gamma$	-0.059/1.04	-0.060/0.99	-0.011/0.98	-0.0031/1.03	-0.031/1.01

Table 7.19: Pull/RMS for those variables floated in the $b \to d\gamma$ pure toy fits, with the yields weighted to those found in data.

for the $b \to d\gamma$ sample. The pulls were found to be small for both the $b \to d\gamma$ sample and the $b \to s\gamma$ sample and comparable to those found in the toy studies described in Section 6.3.

7.6.9 Systematics in the measurement of A_{CP}

The measurement of direct *CP* violation in the $B \to K^*\gamma$ and $b \to s\gamma$ systems again benefits from the advantages of a ratio of yields. The majority of systematic errors cancel. Those that do not cancel are differing tracking and PID efficiencies for positively and negatively charged particles. There is also a systematic uncertainty stemming from the asymmetry of K^+ and K^- yield in the backgrounds. The recent *BABAR* $B \to K^*\gamma$ analysis [34] assigned a systematic error of 1.1% to the A_{CP} measurement, with the dominant contribution from the tracking and intrinsic detector asymmetries. This could be improved by examining more closely the *CP* asymmetry in the sideband region (with values of ΔE^* and $m_{\rm ES}$ outside the fit region used in this analysis). The increased dataset available today would certainly increase the power of such an analysis.

The recent *BABAR* $b \to s\gamma$ analysis [23] made a detailed analysis of asymmetries in the backgrounds and assigned a conservative error of 5% to account for these effects, which has been adopted in this analysis.

Analysis	Stat. Error	Sys. Error
$B \to K^*\gamma$ [34]	$\pm$ 5.1%	$\pm$ 6.1%
$B \to K^*\gamma$ This Analysis	$\pm$ 9.2%	$\pm$ 11%
A_{CP} in $B \to K^*\gamma$ [34]	$\pm$ 30%	$\pm$ 1.1%
A_{CP} in $B \to K^*\gamma$ This Analysis	$\pm$ 45%	$\pm$ 1.1%
$b \to s\gamma$ Semi-inclusive [3]	$\pm$ 5.5%	+17% -12%
$b \to s\gamma$ This analysis	$\pm$ 5.4%	$\pm$ 11%
A_{CP} in $b \to s\gamma$ [23]	$\pm$ 200%	$\pm$ 1.1%
A_{CP} in $b \to s\gamma$ This Analysis	$\pm$ 88%	$\pm$ 1.1%
$B \to (\rho, \omega)\gamma$ [22]	$\pm$ 50%	$\pm$ 16%
$B \to (\rho, \omega)\gamma$ This Analysis	$\pm$ 41%	+12% -13%
$b \to d\gamma$ This analysis	$\pm$ 29%	+17% -18%

Table 7.20: Statistical and systematic errors in previous *BABAR* Radiative Penguin analyses.

7.6.10 Summary of errors

The dominant errors for the cross-check measurements are the fit errors, while for the $b \to d\gamma$ analysis the fit and effects of peaking backgrounds are dominant. It is assumed here that all errors are uncorrelated. This is not actually the case, as some fit errors in particular are certainly correlated. However, the correlated errors are small compared to the dominant systematic errors and for the $b \to d\gamma$ measurements, small compared to the statistical error. For the purposes of this thesis a detailed study of the correlations between systematic errors is not necessary.

It is expected that the magnitude of the systematic errors for this analysis will be comparable to other recent radiative penguin results. For comparison, uncertainties for the recent *BABAR* $B \to (\rho, \omega)\gamma$ and $b \to s\gamma$ analyses are summarised in Table 7.20.

7.7 Limit setting

When searching for new processes, evidence for the decay requires a result of over 3σ significance and observation of the decay can be claimed at more than

5σ significance. In this section the significance of each result is assessed using a likelihood scan. The significance is taken as $\sqrt{-2\ln \mathfrak{L}_0/\mathfrak{L}_{max}}$, where $\mathfrak{L}_0$ is the value of the likelihood for the null signal hypothesis and $\mathfrak{L}_{max}$ the maximum likelihood returned by the fitting software, as described in Section 6.2.

A conservative approach has been taken with the presentation of results in this analysis, as the possible effects of the large signal-like generic B background in the $b \to d\gamma$ decay have not been studied in detail. A large systematic error has already been assigned to this background, but despite this upper and lower confidence limits are preferred even when the result has a significance of over 3σ. The central value and errors are given for all results, together with the 90% confidence level (CL) limits of the result, calculated using the formula:

$$BF^{90\%} = BF + (1.28 \times \sigma_{stat} \times BF) + (1.28 \times \sigma_{syst} \times BF) \qquad (7.3)$$

with BF representing the measured branching fraction (or measured $|\frac{V_{td}}{V_{ts}}|$) and σ the error. The 90% CL is the value of the branching fraction for which, were the measurement to be repeated independently several times, the true value of the branching fraction would be less than the estimated branching fraction in 90% of those measurements.

7.7.1 $b \to d\gamma$ branching fraction

Figure 7.12 shows the likelihood function with respect to the measured $b \to d\gamma$ branching fraction.

Using the formula described above, the significance of the result was found to be 3.1σ, constituting evidence for the $b \to d\gamma$ decay. The upper limit at 90% confidence level was calculated as 3.6×10^{-5} and lower limit 1.4×10^{-5}.

$$BF(b \to d\gamma) = (2.5 \pm 0.7(stat) \, ^{+0.42}_{-0.44}(syst)) \times 10^{-5}$$

$$1.4 \times 10^{-5} < BF(b \to d\gamma) < 3.6 \times 10^{-5} \quad (90\% \text{ CL})$$

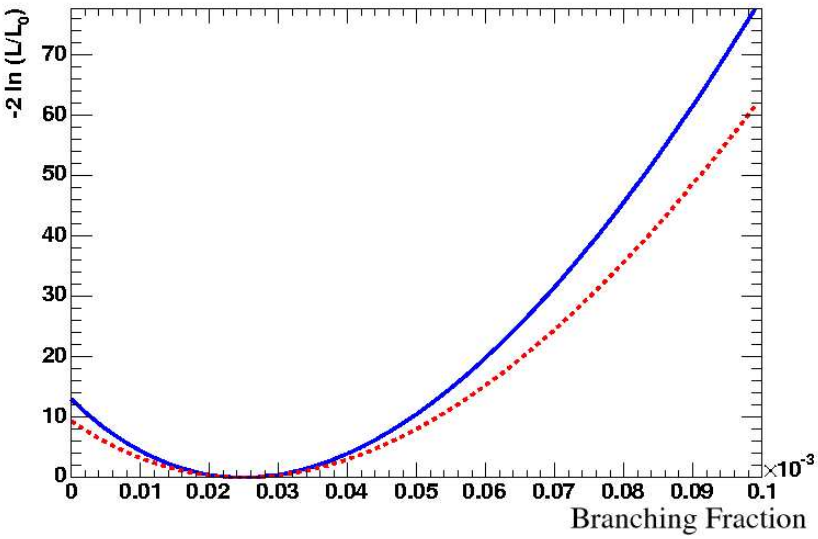

Figure 7.12: Likelihood scan of the fit to $b \to d\gamma$. The dashed curve includes the systematic error described in Section 7.6.10.

7.7.2 $|\frac{V_{td}}{V_{ts}}|$ from $\frac{b\to d\gamma}{b\to s\gamma}$

As described in Section 2.5.2, by measuring the ratio of branching fractions $\frac{b\to d\gamma}{b\to s\gamma}$ the ratio of CKM matrix elements $|\frac{V_{td}}{V_{ts}}|$ can be extracted.

In this analysis, a limit on $|\frac{V_{td}}{V_{ts}}|$ was set using the branching fractions $BF(b \to s\gamma) = (3.54 \pm 0.19(stat.) \pm 0.39(syst.)) \times 10^{-4}$ and $BF(b \to d\gamma) = (2.47 \pm 0.72(stat.)\ ^{+0.42}_{-0.44}(syst.)) \times 10^{-5}$, and using the same calculation and theoretical constants used in the exclusive analysis [22],

$$\frac{BF(B \to (\rho,\omega)\gamma)}{BF(B \to K^*\gamma)} = |\frac{V_{td}}{V_{ts}}|^2 \left(\frac{1 - m^2_{\rho,\omega}/M^2_B}{1 - m^2_{K^*}/M^2_B}\right)^3 \zeta^2[1 + \Delta R]. \tag{7.4}$$

Taking the mass term to be one for the inclusive measurement and using $\zeta = 0.85 \pm 0.10$ and $\Delta R = 0.10 \pm 0.10$ [19],

$$\frac{b \to d\gamma}{b \to s\gamma} = 0.0698 \pm 0.021(stat.) \pm 0.012(syst.) \pm 0.011(theo.)$$

$$|\frac{V_{td}}{V_{ts}}| = 0.30 \pm 0.09(stat.) \pm 0.05(syst.) \pm 0.04(theo.)$$

The (*theo.*) uncertainty arises from the error in theoretical parameters ζ and ΔR. Upper and lower limits at 90% confidence level were set using the method outlined above:

$$0.17 < |\frac{V_{td}}{V_{ts}}| < 0.43 \ \ (90\% \text{ CL}).$$

Clearly, this is an approximate measurement as the inclusive decays do not have the same theoretical constants as the exclusive decays and this should be considered when comparing the result to published measurements. The central value is higher than the recent measurement by CDF of $|\frac{V_{td}}{V_{ts}}| = 0.208^{+0.008}_{-0.007}$ [27], but the two agree within error limits. This result also agrees with the Belle measurement of $|\frac{V_{td}}{V_{ts}}|=0.200^{+0.026}_{-0.025}(exp.)^{+0.038}_{-0.029}(theo.)$ [21] and the *BABAR* upper limit of $|\frac{V_{td}}{V_{ts}}| < 0.19$.

7.7.3 $|\frac{V_{td}}{V_{ts}}|$ from $\frac{B\to(\rho,\omega)\gamma}{B\to K^*\gamma}$

$|\frac{V_{td}}{V_{ts}}|$ has also been calculated from the measurements of $BF(B \to (\rho,\omega)\gamma)$ and $BF(B \to K^*\gamma)$ made as cross-checks in this analysis.

$$\frac{BF(B \to (\rho,\omega)\gamma)}{BF(B \to K^*\gamma)} = 0.039 \pm 0.016(stat.) \pm 0.071(syst.) \pm 0.005(theo.)$$

$$|\frac{V_{td}}{V_{ts}}| = 0.22 \pm 0.09(stat.) \pm 0.04(syst.) \pm 0.03(theo.).$$

$|\frac{V_{td}}{V_{ts}}|$ has been calculated using the same method as the *BABAR* analysis [22] using Equation 7.4, with the values of ζ and ΔR given above and the mass term as given in [19]. This result agrees with the CDF and Belle measurements within errors and with the the value of $|\frac{V_{td}}{V_{ts}}|$ found in this analysis using the ratio of inclusive decays.

7.7.4 Combined $|\frac{V_{td}}{V_{ts}}|$

Combining the inclusive and exclusive measurements of $|\frac{V_{td}}{V_{ts}}|$ increases the statistical significance of the result. The combined measurement

$$|\frac{V_{td}}{V_{ts}}| = 0.26 \pm 0.05(stat.) \pm 0.04(syst.) \pm 0.04(theo.)$$

$$0.15 < |\frac{V_{td}}{V_{ts}}| < 0.37 \quad (90\% \text{ CL})$$

is in good agreement with other published results. The likelihood scan for the combined exclusive and inclusive regions is shown in Figure 7.13.

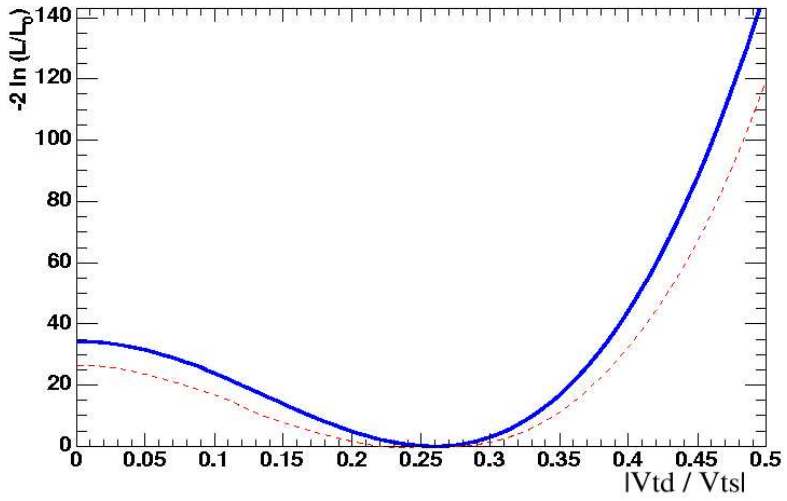

Figure 7.13: Likelihood scan of $|\frac{V_{td}}{V_{ts}}|$ calculated from the combined inclusive and exclusive branching fractions. The dashed curve includes the systematic error.

Chapter 8

Conclusion

Table 8.1 summarises the experimental results described in this thesis.

All measurements made as cross-checks in this analysis agree within errors with both theory and current experimental world averages, and constitute an important verification of the analysis technique. Some are better than the current experimental averages, and give an indication of what to expect from future experimental measures in $b \to (s,d)\gamma$ decays. So far, no discrepancies have been observed between Standard Model predictions and experimental results.

With the neutral current $b \to s\gamma$ now well-established, it is hoped that $b \to d\gamma$ decays will also begin yielding precision measurements, providing independent tests of the Standard Model. The first evidence for the exclusive decays $B \to (\rho,\omega)\gamma$ has been published, and the search for the inclusive process is an important one. This thesis does not observe the $b \to d\gamma$ decay in the inclusive or $B \to (\rho,\omega)\gamma$ regions separately, but there is evidence for the decay in both regions at the $\approx 3\sigma$ level. 90% confidence limits are set on the $b \to d\gamma$ decay at $1.4 \times 10^{-5} < BF(b \to d\gamma) < 3.6 \times 10^{-5}$.

The ratio of CKM matrix elements $|\frac{V_{td}}{V_{ts}}|$ has been measured. The limits $0.17 < |\frac{V_{td}}{V_{ts}}| < 0.43$ at 90% confidence level have been set in this analysis from $\frac{b\to d\gamma}{b\to s\gamma}$ alone. The combined limits from both the inclusive and exclusive mass regions are $0.15 < |\frac{V_{td}}{V_{ts}}| < 0.37$, shown in Figure 8.1 as the central value with experimental errors for comparison with other experimental measurements. This measurement

Analysis	
$B \to K^*\gamma$	$(3.74 \pm 0.16 \pm 0.41) \times 10^{-5}$
A_{CP} in $B \to K^*\gamma$	$-0.079 \pm 0.036 \pm 0.001$
$b \to s\gamma$	$(3.54 \pm 0.19 \pm 0.39) \times 10^{-4}$
A_{CP} in $b \to s\gamma$	$0.040 \pm 0.035 \pm 0.004$
$B \to (\rho, \omega)\gamma$	$(1.46 \pm 0.59^{+0.18}_{-0.19}) \times 10^{-6}$
$b \to d\gamma$	$(2.47 \pm 0.72^{+0.42}_{-0.44}) \times 10^{-5}$
$\lvert\frac{V_{td}}{V_{ts}}\rvert$	$0.26 \pm 0.05 \pm 0.04 \pm 0.04$

Table 8.1: Measurements made in this analysis. First error is statistical, the second systematic and the third (if given) is theoretical. $|\frac{V_{td}}{V_{ts}}|$ is given for the combined inclusive and exclusive measurement.

is consistent with all current experimental results but not yet competitive.

More data is necessary to improve the large statistical errors in the $b \to d\gamma$ measurements and the significant peaking backgrounds must be further studied and their contributions understood. By the end of the *BABAR* Run 5, it is expected that a dataset of more than $400\,\text{fb}^{-1}$ will be collected. Based on the measurements made in this thesis on about half that amount and assuming $BF(b \to d\gamma) = 2.5 \times 10^{-5}$, a measurement of better than 5σ significance is expected. It is likely that with the improved dataset, $|\frac{V_{td}}{V_{ts}}|$ will be determined to within 15% uncertainty using the method outlined in this thesis.

This analysis has established that a measurement of the inclusive $b \to d\gamma$ branching fraction is indeed possible with an enlarged data sample. Measurements of the direct *CP* violation and, eventually, isospin violation will provide stringent tests of SM predictions and hopefully hints of physics beyond the SM.

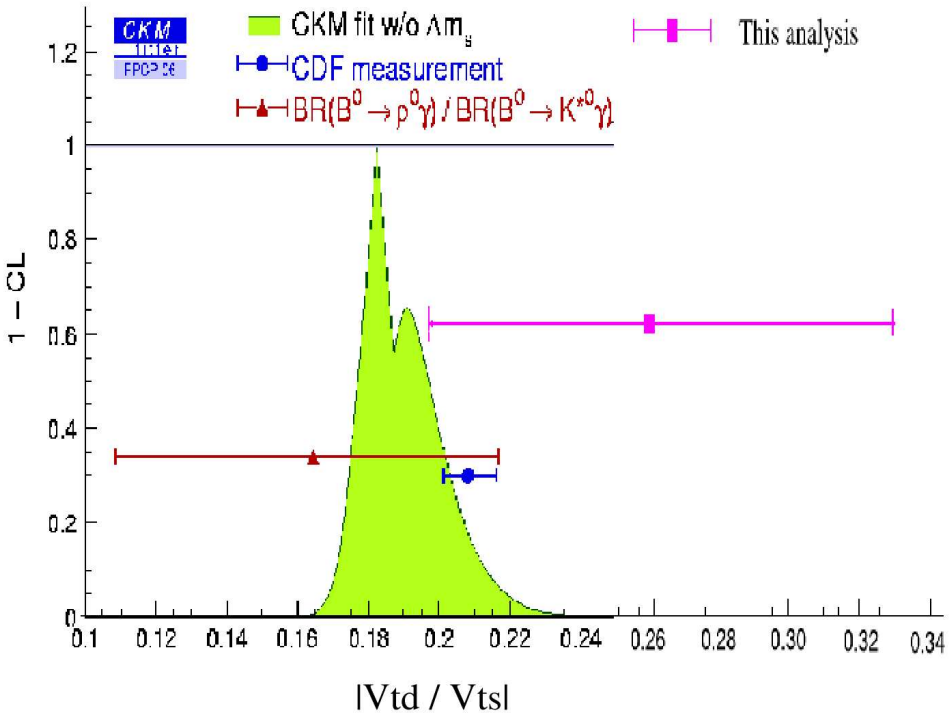

Figure 8.1: Constraints on $|\frac{V_{td}}{V_{ts}}|$, including the measurement made in this thesis. Experimental errors only.

Appendix A

Projection Plots

This Appendix contains results of the likelihood fit to data for the various samples studied in this analysis. The fits are displayed as projection plots in ΔE^* and $m_{\rm ES}$, where the fitted PDFs are shown overlaid on a histogram of data points. Both projections covering the full range of ΔE^* and $m_{\rm ES}$ are shown, as well as projections where a cut is made on the variable not plotted. This is done to enhance the signal component in the projection. A cut of $5.274\,{\rm GeV}/c^2 < m_{\rm ES} < 5.286\,{\rm GeV}/c^2$ is applied for the ΔE^* projection, and a cut of $-0.15\,{\rm GeV} < \Delta{\rm E}^* < 0.10\,{\rm GeV}$ applied for the $m_{\rm ES}$ distribution.

A.1 $B \to K^*\gamma$ results

A.1.1 $B \to K^*\gamma$ Runs 1 - 2 projection plots

Figures A.1 and A.2 show projections in ΔE^* and $m_{\rm ES}$ over the full range of the fit variables, for the Runs 1 - 2 $B \to K^*\gamma$ data sample in the mass region $0.6\,{\rm GeV}/c^2$- $1.0\,{\rm GeV}/c^2$.

A.1.2 $B \to K^*\gamma$ Runs 1 - 4 projection plots

Figures A.3 and A.4 show projections in ΔE^* and $m_{\rm ES}$ over the full range of the fit variables for the full Runs 1 - 4 $B \to K^*\gamma$ data sample. Figures A.5 and A.6 show projections in ΔE^* and $m_{\rm ES}$ over with cuts applied on the variable not

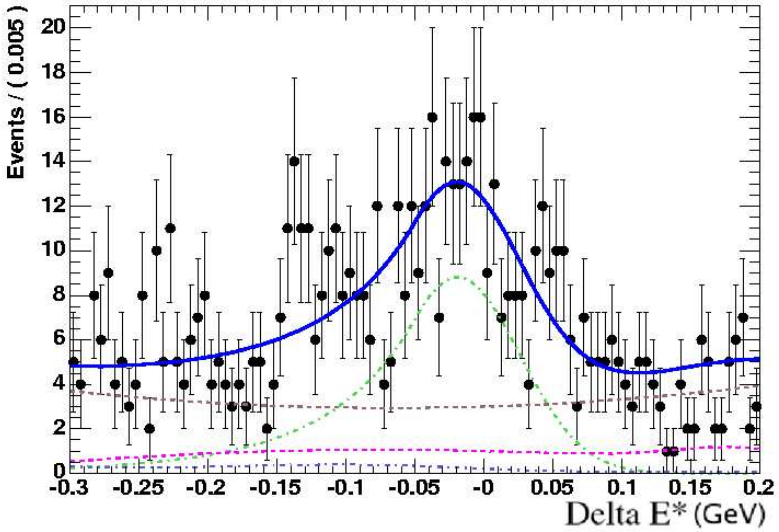

Figure A.1: ΔE^* distribution in data for the K^* control region for the Runs 1 - 2 dataset. Signal is shown in green, $b \to s\gamma$ cross-feed in pink, generic B background in blue and continuum background in brown.

plotted.

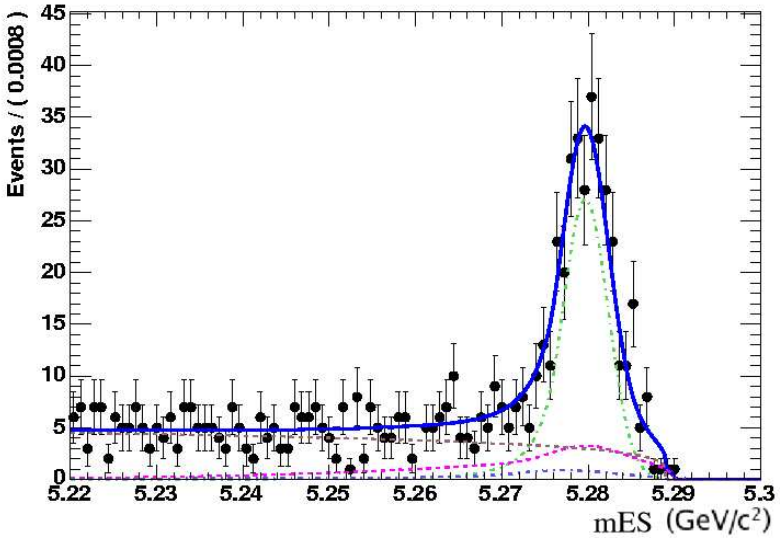

Figure A.2: $m_{\rm ES}$ distribution in data for the K^* control region for the Runs 1 - 2 dataset. Signal is shown in green, $b \to s\gamma$ cross-feed in pink, generic B background in blue and continuum background in brown.

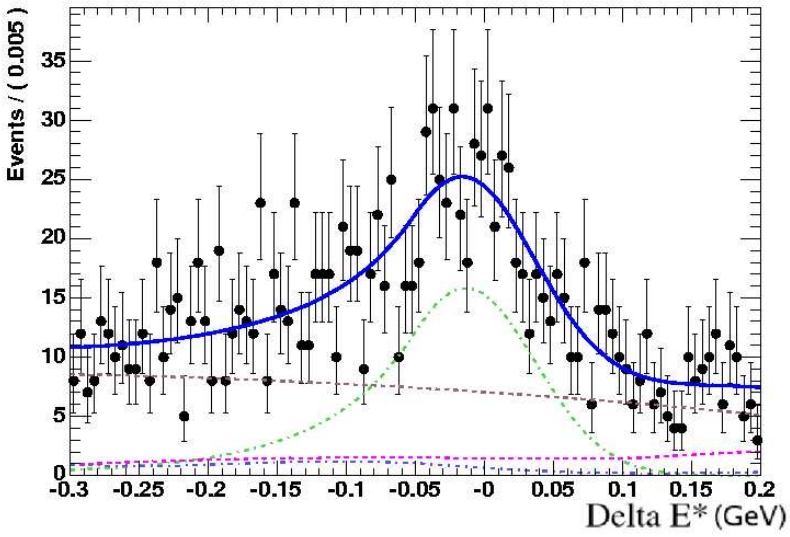

Figure A.3: ΔE^* distribution in data for the K^* control region for the full Runs 1 - 4 dataset. Signal is shown in green, $b \to s\gamma$ cross-feed in pink, generic B background in blue and continuum background in brown.

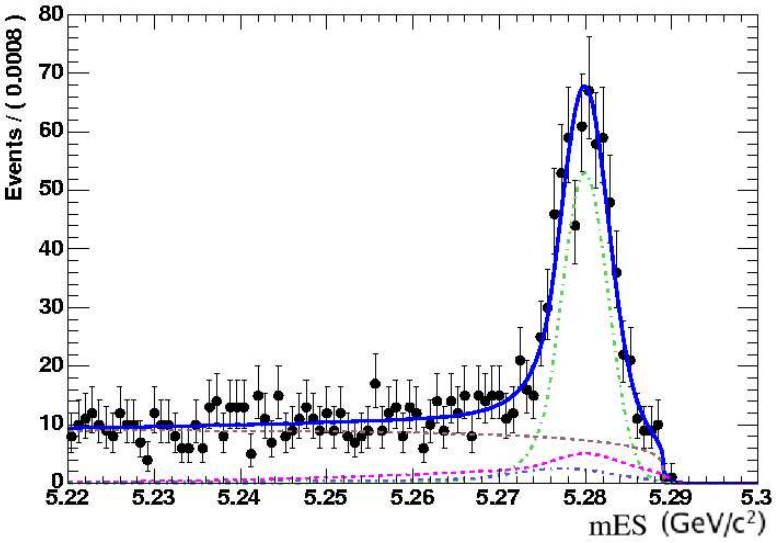

Figure A.4: $m_{\rm ES}$ distribution in data for the K^* control region for the full Runs 1 - 4 dataset. Signal is shown in green, $b \to s\gamma$ cross-feed in pink, generic B background in blue and continuum background in brown.

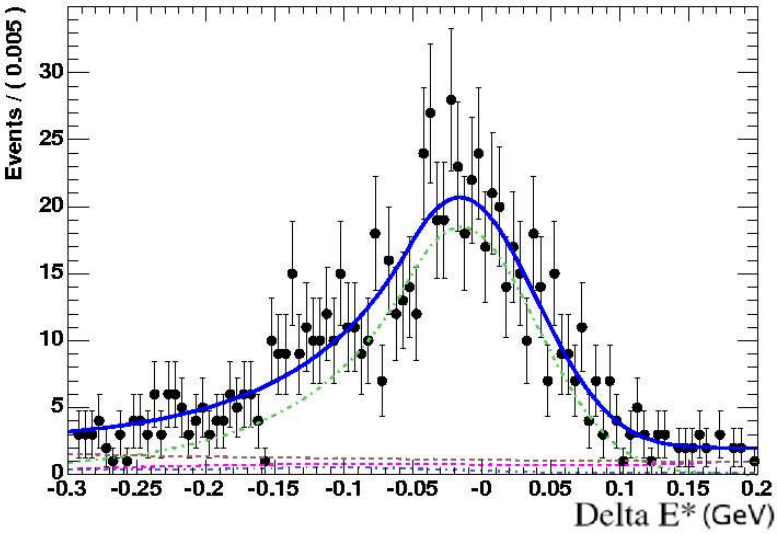

Figure A.5: ΔE^* distribution in data for the K^* control region for the full Runs 1 - 4 dataset, with the cut $5.274\,\mathrm{GeV}/c^2 < m_{\rm ES} < 5.286\,\mathrm{GeV}/c^2$ applied. Signal is shown in green, $b \to s\gamma$ cross-feed in pink, generic B background in blue and continuum background in brown.

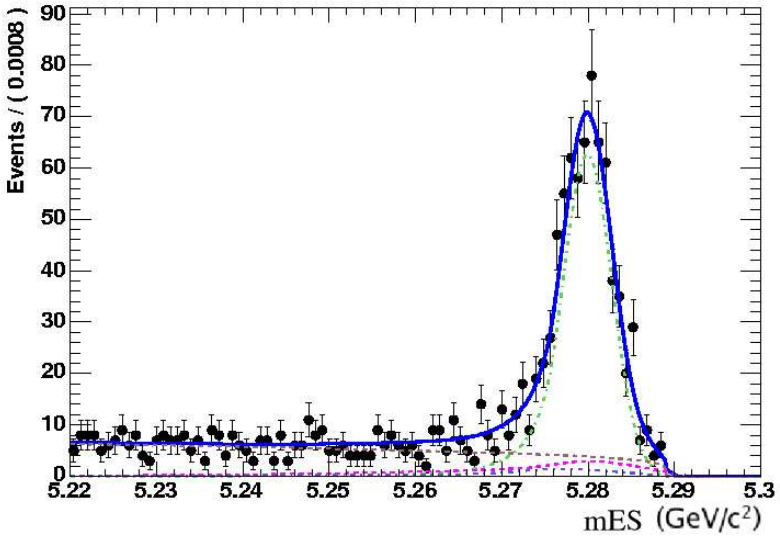

Figure A.6: $m_{\rm ES}$ distribution in data for the K^* control region for the full Runs 1 - 4 dataset, with the cut $-0.15\,\text{GeV} < \Delta\text{E}^* < 0.10\,\text{GeV}$ applied. Signal is shown in green, $b \to s\gamma$ cross-feed in pink, generic B background in blue and continuum background in brown.

A.1.3 Separation of charged and neutral modes

This section contains projection plots of the separated charged and neutral K^* modes. Figures A.7 and A.8 show the ΔE^* and $m_{\rm ES}$ distributions over the full range of each variable for the $B^0 \to K^{*0}(K^{*0} \to K^+\pi^-)\gamma$ exclusive decay. Figures A.9 and A.10 show the ΔE^* and $m_{\rm ES}$ distributions over the full range of each variable for the $B^+ \to K^{*+}(K^{*+} \to K^+\pi^0)\gamma$ exclusive decay.

Figures A.11 and A.12 show the ΔE^* and $m_{\rm ES}$ distributions for the $B^0 \to K^{*0}(K^{*0} \to K^+\pi^-)\gamma$ exclusive decay, with cuts applied to the variable not plotted. Figures A.13 and A.14 show the ΔE^* and $m_{\rm ES}$ distributions for the $B^+ \to K^{*+}(K^{*+} \to K^+\pi^0)\gamma$ exclusive decay, with cuts applied to the variable not plotted.

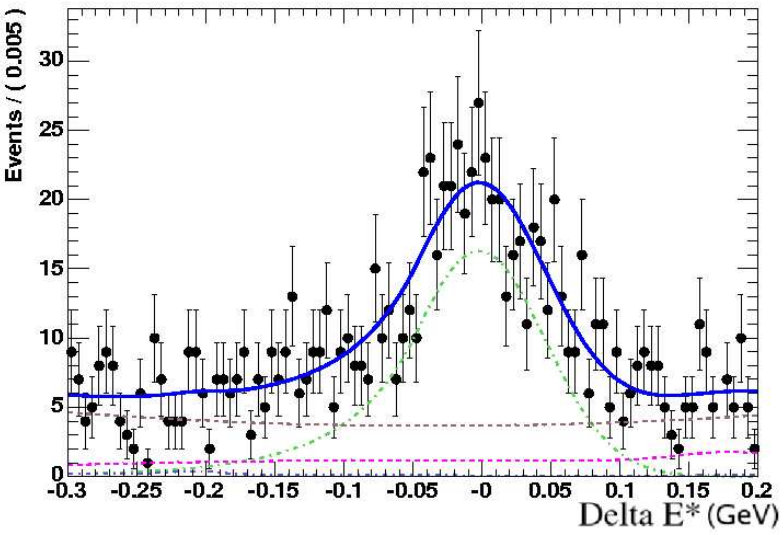

Figure A.7: ΔE^* distribution in data for the $B^0 \to K^{*0}(K^{*0} \to K^+\pi^-)\gamma$ exclusive decay mode. Signal is shown in green, $b \to s\gamma$ cross-feed in pink, generic B background in blue and continuum background in brown.

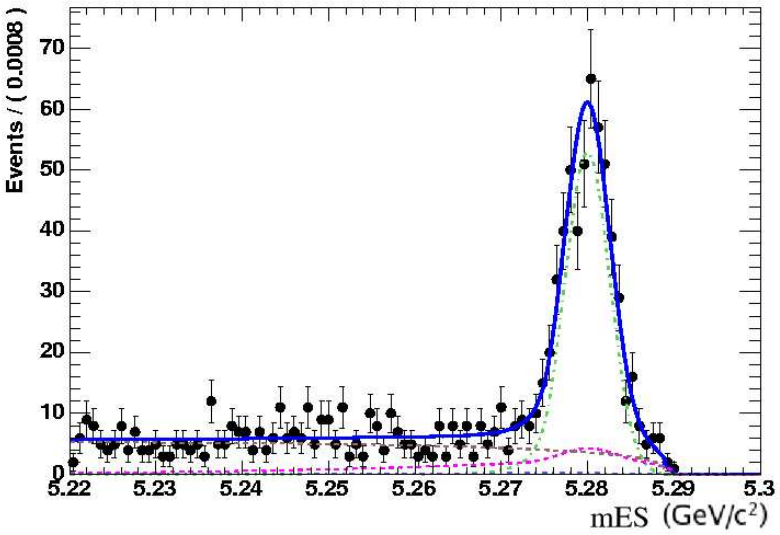

Figure A.8: $m_{\rm ES}$ distribution in data for the $B^0 \to K^{*0}(K^{*0} \to K^+\pi^-)\gamma$ exclusive decay mode. Signal is shown in green, $b \to s\gamma$ cross-feed in pink, generic B background in blue and continuum background in brown.

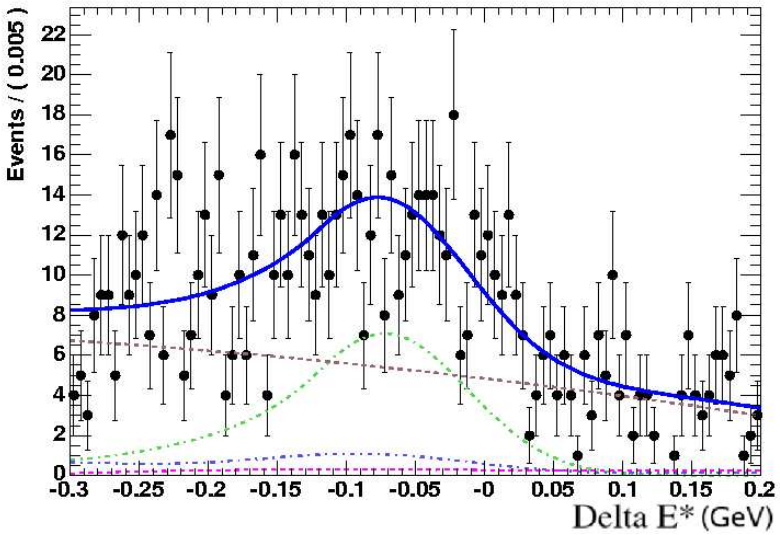

Figure A.9: ΔE^* distribution in data for the $B^+ \to K^{*+}(K^{*+} \to K^+\pi^0)\gamma$ exclusive decay mode. Signal is shown in green, $b \to s\gamma$ cross-feed in pink, generic B background in blue and continuum background in brown.

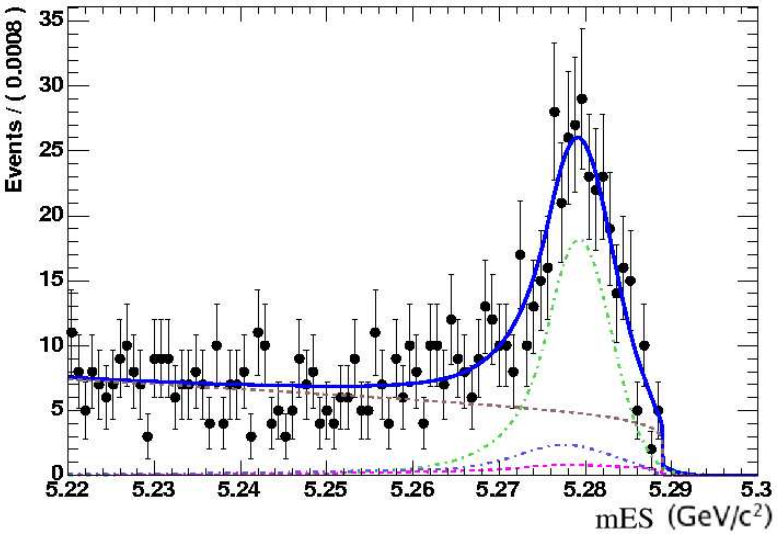

Figure A.10: $m_{\rm ES}$ distribution in data for the $B^+ \to K^{*+}(K^{*+} \to K^+\pi^0)\gamma$ exclusive decay mode. Signal is shown in green, $b \to s\gamma$ cross-feed in pink, generic B background in blue and continuum background in brown.

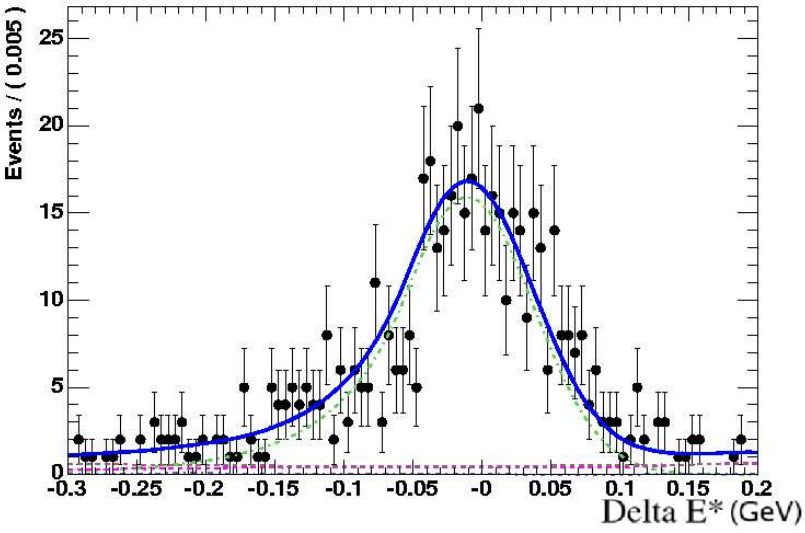

Figure A.11: ΔE^* distribution in data for the $B^0 \to K^{*0}(K^{*0} \to K^+\pi^-)\gamma$ exclusive decay mode, with the cut $5.274\,\mathrm{GeV}/c^2 < m_{\rm ES} < 5.286\,\mathrm{GeV}/c^2$ applied. Signal is shown in green, $b \to s\gamma$ cross-feed in pink, generic B background in blue and continuum background in brown.

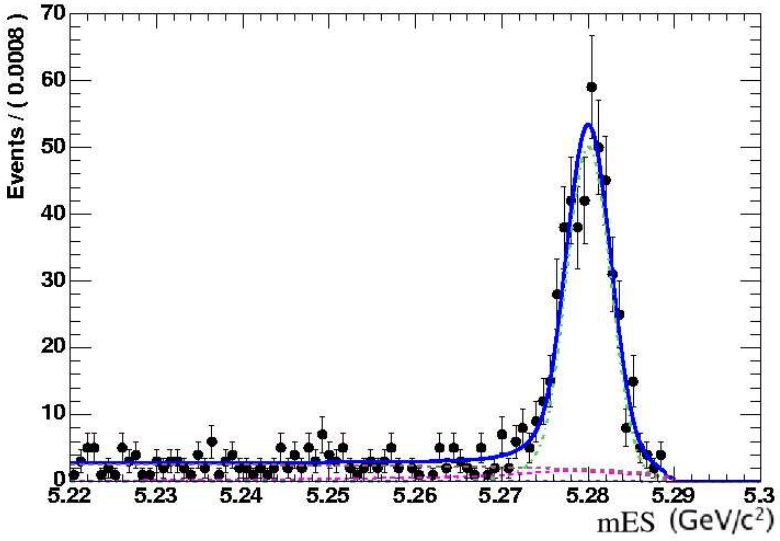

Figure A.12: $m_{\rm ES}$ distribution in data for the $B^0 \to K^{*0}(K^{*0} \to K^+\pi^-)\gamma$ exclusive decay mode, with the cut $-0.15\,\text{GeV} < \Delta\text{E}^* < 0.10\,\text{GeV}$ applied. Signal is shown in green, $b \to s\gamma$ cross-feed in pink, generic B background in blue and continuum background in brown.

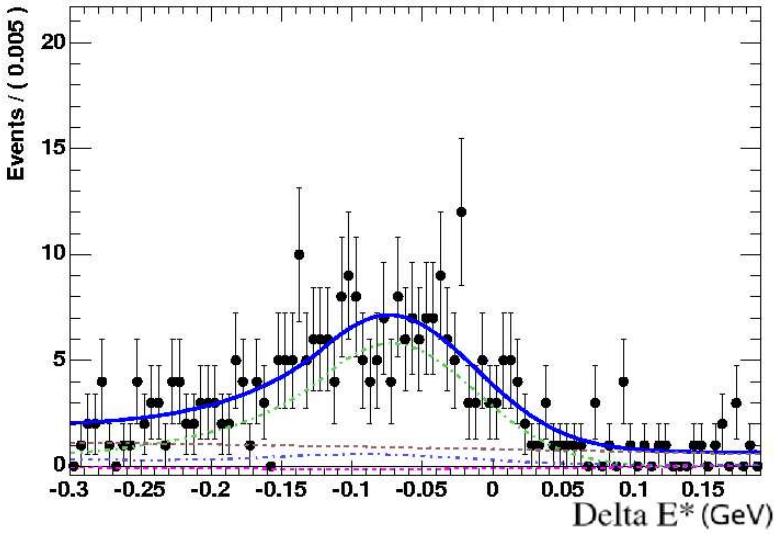

Figure A.13: ΔE^* distribution in data for the $B^+ \to K^{*+}(K^{*+} \to K^+\pi^0)\gamma$ exclusive decay mode, with the cut $5.274\,\text{GeV}/c^2 < m_{\rm ES} < 5.286\,\text{GeV}/c^2$ applied. Signal is shown in green, $b \to s\gamma$ cross-feed in pink, generic B background in blue and continuum background in brown.

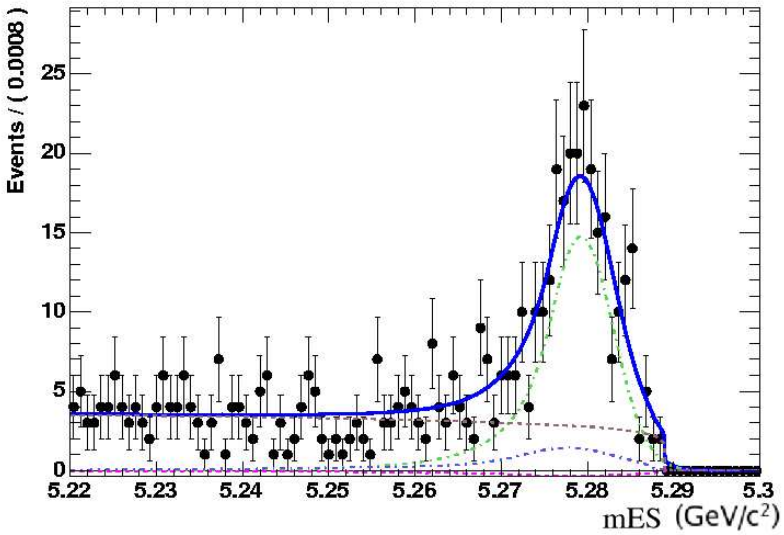

Figure A.14: $m_{\rm ES}$ distribution in data for the $B^+ \to K^{*+}(K^{*+} \to K^+\pi^0)\gamma$ exclusive decay mode, with the cut $-0.15\,\mathrm{GeV} < \Delta \mathrm{E}^* < 0.10\,\mathrm{GeV}$ applied. Signal is shown in green, $b \to s\gamma$ cross-feed in pink, generic B background in blue and continuum background in brown.

A.1.4 A_{CP} in $B \to K^*\gamma$

The projections of the likelihood fit to data is shown for the $B \to K^*\gamma$ samples containing positively and negatively charged Kaons, used to measure the direct *CP* violation of the decay. Figures A.15 and A.16 show the projections of the sample containing K^+s over the full range of ΔE^* and $m_{\rm ES}$. Figures A.17 and A.18 show the projections of the sample containing K^-s over the full range of ΔE^* and $m_{\rm ES}$.

Figures A.19 and A.20 show the projections of the sample containing K^+s over the ΔE^* and $m_{\rm ES}$ distributions, with cuts applied to the variable not plotted. Figures A.21 and A.22 show the projections of the sample containing K^-s in over the ΔE^* and $m_{\rm ES}$distributions, with cuts applied to the variable not plotted.

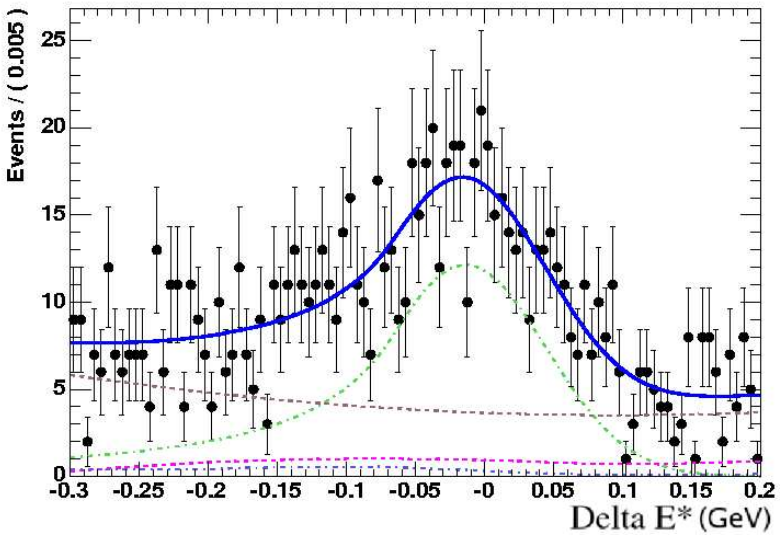

Figure A.15: ΔE^* distribution in data for the $B \to K^*\gamma$ sample containing K^+s, for the full *BABAR* dataset of 222x10^6 $B\bar{B}$ pairs. Signal is shown in green, $b \to s\gamma$ cross-feed in pink, generic B background in blue and continuum background in brown.

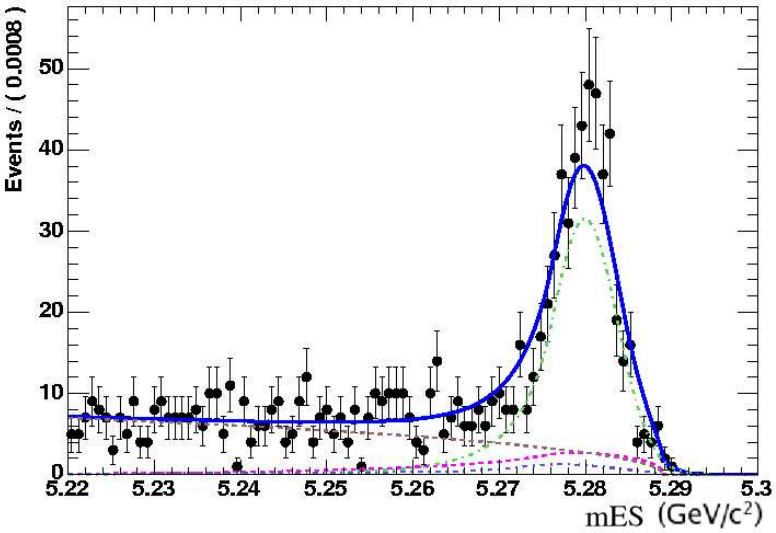

Figure A.16: $m_{\rm ES}$ distribution in data for the $B \to K^*\gamma$ sample containing K^+s, for the full *BABAR* dataset of 222x10^6 $B\bar{B}$ pairs. Signal is shown in green, $b \to s\gamma$ cross-feed in pink, generic B background in blue and continuum background in brown.

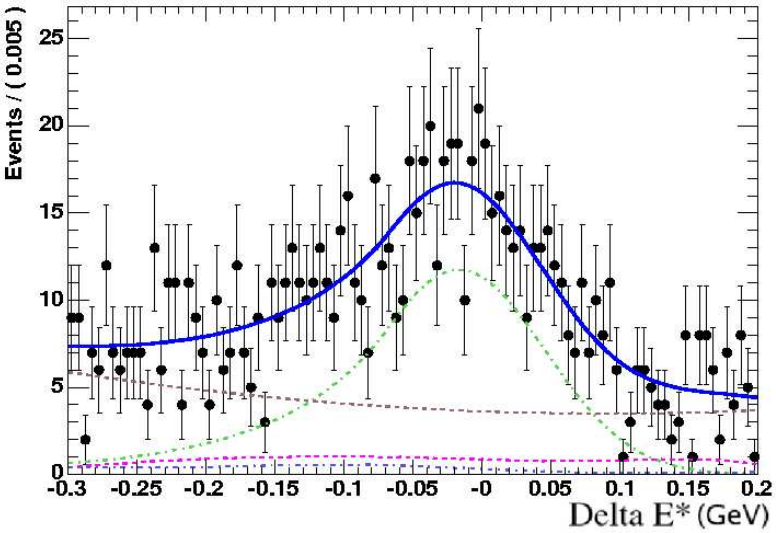

Figure A.17: ΔE^* distribution in data for the $B \to K^*\gamma$ sample containing K^-s, for the full *BABAR* dataset of 222x10^6 $B\bar{B}$ pairs. Signal is shown in green, $b \to s\gamma$ cross-feed in pink, generic B background in blue and continuum background in brown.

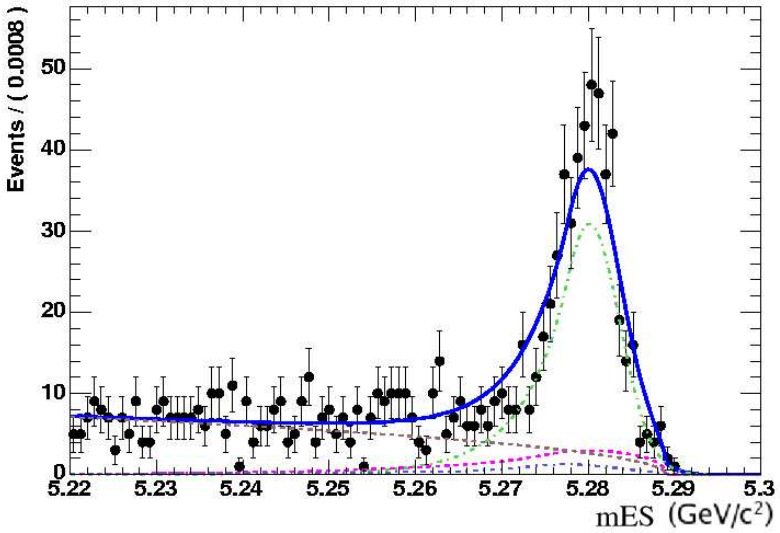

Figure A.18: $m_{\rm ES}$ distribution in data for the $B \to K^*\gamma$ containing K^-s, for the full *BABAR* dataset of 222x10^6 $B\bar{B}$ pairs. Signal is shown in green, $b \to s\gamma$ cross-feed in pink, generic B background in blue and continuum background in brown.

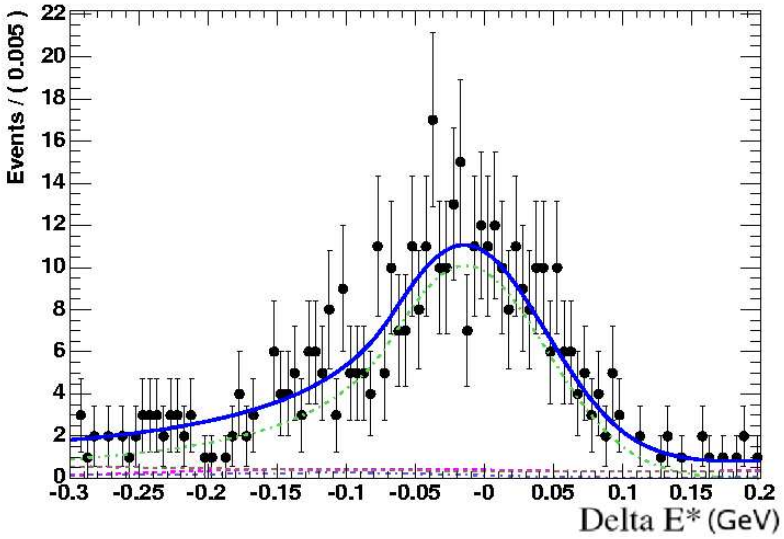

Figure A.19: ΔE^* distribution in data for the $B \to K^*\gamma$ containing K^+s, for the full *BABAR* dataset of 222x10^6 $B\bar{B}$ pairs. Signal is shown in green, $b \to s\gamma$ cross-feed in pink, generic B background in blue and continuum background in brown.

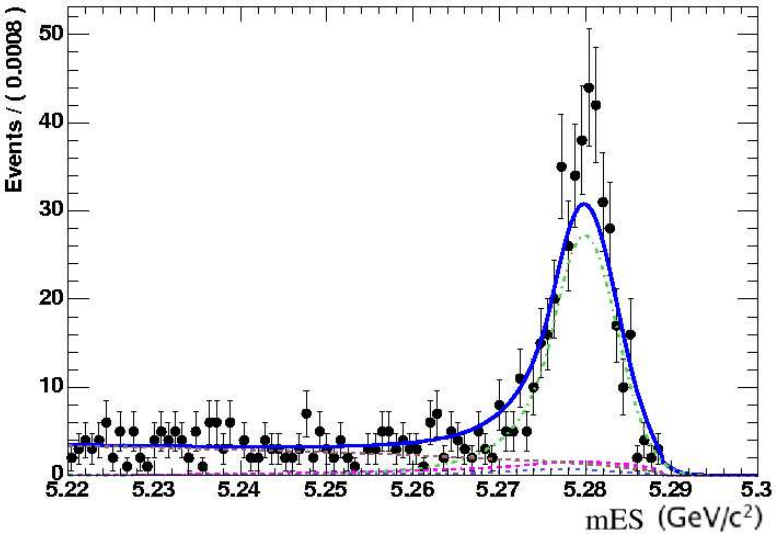

Figure A.20: $m_{\rm ES}$ distribution in data for the $B \to K^*\gamma$ sample containing K^+s, for the full *BABAR* dataset of 222x10^6 $B\bar{B}$ pairs, with the cut $5.274\,{\rm GeV}/c^2 < m_{\rm ES} < 5.286\,{\rm GeV}/c^2$ applied, with the cut $-0.15\,{\rm GeV} < \Delta{\rm E}^* < 0.10\,{\rm GeV}$ applied. Signal is shown in green, $b \to s\gamma$ cross-feed in pink, generic B background in blue and continuum background in brown.

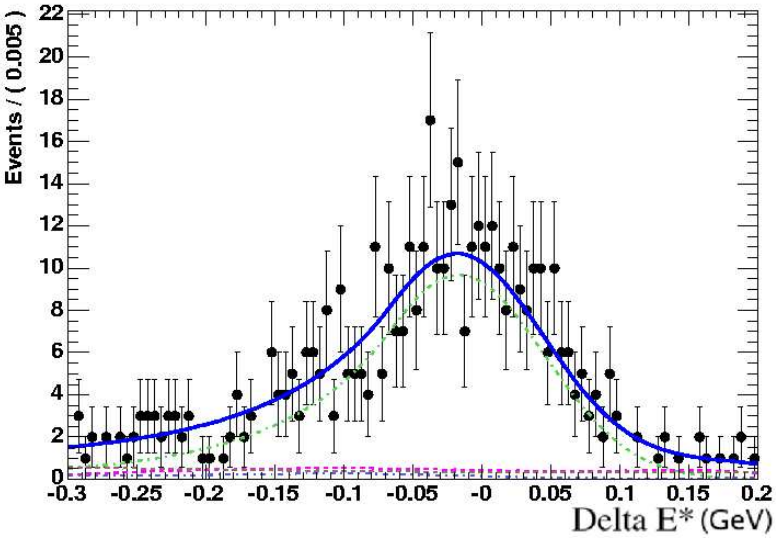

Figure A.21: ΔE^* distribution in data for the $B \to K^*\gamma$ sample containing K^-s, for the full *BABAR* dataset of 222x10^6 $B\bar{B}$ pairs, with the cut $5.274\,{\rm GeV}/c^2 < m_{\rm ES} < 5.286\,{\rm GeV}/c^2$ applied. Signal is shown in green, $b \to s\gamma$ cross-feed in pink, generic B background in blue and continuum background in brown.

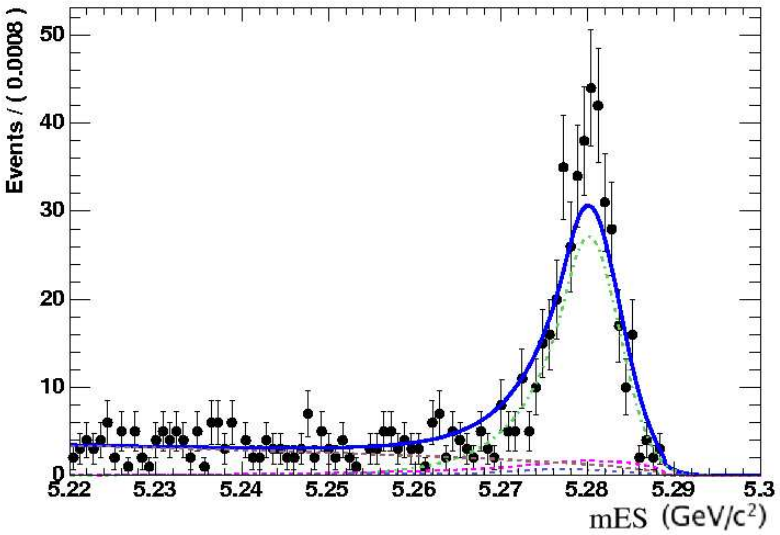

Figure A.22: $m_{\rm ES}$ distribution in data for the $B \to K^*\gamma$ sample containing K^-s, for the full *BABAR* dataset of 222x10^6 $B\bar{B}$ pairs, with the cut $-0.15\,\text{GeV} < \Delta\text{E}^* < 0.10\,\text{GeV}$ applied. Signal is shown in green, $b \to s\gamma$ cross-feed in pink, generic B background in blue and continuum background in brown.

A.2 $b \to s\gamma$ results

A.2.1 $b \to s\gamma$ Runs 1 - 2 projection plots

Figures A.23 and A.24 show the projections in ΔE^* and $m_{\rm ES}$ in the Runs 1 - 2 $b \to s\gamma$ data sample, covering the mass range 1.0 GeV/c^2-1.8 GeV/c^2.

Figures A.25 and A.26 show the projections in ΔE^* and $m_{\rm ES}$ in the Runs 1 - 2 $b \to s\gamma$ data sample, with cuts applied to the variable not plotted.

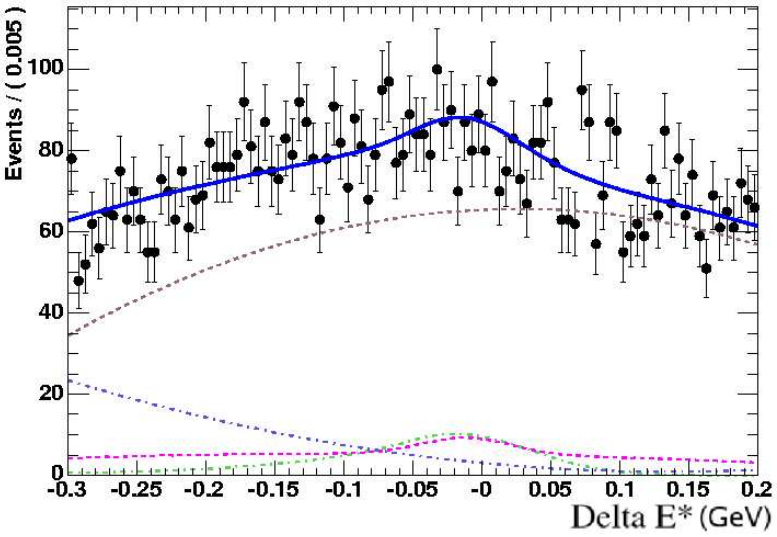

Figure A.23: ΔE^* distribution in data for $b \to s\gamma$ for the Runs 1 - 2 dataset. Signal is shown in green, $b \to s\gamma$ cross-feed in pink, generic B background in blue and continuum background in brown.

A.2.2 $b \to s\gamma$ Runs 1 - 4 projection plots

The projection plots in this section show the fit to data for the full Runs 1 - 4 $b \to s\gamma$ data sample. Figures A.27 and A.28 show the projections for ΔE^* and $m_{\rm ES}$, over the full range of each variable.

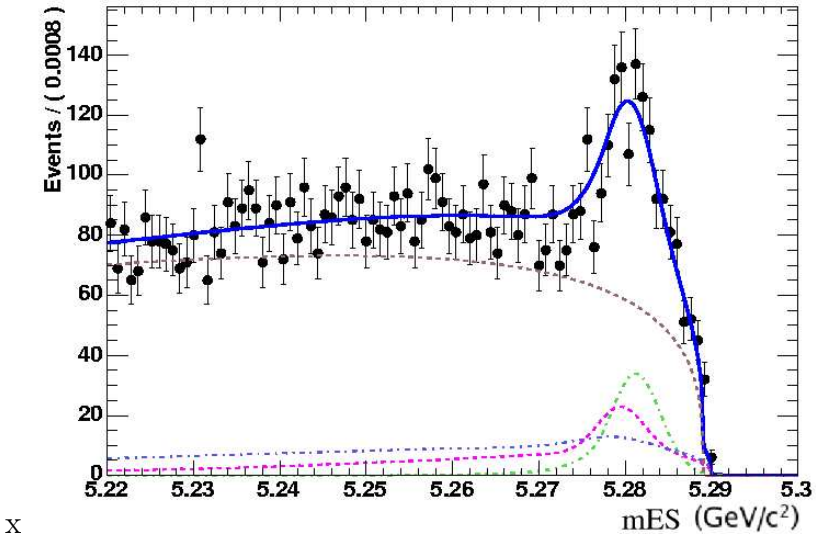

x

Figure A.24: $m_{\rm ES}$ distribution in data for $b \to s\gamma$ for the Runs 1 - 2 dataset. Signal is shown in green, $b \to s\gamma$ cross-feed in pink, generic B background in blue and continuum background in brown.

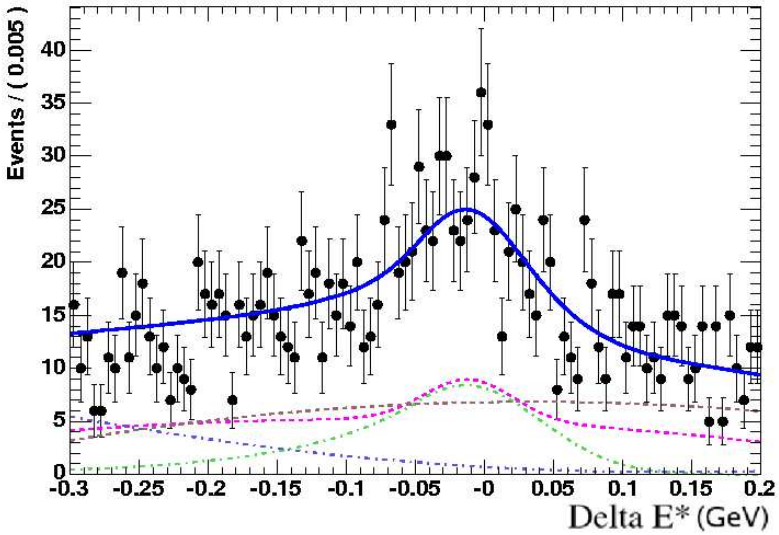

Figure A.25: ΔE^* distribution in data for $b \to s\gamma$ for the Runs 1 - 2 dataset, with the cut $5.274\,\mathrm{GeV}/c^2 < m_{\rm ES} < 5.286\,\mathrm{GeV}/c^2$ applied. Signal is shown in green, $b \to s\gamma$ cross-feed in pink, generic B background in blue and continuum background in brown.

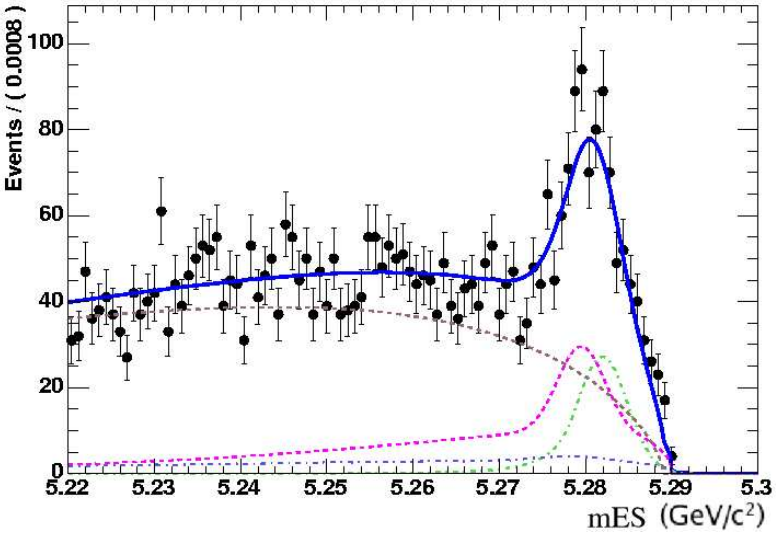

Figure A.26: $m_{\rm ES}$ distribution in data for $b \to s\gamma$ for the Runs 1 - 2 dataset, with the cut $-0.15\,\text{GeV} < \Delta\text{E}^* < 0.10\,\text{GeV}$ applied. Signal is shown in green, $b \to s\gamma$ cross-feed in pink, generic B background in blue and continuum background in brown.

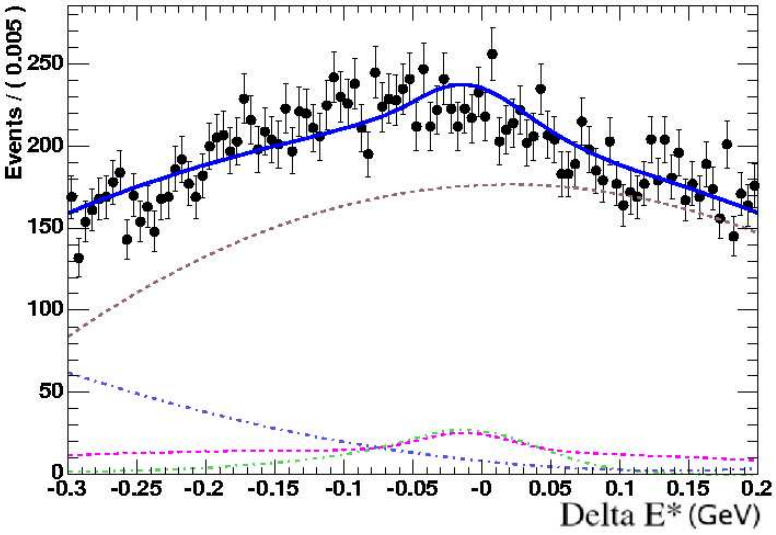

Figure A.27: ΔE^* distribution in data for $b \to s\gamma$ for the full *BABAR* dataset of 222x10^6 $B\bar{B}$ pairs. Signal is shown in green, $b \to s\gamma$ cross-feed in pink, generic B background in blue and continuum background in brown.

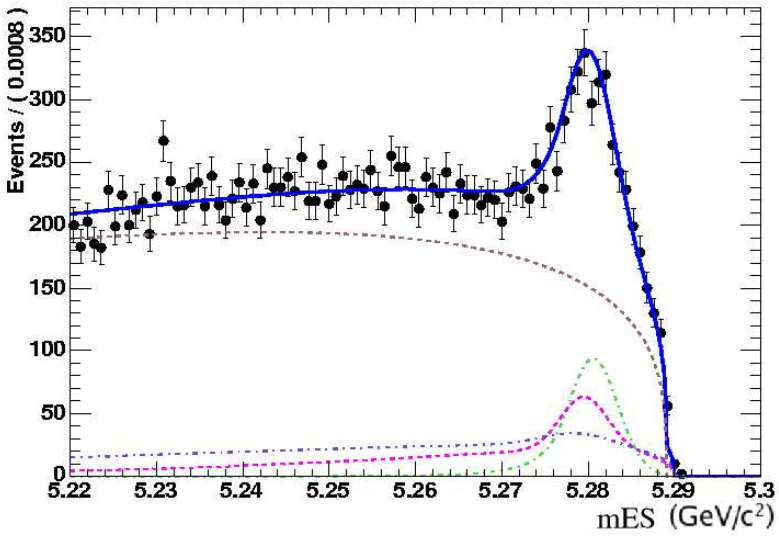

Figure A.28: $m_{\rm ES}$ distribution in data for $b \to s\gamma$ for the full *BABAR* dataset of 222x10^6 $B\bar{B}$ pairs. Signal is shown in green, $b \to s\gamma$ cross-feed in pink, generic B background in blue and continuum background in brown.

A.2.3 A_{CP} in $b \to s\gamma$

The projections of the likelihood fit to data is shown for the $b \to s\gamma$ samples containing positively and negatively charged Kaons, used to measure the direct *CP* violation of the decay. Figures A.29 and A.30 show the projections of the sample containing K^+s over the full range of ΔE^* and $m_{\rm ES}$. Figures A.31 and A.32 show the projections of the sample containing K^-s over the full range of ΔE^* and $m_{\rm ES}$.

Figures A.33 and A.34 show the projections of the sample containing K^+s over the ΔE^* and $m_{\rm ES}$ distributions, with cuts applied to the variable not plotted. Figures A.35 and A.36 show the projections of the sample containing K^-s in over the ΔE^* and $m_{\rm ES}$distributions, with cuts applied to the variable not plotted.

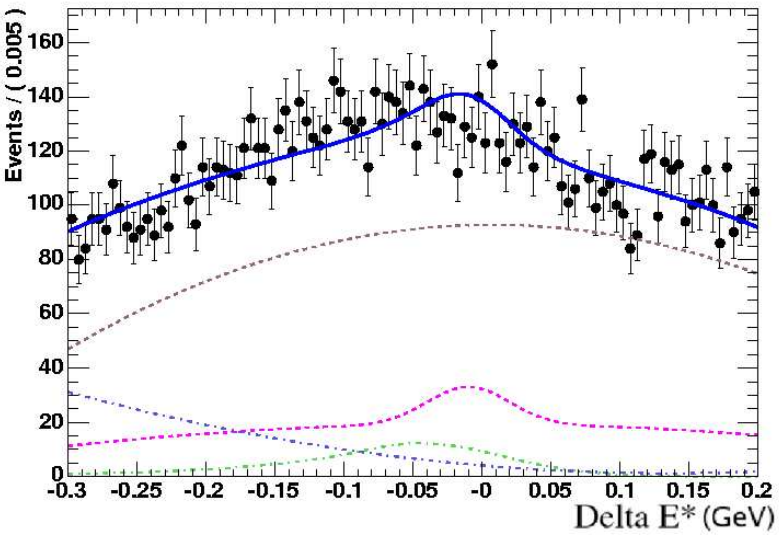

Figure A.29: ΔE^* distribution in data for the $b \to s\gamma$ sample containing K^+s, for the full *BABAR* dataset of 222x10^6 $B\bar{B}$ pairs. Signal is shown in green, $b \to s\gamma$ cross-feed in pink, generic B background in blue and continuum background in brown.

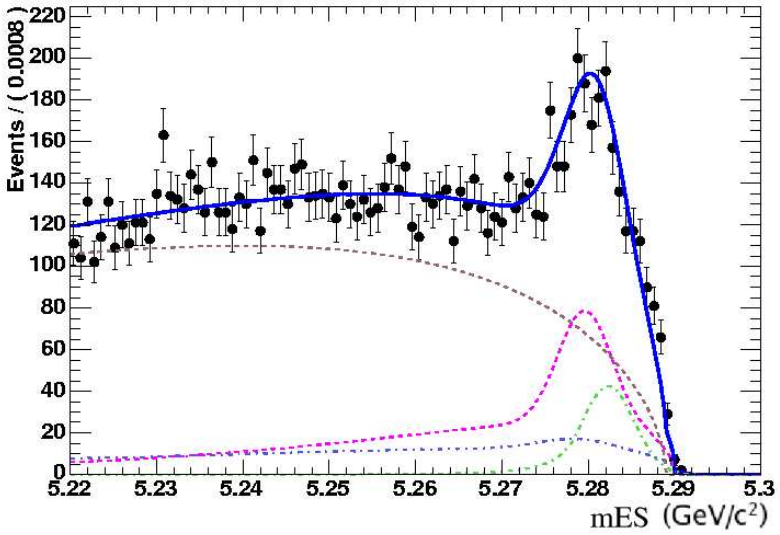

Figure A.30: $m_{\rm ES}$ distribution in data for the $b \to s\gamma$ sample containing K^+s, for the full *BABAR* dataset of 222x10^6 $B\bar{B}$ pairs. Signal is shown in green, $b \to s\gamma$ cross-feed in pink, generic B background in blue and continuum background in brown.

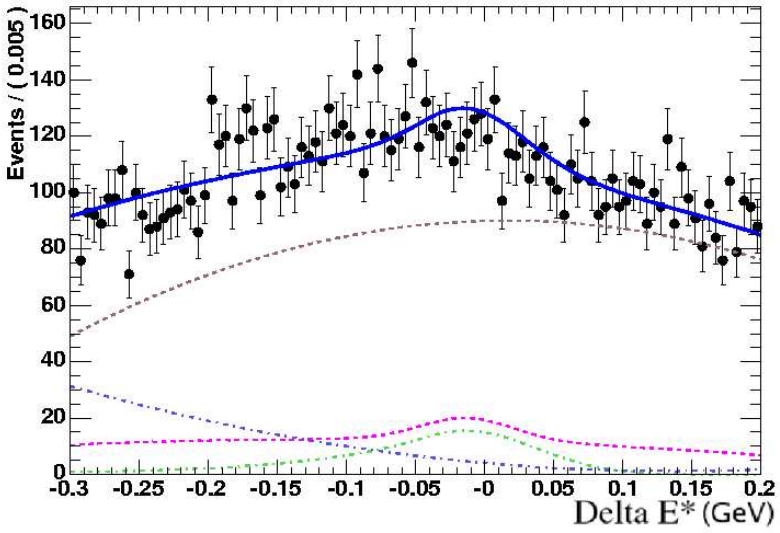

Figure A.31: ΔE^* distribution in data for the $b \to s\gamma$ sample containing K^-s, for the full *BABAR* dataset of 222x10^6 $B\bar{B}$ pairs. Signal is shown in green, $b \to s\gamma$ cross-feed in pink, generic B background in blue and continuum background in brown.

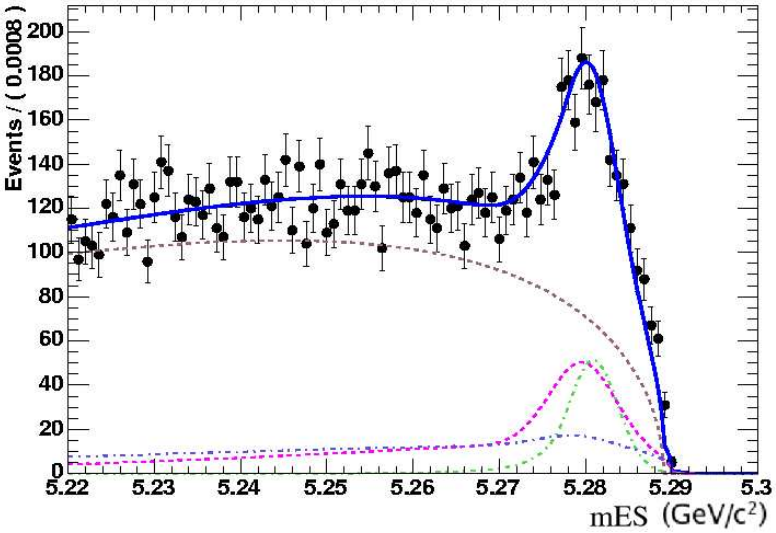

Figure A.32: $m_{\rm ES}$ distribution in data for the $b \to s\gamma$ containing K^-s, for the full *BABAR* dataset of 222x10^6 $B\bar{B}$ pairs. Signal is shown in green, $b \to s\gamma$ cross-feed in pink, generic B background in blue and continuum background in brown.

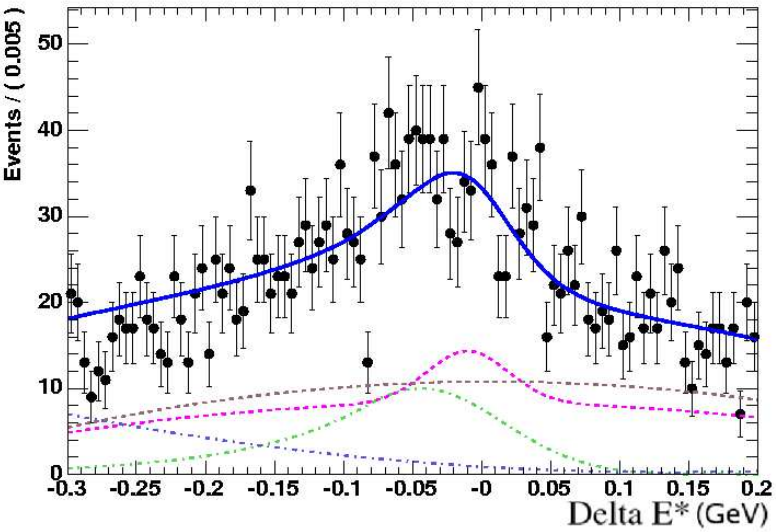

Figure A.33: ΔE^* distribution in data for the $b \to s\gamma$ containing K^+s, for the full *BABAR* dataset of 222x10^6 $B\bar{B}$ pairs. Signal is shown in green, $b \to s\gamma$ cross-feed in pink, generic B background in blue and continuum background in brown.

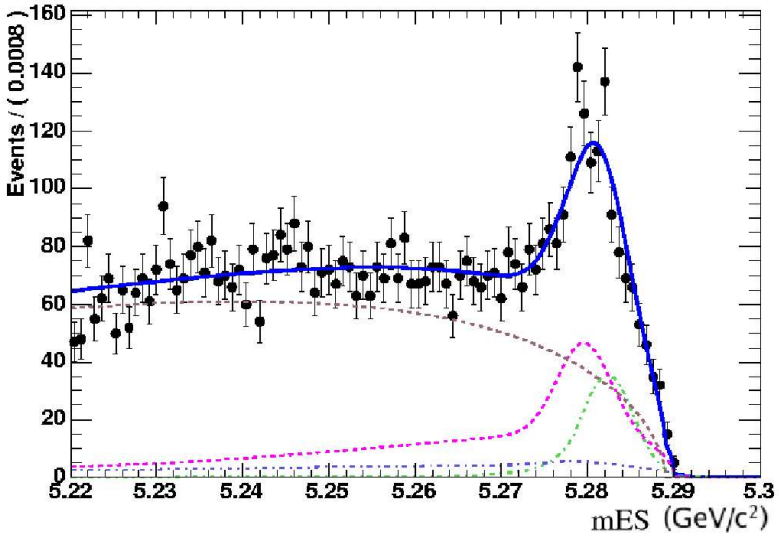

Figure A.34: $m_{\rm ES}$ distribution in data for the $b \to s\gamma$ sample containing K^+s, for the full *BABAR* dataset of 222x10^6 $B\bar{B}$ pairs, with the cut $5.274\,{\rm GeV}/c^2 < m_{\rm ES} < 5.286\,{\rm GeV}/c^2$ applied, with the cut $-0.15\,{\rm GeV} < \Delta{\rm E}^* < 0.10\,{\rm GeV}$ applied. Signal is shown in green, $b \to s\gamma$ cross-feed in pink, generic B background in blue and continuum background in brown.

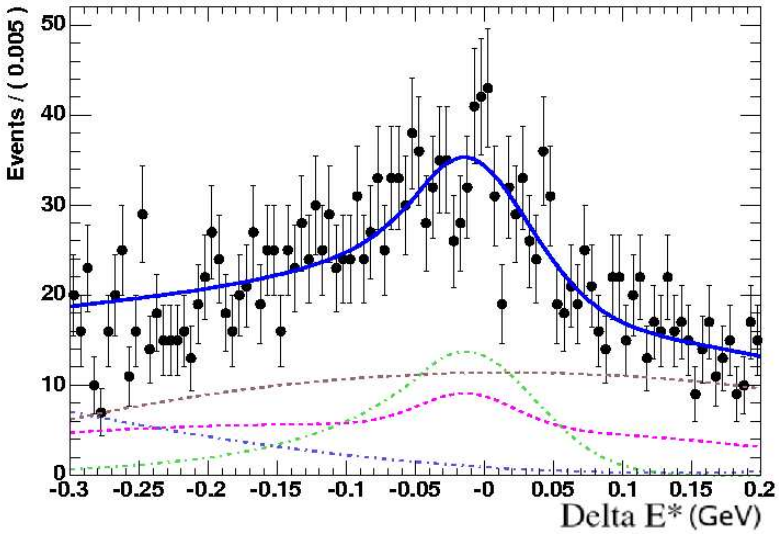

Figure A.35: ΔE^* distribution in data for the $b \to s\gamma$ sample containing K^-s, for the full *BABAR* dataset of 222x10^6 $B\bar{B}$ pairs, with the cut $5.274\,{\rm GeV}/c^2 < m_{\rm ES} < 5.286\,{\rm GeV}/c^2$ applied. Signal is shown in green, $b \to s\gamma$ cross-feed in pink, generic B background in blue and continuum background in brown.

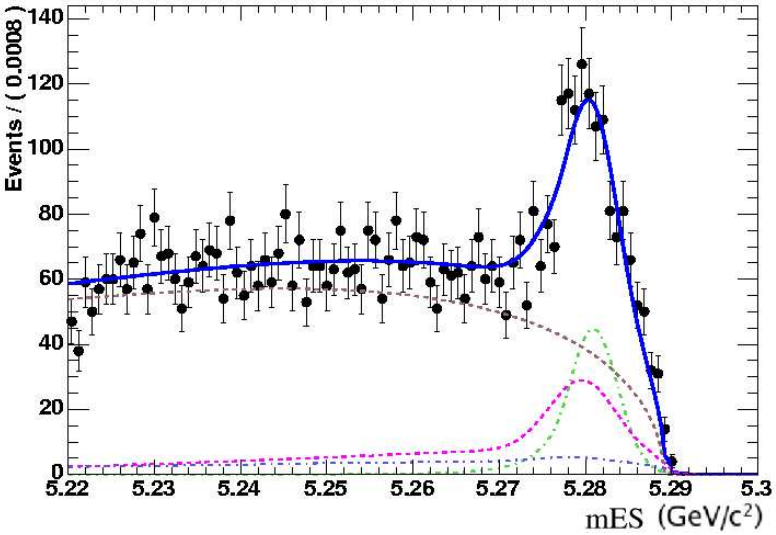

Figure A.36: $m_{\rm ES}$ distribution in data for the $b \to s\gamma$ sample containing K^-s, for the full *BABAR* dataset of 222x10^6 $B\bar{B}$ pairs, with the cut $-0.15\,\text{GeV} < \Delta\text{E}^* < 0.10\,\text{GeV}$ applied. Signal is shown in green, $b \to s\gamma$ cross-feed in pink, generic B background in blue and continuum background in brown.

A.3 $B \to (\rho, \omega)\gamma$ results

Here, the low mass region (0.6 GeV/c^2-1.0 GeV/c^2) of the $b \to d\gamma$ data sample containing the $B \to (\rho, \omega)\gamma$ resonances is fit. Figures A.37 and A.38 show the fit to data over the full range of ΔE^* and $m_{\rm ES}$.

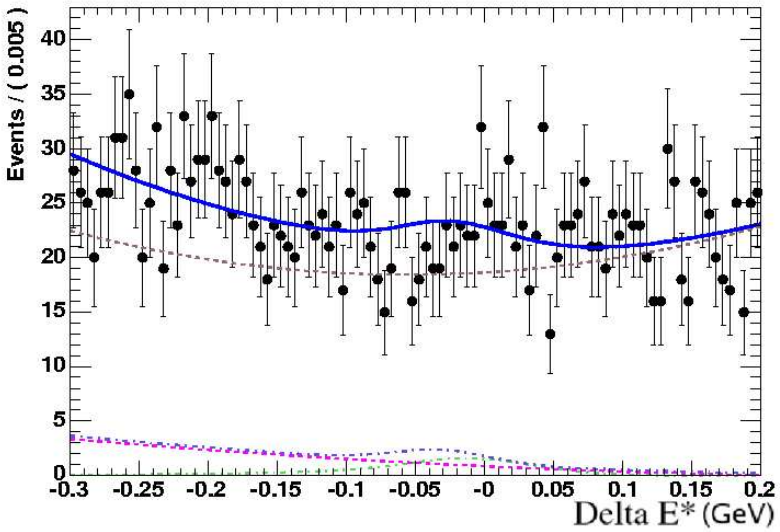

Figure A.37: ΔE^* distribution in data for $B \to (\rho, \omega)\gamma$ for the full *BABAR* dataset of 222x10^6 $B\bar{B}$ pairs. Signal is shown in green, $b \to s\gamma$ cross-feed in pink, generic B background in blue and continuum background in brown.

A.4 $b \to d\gamma$ results

Figures A.39 and A.39 show the fits to data over the full ΔE^* and $m_{\rm ES}$ ranges for the $b \to d\gamma$ data sample in the mass range 1.0 GeV/c^2-1.8 GeV/c^2.

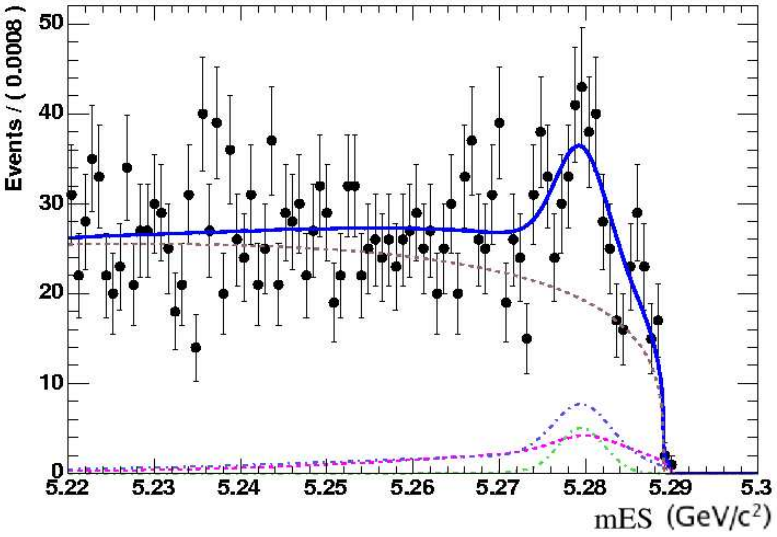

Figure A.38: $m_{\rm ES}$ distribution in data for $B \to (\rho, \omega)\gamma$ for the full *BABAR* dataset of 222x10^6 $B\bar{B}$ pairs. Signal is shown in green, $b \to s\gamma$ cross-feed in pink, generic B background in blue and continuum background in brown.

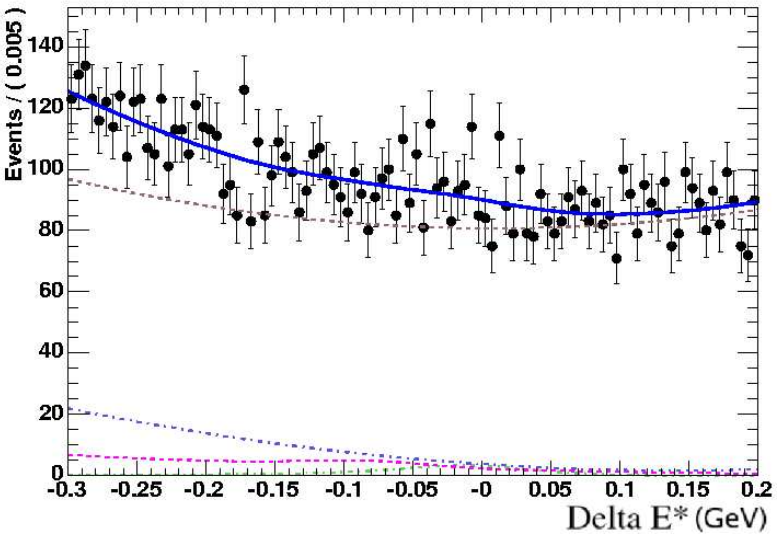

Figure A.39: ΔE^* distribution in data for $b \to d\gamma$ for the full *BABAR* dataset of 222x10^6 $B\bar{B}$ pairs. Signal is shown in green, $b \to s\gamma$ cross-feed in pink, generic B background in blue and continuum background in brown.

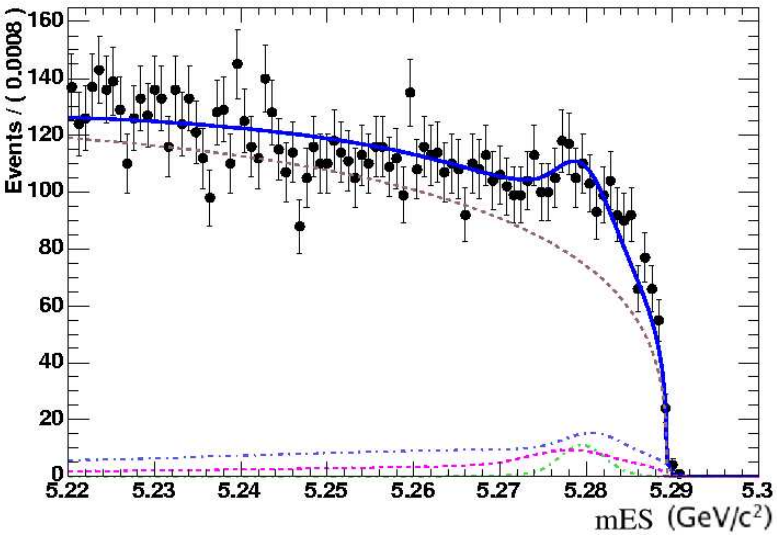

Figure A.40: $m_{\rm ES}$ distribution in data for $b \to d\gamma$ for the full *BABAR* dataset of 222x10^6 $B\bar{B}$ pairs. Signal is shown in green, $b \to s\gamma$ cross-feed in pink, generic B background in blue and continuum background in brown.

Bibliography

[1] Heavy Flavor Averaging Group (HFAG), *Averages of b-hadron Properties at the End of 2005*, hep-ex/0603003
(and http://www.slac.stanford.edu/xorg/hfag/rare/winter06/radll/index.html).

[2] P. Gambino and M. Misiak, Nucl. Phys. **B611** 338 (2001).

[3] B. Aubert *et al.*, the BaBar Collaboration, Phys. Rev. D **72** 052004 (2005).

[4] P.W. Higgs, Phys. Lett. **12** 132 (1964),
P.W. Higgs, Phys. Rev. Lett. **13** 508 (1964).

[5] P. Ramond, *Field Theory: A Modern Primer* (Addison-Wesley Publishing Company, 1990).

[6] N. Cabibbo, Phys. Rev. Lett. **10** 531 (1963).

[7] S.L. Glashow, J. Iliopoulos and L Maiani, Phys. Rev. D **2** 1285 (1970).

[8] M. Kobayashi and T. Maskawa, Prog. Th. Phys. **49** 652 (1973).

[9] J.J. Aubert *et al.*, Phys. Rev. Lett. **33** 1404 (1974).

[10] J.E. Augustin *et al.*, Phys. Rev. Lett. **33** 1406 (1974).

[11] S.W. Herb *et al.*, Phys. Rev. Lett. **39** 252 (1977).

[12] S. Abachi *et al.*, D0 Collaboration, Phys. Rev. Lett. **74** 2632 (1995).

[13] G.D. Rochester and C.C. Butler, Nature **160** 885 (1947).

[14] N.S. Lockyer *et al.*, Phys. Rev. Lett. **51** 1316 (1983).

[15] B. Aubert *et al.*, the BaBar Collaboration, Phys. Rev. Lett. **94** 161803 (2005).

[16] B. Aubert *et al.*, the BaBar Collaboration, Phys. Rev. Lett. **93** 131801 (2004).

[17] D.G. Hitlin (for the BABAR Collaboration), hep-ex/0011024.

[18] R. Ammar *et al.*, the CLEO Collaboration, Phys. Rev. Lett. **71** 674 (1993).

[19] A. Ali, E. Lunghi and A.Ya. Parkhomenko, Phys. Lett. B **595** 323 (2004).

[20] A. Bosch and G. Buchalla, Nucl. Phys. **B621** 459 (2002).

[21] D. Mohaptra *et al.*, the Belle Collaboration, hep-ex/0506079.

[22] B. Aubert *et al.*, the BaBar Collaboration, Phys. Rev. Lett. **94** 011801 (2005).

[23] B. Aubert *et al.*, the BaBar Collaboration, Phys. Rev. Lett. **93** 021804 (2004).

[24] K. Abe *et al.*, the Belle Collaboration, Phys. Rev. Lett. **93** 061803 (2004).

[25] John Walsh (for the BaBar Collaboration), hep-ex/0506043.

[26] A.L. Kagan and M. Neubert, Phys. Rev. D **58** 094012 (1998).

[27] G. Gomez-Ceballos (for the CDF collaboration), Flavor Physics and CP Violation Conference (2006).

[28] CKMfitter Group (J. Charles *et al.*), http://ckmfitter.in2p3.fr.

[29] S. Eidelman *et al.*, The Particle Data Group, Phys. Lett. B **592** 1 (2004) (and http://pdg.lbl.gov/).

[30] http://root.cern.ch/root/html//TMultiLayerPerceptron.html

[31] K. Hornik, M. Stinchcombe and H. White, *Multilayer feedforward networks are universal approximators.* Neural Networks, 2(**5**) 359 (1989).

[32] *BABAR* Analysis Document BAD-1137.

[33] *BABAR* Analysis Document BAD-134.

[34] B. Aubert *et al.*, the BaBar Collaboration, Phys. Rev. D **70** 112006 (2004).

[35] H. Albrecht *et al.* Phys. Lett. B **185** 218 (1987).

[36] W. Verkerke, D. Kirkby *et al.* RooFit toolkit for data modelling, http://roofit.sourceforge.net/.

[37] R. Brun *et al.* ROOT: An object-orientated data analysis framework, http://root.cern.ch.